Waves on Flexible Surfaces

Luisa Pruessner

A dissertation submitted in partial fulfillment

of the requirements for the degree of

Doctor of Philosophy

of

University College London

Department of Mathematics

University College London

September 2012

I, Luisa Pruessner confirm that the work presented in this thesis is my own. Where information has been derived from other sources, I confirm that this has been indicated in the thesis.

Abstract

The overall concern of the thesis is with fluid-body interaction in the sense of the fluid dynamics of external flow past a bluff body or other bounding surface whose shape responds to the flow properties. The work is motivated for the most part by industrial connections. Neither the flow nor the body shape is known at the outset. Indeed the major task described in the thesis is to predict the flow and the shape with a special emphasis being on the interactive behaviour inferred at relatively large flow rates. Allied with the above is the application of novel mathematical modelling, analysis and computation. The thesis addresses in turn some of the detail in the motivation for the work, the focus of the study, the most relevant background literature, the aim of the investigations and then the rest of the thesis. The latter part centres on triple-deck theory and related theory, linear and nonlinear phenomena, two-dimensional and three-dimensional responses, steady and unsteady interactions, and new kinds of resonances that are found, accompanied by typical real-world values of the parameters involved in the controlling systems.

Acknowledgement

I would like to thank my supervisor Frank Smith for his support and advice; Rob Lewis from TotalSim, Graham Johnson from BAE systems, Philip Bond and Dimitris Katsanis for their helpful input; and the EPSRC and UK Sport for their financial support.

Contents

List of Figures

List of Figures

Chapter 1

Intoduction

The concern of the thesis is with fluid-body interaction in the sense of the fluid dynamics of external flow past a bluff body or other bounding surface whose shape responds to the flow properties. Neither the flow nor the body shape are known in advance. Indeed the major task described in the thesis is to predict the flow and the shape. Allied with the above is the application of mathematical modelling, analysis and computation. This introduction addresses in turn the motivation for the work, the focus of the study, the most relevant background literature, the aim of the present investigations and then an outline of the rest of the thesis.

1.1 Motivation

The fluid flow past a bluff body represents a central and long-standing problem in fluid dynamics: see standard books such as [1,2]. Here a bluff body generally is of a non-streamlined shape, a body whose lateral dimension measured in the direction perpendicular to the oncoming fluid motion is of the same order as the streamwise dimension, or larger; that is in a two-dimensional configuration and a similar definition holds in three spatial dimensions. The presence of the bluff body leads to complicated flow phenomena especially at relatively high flow rates [3, 4] including most notably boundary layers, which in the regime of laminar flow are thin regions of fluid within which viscous

effects matter, adjacent to the body surface, whereas outside in the bulk of the motion viscous effects tend to be secondary except in thin shear layers. The laminar regime of well-ordered motion is not the most common one encountered however, or in a temporal sense it does not last long, as eruptions of the boundary layer occur together with transition from the laminar state and eventual turbulence, corresponding to a loss of well-ordered motion. The fluid flow over a portion of the body near the front face then tends to remain laminar whereas the majority of the rear face of the body is covered by turbulent flow. Somewhere between the front and the rear faces a transition from laminar to turbulent motion takes place.

Methods of flow control to delay or enhance transition to turbulence remain of significance and indeed have become increasingly important in many industrial applications, some of which are outlined in books such as [5] and many papers such as [6–12] . Most applications of real concern involve relatively rapid fluid flows, i.e. motions at high Reynolds numbers, and hence boundary layers where viscous influences combined with transition and separation can play key roles [13–17]. Precise definitions of the Reynolds number and of separation are given later but in broad terms the Reynolds number is a measure of the typical inviscid forces of inertia or momentum acting on the fluid relative to the typical viscous forces acting on the fluid.

There are many other motivations as well. In many racing sports, such as swimming, bob skeleton and Formula One car racing to name just a few, engineering methods to reduce drag on the athlete or vehicle and the equipment play an increasing part. In Formula One for example the Reynolds numbers involved are found to clearly lie in the turbulent regime and fairly competent computational models exist to deal with them. In other sports such as bob skeleton the Reynolds numbers are significantly lower and they can lie on the border between laminar and turbulent flow. This regime is much more difficult to deal with because of subtleties associated with instabilities, nonlinearities and transition; it is felt to need mathematical methods to make progress on small-disturbance stability or instability analysis together with non-small-disturbance transition and the resultant drag calculation for the whole body, or at least such methods may be of benefit to the total understanding.

Further on this theme, in aerodynamics in particular it is often desirable to reduce the overall drag on say a vehicle, an aim that has spawned many ingenious methods of experimentation, calculation or other types of research and prediction. These methods range from introducing trips and kicks on the solid surface or suction of boundary layer fluid through the wall of the body to special coatings that are intended to affect the boundary layer: see the above mentioned Gad-el-Hak [5] for example. There has also been considerable interest within such research in the effects of a flexible wall on the adjacent boundary layer flow, where one of the first questions to answer is whether there is substantial instability or delay of instability present in the flow. This question is one in which the current study is particularly interested. Early work on compliant surfaces and the flutter of flags include [18–26] and more recent work includes [27–30].

Trips can also be important devices [5,31] for flow control. Places of absolute instability for example as well as near-critical positions in a boundary layer say are most susceptible to outside influences. Studies of the corresponding receptivity issue abound [32–37]. It is for instance feasible in principle to place a trip in a region with an absolute instability to make the boundary layer pass through transition to turbulence. In such scenarios this would have the advantage that the boundary layer would stay attached for longer (turbulent boundary layers tend to do so (e.g. Neish and Smith [3], and also [37]) which could result in an overall drag reduction. In flow around a cylinder or bluff body a laminar boundary layer produces less skin-friction drag than a turbulent boundary layer but as it separates earlier the laminar case has a higher form drag. To produce the lowest value for the drag it is generally regarded as essential to place a trip in the right place. This may pose some quite substantial problems in practice if for example the Reynolds number is not constant, as the right place for the trip may change. It would be desirable to have a so-called tune-able trip which would only activate under the right conditions and remain neutral when the conditions are not met. Traditional trips are of fixed geometry of course and hence are always present; therefore if they are not placed appropriately they may well cause undesirable effects such as an overall increase in drag. In this thesis we are focusing, as stated below, on the effects produced by a flexible surface on the accompanying boundary layer. We are particularly interested in whether it is possible to achieve a

tune-able trip effect using such a flexible surface and whether there is here a viable option for total drag reduction.

1.2 The focus

The focus of the current study then is concerned with fluid dynamics at relatively high flow rates abetted by solid mechanics. The latter is treated in a basic simple fashion as a first step, rather than by the fuller more computational treatments that have been applied in biomedical studies especially (see Green et all [38] and other references above). The main elements of the study include bluff bodies, boundary layers, separation, instabilities, transition, turbulence, flexible walls and flow control. Here separation or breakaway separation [39, 40] refers to large-scale detachment of a boundary layer from a surface, leading on usually into a free shear layer as mentioned earlier, whereas small-scale separation tends to refer to a local eddy or reversed flow zone being created [41–44]. We should also define here the characteristic Reynolds number Re which is $\frac{U^*L^*}{\nu^*}$ where U* is a representative dimensional velocity of the oncoming fluid flow ahead of the body, L* is a typical body length scale in dimensional terms and ν^* is the kinematic viscosity of the fluid. The boundary layer therefore has characteristic thickness of order $Re^{(-1/2)}L^*$ from [31]. The solution methodology to aid the present focus consists in essence of modelling, scale reasoning, asymptotic theory, matched asymptotic expansions, reduced-system computation and attendant analysis.

Thus we will consider the fluid flow over a flat surface or bluff body which is covered by a flexible wall either in full or in part, with the consequent departure in shape from the original fixed form remaining small in a sense which will become clearer later. For the most part we will consider one or more blips of flexible materials separated by a solid non-flexible wall, the blips here being effectively humps or dents of unknown shape but of comparatively small size. However, we also consider the possibility of long or large blips where the flexible material spans the entire bluff body say.

To keep the basic scenarios simple and clear we will assume that the oncoming flow ahead of the

body is just a uniform stream. This is a reasonable approximation for the situation of a bluff body moving at relatively large speeds through a mostly stationary medium. For a runner racing in an indoor event for example this approximation is suitable, whereas for a runner racing in an outdoor event the approximation may break down if there are strong winds present, as the latter may alter significantly the form of the oncoming flow. Similar considerations apply to running, jumping, throwing, swimming and rowing sports subject to extra influences such as air-water interfacial effects. In any case the typical scenario leads to thin boundary layers being promoted along the body surface at least over a front portion of the body. Their expected thickness relative to an expected blip size is clearly a major parameter in terms of its order of magnitude, implying a need to investigate length and time scales in some depth.

We will indeed consider several different scales. We will first examine small blips that are in effect buried well within the boundary layer. The ones in mind are significant as they require a triple deck approach [45–48], giving us a dispersion relation which (to anticipate) relates the spatial growth rate of small linearised disturbances to the representative frequency of the disturbances in scaled form. Then, secondly, we will examine longer or larger blips which affect the whole boundary layer, for which we will need to consider the boundary layer equations. These larger blips span from the front stagnation point to the separation point on a bluff body. For this case we will find that it is justifiable to assume that the surface pressure is prescribed and we only need to solve for the shape of the blip. Finally, we will consider smaller blips and the effect that the variation of the flow strength to the flexibility strength has on the fluid flow and the wall shape. All of these investigations are to be done for a two-dimensional approximation mostly but as the final step these will have to be taken to three dimensions. These remarks and the following background material help set the scene for the thesis, it is felt.

1.3 Background

The broad background includes first the point that the present issues and their investigation arose from continued industrial interest and support. Second, the scientific and /or mathematical back-

ground to the current study is quite extensive as indicated previously in the introduction. Investigations of flexible wall effects have been performed since Kramer suggested in the 1950s that the compliant skin of the dolphin is responsible for its decreased drag, see [18]. An early theoretical treatment after Kramers discovery was done by Benjamin, see [19], while much of the fundamental work on this topic was carried out by Carpenter and Garrad, see [20,21], Davis and Carpenter [22]. Other works of significant interest include Gajjar and Sibanda [23], Fitt and Pope [27], Carpenter and Sen [24] and Jensen et al [28] on various different aspects of flexible surfaces and fluid-body interactions in internal or external flow configurations. Furthermore similar studies on the flutter of flags for example are by Theodorsen [25, 26], Argentina and Mahardevan [29] and Alben and Shelley [30].

Some more essential background we perhaps need is on the flow past a bluff body and triple-deck ideas. The work done on flow past bluff bodies is vast as hinted earlier and the basics are covered in many standard texts such as Schlichting [31], Paterson [1], Batchelor [2] and more recently Scheichl et al [39]. For the triple-deck structure and approaches concerning the effects of humps, corners, surface injections, separations, Tollmien-Schlichting instabilities, transition, spatial two-dimensionality and three-dimensionality we can turn to the contributions of Smith [13, 49], Rothmayer and Smith [50], Sychev et al [51] and Lagree [52, 53].

1.4 Aim

Overall, and to repeat to some extent, the aim of the thesis is to investigate and be able to predict the flow behavior due to a uniform stream encountering various shapes of bluff body with flexible surfaces. The intention is also to exploit this to find a method which utilizes flexible surfaces, in particular blips of flexible material, to create a tune-able trip in order to aid transition to turbulence and hence reduce the overall drag. Mathematical modeling, computations and analysis are anticipated to provide the means to fulfill this aim, founded especially on the use of asymptotics, scaling arguments and matching.

1.5 Outline of the thesis

In Chapter 2 below we describe the governing equations, non-dimensionalisation and scalings used throughout this thesis. These are based on the fluid and flow properties primarily, with the wall-flexibility properties being considered relative to the former properties and thus yielding several extra parameters of importance to the flow and shape solutions. The flexibility of the wall is represented by a direct relationship between the induced local pressure, the wall shape function and the wall curvature function along with the fourth derivative effect, all of which are unknowns. The relationship is taken to be a linear one involving coefficients whose appropriate scaled values can be estimated from real-world applications for example. The argument at this stage is under the assumption of two-dimensional unsteady motion for an incompressible fluid in general and with nonlinear responses being induced. We also present the derivation of the boundary-layer equations and the triple-deck interactions which are used in later chapters.

For small disturbances linearisation of the governing equations applies and enables more analytical progress to be made initially. A simple local instability analysis on piece-wise linear velocity profiles on a flexible wall and a comparison with the corresponding solid wall results are presented in Chapter 3. This is in order to generate an appreciation for the main mathematical methods that are required throughout the project in regard to small disturbances, and in fact larger disturbances are to be accommodated in a similar way. Ideas on important length and time scales also emerge here.

Chapter 4 is concerned with the situation where the scales are such that the flexible wall conditions are acting within a triple-deck structure, for which the unknown wall pressure, boundary-layer displacement and wall shape all interact together. The streamwise length scale here is slightly longer than the basic boundary-layer thickness but considerably less than the length scale of the boundary layer (which is typically the same as length scale of the bluff body). Small disturbances and linear effects are again the focus. We present a derivation of the full dispersion relation between disturbance frequency and wavelength as well as results for simplified time-dependent and time-independent cases. The latter cases form the basis for the remainder of the study.

In Chapter 5 nonlinear influences are admitted as we concentrate on blips of the boundary-layer length scale in the streamwise direction. Such larger blips, which span from the front stagnation point of the bluff body to the separation point, bring the classical Prandtl transposition into play and in effect the solution task becomes that of finding the wall shape for a given wall pressure distribution which is taken to be representative of the pressure on the front face of the body. A possible exception to this is near the breakaway separation point where a non-classical interaction is implied.

Nonlinearity is also a substantial factor in chapter 6 which presents the work on small-scale blips, whose length is much less than that of the triple deck above: a prime example is a blip whose length scale is comparable with the local boundary-layer thickness. Such small-scale blips produce negligible changes in the local boundary-layer displacement and hence give so-called condensed interactions. The effect of the variation of the ratio of the flow strength to the flexibility strength is explored, where the flow strength is proportional to the local wall-shear stress of the oncoming boundary layer while the flexibility strength is proportional to one of the coefficients mentioned earlier. This work leads to an investigation of resonance, generating a comparatively large response in the wall shape in particular.

Finally, in Chapter 7 we address a simplified model of the flexible wall relation in a linear regime again but in three spatial dimensions. Some interesting patterns of interference between arrayed blips are obtained.

Conclusions are presented in chapter 8. The main highlights and novel features in terms of the findings or predictions of the present investigation are believed to be the possible resonances where the blip size actually achieved far exceeds the expected size, the three-dimensional arrays including the ability to capture them according to the present approach, and the work on multiple blips with their accompanying advantages for flow control.

The research in the thesis has undoubtedly benefited from and been influenced by interactions

with an interdisciplinary group of researchers (see acknowledgements), meetings and support, for example concerning material properties of interest. The thesis necessarily must concentrate on detailed investigations of course, as well as considering breadth in terms of the subject area, but also a wider view is important because of the applications and corresponding motivation that underlie the work: to that end an attempt is made in chapter 8 to give a wider view together with responding to certain interesting points that arose during the interactions and meetings above.

Chapter 2

Governing equations, non-dimensionalisation and scalings

In this chapter we introduce the governing equations, which consist of the fluid flow equations as well as an equation describing the condition at the wall. These equations will be non-dimensionalised and then the various simplifications used in the following chapters will be presented. Since we are investigating flows over various flexible surfaces we clearly need to bring into play two such sets of equations in the formulation of our model. The first one is the set of equations describing the fluid flow, as mentioned above, and the second one is actually a pressure-shape equation describing the interaction of the flow model with the wall.

2.1 Governing equations and non-dimensionalisation

The fluid flow is governed by the Navier-Stokes equations: (2.1.1) below gives the momentum equation and (2.1.2) gives the continuity equation. We assume an incompressible Newtonian fluid

at this stage, see e.g. Batchelor [2]. Thus

$$\rho^*(\frac{\partial \underline{u}^*}{\partial t^*} + \underline{u}^*.(\underline{\nabla}.\underline{u}^*)) = -\underline{\nabla} p^* + \mu^* \nabla^2 \underline{u}^*, \tag{2.1.1}$$

$$\underline{\nabla}.\underline{u}^* = 0. \tag{2.1.2}$$

Here the superscript * where used indicates a dimensional quantity, $\underline{u}^*$ is the fluid velocity with components $\{u^*,v^*,w^*\}$ in three dimensions (x^*,y^*,z^*) or $\{u^*,v^*\}$ in two dimensions, p^* is the fluid pressure, ρ^* is the fluid density and μ^* is the fluid viscosity.

For the subsequent analysis it is most useful to non-dimensionalise these equations. We introduce the following scaling quantities: U as a scale for the speed of the fluid flow, L as a typical length scale of the object the flow is passing and T as a scale for the time such that $T = \frac{L}{U}$. We then apply the following transformations in the two-dimensional setting:

$$\{u^*, v^*, x^*, y^*, t^*, p^*\} = \{Uu, Uv, Lx, Ly, Tt, \rho^* U^2 p\}. \tag{2.1.3}$$

Hence in non-dimensional variables the fluid-flow equations (2.1.1 and 2.1.2) become:

$$\frac{\partial \underline{u}}{\partial t} + \underline{u}.(\underline{\nabla}.\underline{u}) = -\underline{\nabla} p + \frac{1}{R_e}\nabla^2 \underline{u}, \tag{2.1.4}$$

$$\underline{\nabla}.\underline{u} = 0. \tag{2.1.5}$$

Here $R_e = \frac{UL\rho^*}{\mu^*}$ is the Reynolds number. For chapters 3 - 6 we only consider two-dimensional flows, with streamwise coordinate x and corresponding velocity component u, and transverse coordinate y and corresponding velocity component v, i.e. $\underline{u} = (u, v)$. The two-dimensional Navier-Stokes equations for incompressible Newtonian fluids consist of:

$$u_t + uu_x + vu_y = -p_x + \frac{1}{R_e}(u_{xx} + u_{yy}) \qquad x\text{-momentum} \tag{2.1.6}$$

$$v_t + uv_x + vv_y = -p_y + \frac{1}{R_e}(v_{xx} + v_{yy}) \qquad y\text{-momentum} \tag{2.1.7}$$

$$u_x + v_y = 0 \qquad \text{continuity} \tag{2.1.8}$$

in component form.

2.2 Derivation of the two-dimensional boundary layer equations

We can simplify the above equations for R_e large since we assume for the most part that the flow disturbances occur inside the boundary layer, a thin viscous layer at the body surface. The rest of the flow can be considered as a non-viscous motion or even a uniform stream. This assumption leads to the boundary layer equations. We will present a brief derivation as details can be found in standard texts such as Schlichting [31]. The assumption is that the boundary layer is thin, which means that the streamwise coordinate x as well as the corresponding velocity component u remain of order one but the transverse coordinate y is of order δ, where δ is the characteristic boundary-layer thickness which is much less than unity. From the continuity equation it follows that the transverse velocity component v must also be of order δ. So we have the following scalings: $x \to x$, $u \to u$, $y \to \delta y$, $v \to \delta v$. The scaling for the Reynolds number comes from the relation between the boundary-layer thickness and the kinematic viscosity, namely the boundary-layer thickness is proportional to the square root of the kinematic viscosity and the kinematic viscosity is inversely proportional to the Reynolds number. We have $\delta \propto \sqrt{R_e^{-1}}$, and therefore $R_e^{-1} \to \delta^2$. Substituting the above into equations (2.1.6 and 2.1.7) gives:

$$u_t + uu_x + \delta v \delta^{-1} u_y = -p_x + \frac{1}{R_e}\delta^2(u_{xx} + \delta^{-2}u_{yy}), \tag{2.2.1}$$

$$\delta v_t + \delta u v_x + \delta^2 \delta^{-1} v v_y = -\delta^{-1} p_y + \frac{1}{R_e}\delta^2(\delta v_{xx} + \delta\delta^{-2} v_{yy}). \tag{2.2.2}$$

Terms containing factors of δ are small compared to terms without and terms containing δ^{-1} are larger. Therefore the leading order of (2.2.1 and 2.2.2) together with the continuity equation give the boundary layer equations as:

$$u_t + uu_x + vu_y = -p_x + \frac{1}{R_e}u_{yy}, \tag{2.2.3}$$

$$p_y = 0, \tag{2.2.4}$$

$$u_x + v_y = 0. \tag{2.2.5}$$

We retain the factor R_e^{-1} in (2.2.3) here for convenience. Also here (2.2.4) implies that $p = p(x,t)$, the pressure inside the boundary layer, depends only on x and t and hence equates to the pressure just outside. For a uniform stream of speed U over a flat plate the boundary conditions are $u \to 1$ as $y \to \infty$ and $u = v = 0$ at $y = 0$. Solving for this set-up with $u_t \equiv 0$ will give the classical steady-flow results of the Blasius boundary layer, which we will make use of in the triple-deck analysis below. Precise boundary conditions are discussed later.

2.3 Derivation of the triple-deck equations

Next we will present a brief derivation of the triple-deck equations since the triple-deck structure provides a very useful tool for analysing flow over surface-mounted humps, corners, wall injections, trailing edges and so on: see reviews by Smith [13], Sychev et al [51], Rothmayer and Smith [50]. In contrast with the classical case of the boundary layer described in the previous section the pressure in the triple-deck case is unknown in advance as it interacts with the local displacement of the motion which is also unknown. As suggested in the name there are three decks, the lower deck, right at the wall, the middle deck or main deck, which is the main part of the boundary layer, and the upper deck lying just outside the boundary layer. We introduce a small parameter $\epsilon = R_e^{-\frac{1}{8}}$, which is used to scale the equations. Throughout the decks the streamwise coordinate x is scaled as $x = \epsilon^3 X$, implying a length scale which is short but still longer than the boundary-layer thickness,

and time is scaled as $t = \epsilon^2\tau$, corresponding to a relatively short time scale. The scaling of the transverse coordinate y depends on which deck we are considering. For the lower deck we have scaled transverse variable $y = \epsilon^5 Z$ and the basic flow is the Blasius flow $U_0 = \epsilon\lambda Z + \epsilon^4\lambda_4 Z^4$, following the example in Smith [], which results to leading order in the following linearized equations:

$$U_{1X} + V_{1Z} = 0 \quad \text{continuity} \tag{2.3.1}$$

$$U_{1\tau} + \lambda Z U_{1X} + \lambda V_1 = -P_{1X} + U_{1ZZ} \tag{2.3.2}$$

Here, we have used the linearized form for simplicity. The boundary conditions are the wall equation, usually the no-slip condition $U = V = 0$ at $Z = 0$, and matching with the middle deck $U \sim \lambda(Z + A(X,\tau))$ as $Z \to \infty$, where the function $A(X,\tau)$ is to be determined.

In the main deck we have the scaled transverse variable $y = \epsilon^4 Y$, and the basic flow here is the Blasius flow which has the properties $U_B = f_B'(q)$, $f_B''' + \frac{1}{2} f_b f_b'' = 0$, $f_B(0) = f_B'(0)$ and $f_B'(q) \to 1$ as $q \to \infty$ where $q = Y x^{'\frac{1}{2}}$. This leads to the following equations for the main deck:

$$u_{1X} + v_{1Y} = 0 \quad \text{continuity} \tag{2.3.3}$$

$$U_B u_{1x} + v_1 U_{BY} = 0 \quad \text{x-momentum} \tag{2.3.4}$$

The y-momentum equation simply tells us that the pressure is independent of the transverse coordinate Y. Here the boundary conditions are matching with the lower deck $U \sim \lambda(Z + A(X,\tau))$ as $Y \to 0$ and matching with the upper deck as $Y \to \infty$.

Finally, the upper deck has the vertical coordinate $y = \epsilon^3\bar{y}$, the basic flow here is $U_0 = 1$ and so we need to solve Laplace's equation for the pressure:

$$\nabla^2 P = 0. \tag{2.3.5}$$

Here we have the boundary conditions of matching with the middle deck as $\bar{y} \to 0$ and boundedness

as $\bar{y} \to \infty$. Again, precise boundary conditions are discussed later on.

2.4 The flexible-wall equation

We next seek an equation describing the interaction between the flexible wall and the fluid flow, again in two dimensions for now. The fluid flow and the flexible wall interact via the pressure, in the current model. The equation we examine has been described by Carpenter et al [20–22] and subsequently by Gajjar et al [23] and it has the form

$$M^*\frac{\partial^2 \eta^*}{\partial t^{*2}} + C^*\frac{\partial \eta^*}{\partial t^*} + B^*\frac{\partial^4 \eta^*}{\partial x^{*4}} - {T_t}^*\frac{\partial^2 \eta^*}{\partial x^{*2}} + \kappa^*\eta^* = -p^* + {p_0}^*. \tag{2.4.1}$$

In the above equation M* is a mass density (i.e. mass per unit length in one dimension), C* is the damping constant, B* is the flexural rigidity, κ^* is the spring stiffness, ${T_t}^*$ is the tension, p^* is the unknown pressure and η^* is the unknown surface shape, in the sense that the surface lies at $y^* = \eta^*(x^*, t^*)$ in the two-dimensional case.

The non-dimensionalisation of the pressure and the streamwise-coordinate in (2.4.1) are the same as described above. We also introduce a scale for η^*, namely a distance scale H, and a time scale T for t^*. This time scale might in principle be not the same as above but in fact it is probably best defined through normalization of the Strouhal number ($S = \frac{L}{UT}$) to unity and so T is again $\frac{L}{U}$. We apply the following transformations:

$$\{\eta^*, x^*, t^*, p^*\} = \{L\eta, Lx, Tt, \rho^* U^2 p\}. \tag{2.4.2}$$

in keeping with (2.1.3). Hence in non-dimensional variables the wall equation becomes:

$$e_1\frac{\partial^4 \eta}{\partial x^4} + e_2\frac{\partial^2 \eta}{\partial x^2} + e_3\eta + e_4\frac{\partial^2 \eta}{\partial t^2} + e_5\frac{\partial \eta}{\partial t} = p - p_0. \tag{2.4.3}$$

Here the non-dimensional constants e_i as obtained from the dimensional quantities of equation

(2.4.1) are

$$e_1 = -\frac{B^*}{\rho^* U^2 L^3}, \tag{2.4.4}$$

$$e_2 = \frac{T_t^*}{\rho^* U^2 L}, \tag{2.4.5}$$

$$e_3 = -\frac{\kappa^* L}{\rho^* U^2}, \tag{2.4.6}$$

$$e_4 = -\frac{M^*}{\rho^* L}, \tag{2.4.7}$$

$$e_5 = -\frac{C^*}{\rho^* U}. \tag{2.4.8}$$

The scalings are as follows (to repeat for convenience what is in section 2.1): U is the typical fluid's speed or the object's speed if the fluid is stationary, L is the typical length scale of the object. To give estimates of the parameters e_i we need to know the fluid and object properties ρ^*, L, U and also the material properties B*, T_t^*, κ^*, M* and C*.

In the real-world applications the material properties B* (flexural rigidity), T_t^* (tension), κ^* (spring stiffness), M* (mass density) and C* (damping factor) are not independent. They are related through equations containing the Young's modulus (E) and the Poisson ratio (ν) as well as certain other quantities, as follows.

The flexural rigidity can be expressed as:

$$B^* = \frac{Et^3 b}{12(1-\nu^2)} \tag{2.4.9}$$

where E is the Young's modulus, t is the material thickness, b is the material width and ν is the Poisson ratio. The tensile modulus can be calculated as:

$$E = \frac{F}{A\epsilon} \tag{2.4.10}$$

where E is the tensile (Youngs) modulus, F is the applied load, A is the cross-sectional area and ϵ is the material strain. This tensile or Young's modulus must correspond to the one used in the equation (2.4.9) for the flexural rigidity. One traditional formulation for the spring stiffness κ^* is :

$$\kappa^* = \frac{AE}{L} \tag{2.4.11}$$

where L is the length of the material beam and A is the cross-section. The damping constant C* is determined via the damping ratio as follows:

$$\zeta = \frac{C^*}{2\sqrt{\kappa M}}. \tag{2.4.12}$$

Here ζ is the damping ratio.

The values of the above quantities if required need to be determined experimentally or are tabulated for certain materials. The experimental methods used are outside the scope of this report.
In later chapters we will make use of different scalings, namely a boundary-layer length scale and a triple-deck length scale. In the case of the boundary-layer length scale we will introduce a scaling quantity H, which is the boundary-layer thickness. In the case of the triple deck we will make use of the typical triple-deck scaling involving different powers of the Reynolds number. These further scalings, as derived below, will introduce additional scaling factors effectively in the expression for the parameters e_i and hence their values as used in the working will then be modified.

Throughout most of the theory presented in this study we do not work with the full $p - \eta$ equation (2.4.3) but instead make the assumption that we can neglect some of the terms in the equation. In later chapters we use time-dependent and time-independent approaches. For the time-dependent approach we also use the following simplification of the $p - \eta$ relation:

$$e_3\eta + e_4\frac{\partial^2\eta}{\partial t^2} + e_5\frac{\partial\eta}{\partial t} = p - p_0. \tag{2.4.13}$$

For the time-independent approach the following simplification of the $p - \eta$ relation is employed:

$$e_1 \frac{\partial^4 \eta}{\partial x^4} + e_2 \frac{\partial^2 \eta}{\partial x^2} + e_3 \eta = p - p_0, \tag{2.4.14}$$

again from (2.4.3). The above simplifications apply to two-dimensional calculations. For three dimensions we simplify further and assume that e_1 is negligible compared with e_2. Considering the relative magnitude of the real-world parameters described earlier in the present chapter this is indeed a valid approximation. In such cases we have:

$$e_2 \frac{\partial^2 \eta}{\partial x^2} = p - p_0. \tag{2.4.15}$$

This is not only sensible in physical terms but also allows us to solve more readily for η using analytical methods, as we shall see in some of our subsequent working.

We are now going to consider the two different length scales in the streamwise direction mentioned above. The first one is the boundary-layer development scale; at this scale it is assumed that the non-dimensional variable x remains of order one [46]. The second one is the triple deck scale; in this scale we assume that the non-dimensional variable x scales with the Reynolds number as $R_e^{-\frac{3}{8}}$ [46] as in section 2.3. Clearly the boundary-layer scale has a larger x scale and we expect to pick up different effects from those of a shorter length scale.

2.5 The boundary-layer development scale

In case of the boundary layer we scale the y-direction or η of the flexible-wall equations by a factor h (to be specified below) while the x-direction stays of order one, i.e. we scale the parameters as $\bar{e_i} = he_i$. Therefore we have the following expressions for the new parameters $\bar{e_i}$,

$$\bar{e}_1 = -\frac{hB^*}{\rho^* U^2 L^3}, \tag{2.5.1}$$

$$\bar{e}_2 = \frac{hT_t^*}{\rho^* U^2 L}, \tag{2.5.2}$$

$$\bar{e}_3 = -\frac{h\kappa^* L}{\rho^* U^2}, \tag{2.5.3}$$

$$\bar{e}_4 = -\frac{hM^*}{\rho^* L}, \tag{2.5.4}$$

$$\bar{e}_5 = -\frac{hC^*}{\rho^* U}. \tag{2.5.5}$$

Here h is a non-dimensional scale parameter and is related to the boundary-layer thickness H by $h = \frac{H}{L}$, where L is the typical length scale as described in section 2.1. We will make use of this scale for the large blips discussed in chapter 5.

2.6 The triple-deck scale

In the case of the triple deck we introduce the following scalings, using $\epsilon = R_e^{-\frac{1}{8}}$ and bearing section 2.3 in mind,

$$\{x, y, \eta, t, p\} = \{\epsilon^3\tilde{x}, \epsilon^5\tilde{y}, \epsilon^5\tilde{\eta}, \epsilon^2\tilde{t}, \epsilon^2\tilde{p}\}. \tag{2.6.1}$$

This is specifically for the lower deck of the structure since that deck is closest to the flexible wall and hence relevant to flexing responses there. Therefore the following scaled expressions, $\tilde{e_i}$, for the

parameters e_i apply:

$$\tilde{e}_1 = -R_e^{\frac{9}{8}} \frac{B^*}{\rho^* U^2 L^3}, \tag{2.6.2}$$

$$\tilde{e}_2 = R_e^{\frac{3}{8}} \frac{T_t^*}{\rho^* U^2 L}, \tag{2.6.3}$$

$$\tilde{e}_3 = -R_e^{-\frac{3}{8}} \frac{\kappa^* L}{\rho^* U^2}, \tag{2.6.4}$$

$$\tilde{e}_4 = -R_e^{\frac{1}{8}} \frac{M^*}{\rho^* L}, \tag{2.6.5}$$

$$\tilde{e}_5 = -R_e^{-\frac{1}{8}} \frac{C^*}{\rho^* U}. \tag{2.6.6}$$

This scaling applies in the lower deck of the triple-deck structure and the other decks remain as usual. Further, we introduce a quantity a, which measures essentially the ratio of flow strength to flexibility strength. This quantity enters into the calculations as another scaling factor for the parameters $\tilde{e}_i$. We will make use of this scaling for the small blips discussed in chapter 4.

Chapter 3

Models with Simple Velocity Profiles

The focus in the majority of the thesis is on fluid motion past a bluff body, at relatively high values of the Reynolds number R_e, with the body in effect having comparatively small fluctuations of its surface shape. These fluctuations occur through interactions with the fluid flow properties including especially the induced fluid flow pressure. There is thus flow-structure interaction; see [38, 54]. The fluctuations can be small 'vertically' in the sense of the small spatial deviations they produce in the direction normal to the undisturbed surface of the body compared with the streamwise deviations, i.e. their slopes may be small. The fluctuations can also be small or large in the streamwise direction, 'horizontally', depending on the ratio of length scales of the fluctuation and the underlying body shape. In either case the two main contenders for providing a plausible theoretical mechanism responsible for significant fluctuations are fluid-dynamic instability [55] and thin-layer interaction [50].

These contenders and possible combinations of them need to be considered for various distinct scenarios.

Our initial concern here is with the local stability of a basic flow (with local streamwise velocity

profile $u = U(y)$ in effect) when small disturbances are present. The parallel-flow approximation is adopted, namely that the velocity components of the basic flow apart from u can be neglected and any x, z, t dependence in u can also be neglected. The method that is used in this stability analysis is to solve the well-known Rayleigh equation for small inviscid disturbances [55]. The next three sections present a short overview of the equations and boundary conditions that need to be solved. The two subsections then each present the stability analysis of a simple velocity profile, namely the simple shear flow and the uniform stream. These will then be compared to the equivalent solid wall solution in the final section.

3.1 Derivation of the linearized Navier-Stokes equations for parallel basic flow

As mentioned above we will utilize the Rayleigh equation to perform a stability analysis for simple piecewise velocity profiles. In this section we are presenting a derivation of the linearized Navier-Stokes equations, followed by the derivation of the Rayleigh equation and Orr-Sommerfeld equation from Navier-Stokes equations in the subsequent sections. Treatments of these derivations can be found in many standard texts, for example Drazin and Reid [55] or more recently Schmid and Hennigson [56].

The Navier-Stokes equations for incompressible Newtonian fluids are given by:

$$\frac{\partial \underline{v}}{\partial t} + (\underline{v}.\underline{\nabla})\underline{v} = -\underline{\nabla} p + R^{-1}\nabla^2 \underline{v} \qquad \text{momentum,} \tag{3.1.1}$$

$$\underline{\nabla}.\underline{v} = 0 \qquad \text{continuity,} \tag{3.1.2}$$

in terms of the velocity vector written as $\underline{v}$ for convenience and the pressure p. We assume a basic flow $\underline{U}$, which is known and satisfies the Navier-Stokes equations, and now introduce a disturbance $\underline{u}$, which is assumed to be small to allow us to linearize the equations. The new flow is $\underline{v} = \underline{U} + \underline{u}$

with pressure $P + p$ which must also satisfy the Navier-Stokes equations. Hence

$$\frac{\partial(\underline{U} + \underline{u})}{\partial t} + [(\underline{U} + \underline{u}).\underline{\nabla}]\,(\underline{U} + \underline{u}) = -\underline{\nabla}(P + p) + R_e^{-1}\nabla^2(\underline{U} + \underline{u}). \tag{3.1.3}$$

Since the basic flow $\underline{U}$ satisfies the Navier-Stokes equation we can use (3.1.1) to obtain

$$\frac{\partial \underline{u}}{\partial t} + (\underline{u}.\underline{\nabla})\underline{U} + (\underline{U}.\underline{\nabla})\underline{u} + (\underline{u}.\underline{\nabla})\underline{u} = -\underline{\nabla}p + R_e^{-1}\nabla^2\underline{u}, \tag{3.1.4}$$

which acts as an equation controlling the disturbance $\underline{u}$ and the corresponding pressure p. The next step is to linearise equation(3.1.4), which suppresses the nonlinear term $(\underline{u}.\underline{\nabla})\underline{u}$, since this is quadratic in $\underline{u}$ and we assume that the disturbances are small. We therefore obtain:

$$\frac{\partial \underline{u}}{\partial t} + (\underline{U}.\underline{\nabla})\underline{u} + (\underline{u}.\underline{\nabla})\underline{U} = -\underline{\nabla}p + R_e^{-1}\nabla^2\underline{u}. \tag{3.1.5}$$

The next assumption is that the basic flow is parallel and only depends on the vertical coordinate (i.e. y), which means $\underline{U} = U(y)\hat{\underline{i}}$ where $\hat{\underline{i}}$ is the unit vector in the x-direction. Applying this, equation (3.1.5) simplifies to

$$\frac{\partial u}{\partial t} + U\frac{\partial u}{\partial x} + v\frac{dU}{dy} = -\frac{\partial p}{\partial x} + R_e^{-1}\nabla^2 u, \tag{3.1.6}$$

$$\frac{\partial v}{\partial t} + U\frac{\partial v}{\partial x} = -\frac{\partial p}{\partial y} + R_e^{-1}\nabla^2 v, \tag{3.1.7}$$

$$\frac{\partial w}{\partial t} + U\frac{\partial w}{\partial x} = -\frac{\partial p}{\partial z} + R_e^{-1}\nabla^2 w, \tag{3.1.8}$$

$$\frac{\partial u}{\partial x} + \frac{\partial v}{\partial y} + \frac{\partial w}{\partial z} = 0. \tag{3.1.9}$$

These are the linearized Navier-Stokes equations for parallel basic flow.

3.2 Derivation of the Rayleigh equation

In order to derive the Rayleigh equation for two-dimensional inviscid flow we assume wavelike disturbances for the flow $\underline{u}$ and the pressure p, i.e.

$$\underline{u} = \underline{\tilde{u}}(y)e^{i\alpha(x-ct)}, \tag{3.2.1}$$

$$p = \tilde{p}(y)e^{i\alpha(x-ct)}. \tag{3.2.2}$$

Here α and c are constants. Substituting (3.2.1 and 3.2.2) in the above equations (3.1.6-3.1.9) and neglecting z-dependence as well as viscous forces gives

$$-i\alpha c\tilde{u} + i\alpha U\tilde{u} + \tilde{v}\frac{dU}{dy} = -i\alpha\tilde{p}, \tag{3.2.3}$$

$$-i\alpha c\tilde{v} + i\alpha U\tilde{v} \qquad\qquad = -\frac{d\tilde{p}}{dy}, \tag{3.2.4}$$

$$i\alpha\tilde{u} + \frac{d\tilde{v}}{dy} = 0. \tag{3.2.5}$$

Now we introduce a stream function for the disturbances such that

$$u = \frac{\partial\psi}{\partial y} \text{ and} \tag{3.2.6}$$

$$v = -\frac{\partial\psi}{\partial x} \text{ with} \tag{3.2.7}$$

$$\psi = \tilde{\psi}(y)e^{i\alpha(x-ct)}. \tag{3.2.8}$$

Then we have $\tilde{u} = \frac{\partial\tilde{\psi}}{\partial y}$ and $\tilde{v} = -i\alpha\tilde{\psi}$, and so substituting these into the x- momentum equation gives us the following expression for the pressure

$$\tilde{p} = \frac{dU}{dy}\tilde{\psi} - (U-c)\tilde{\psi}'. \tag{3.2.9}$$

The last step is to substitute this expression for $\tilde{p}$ into the y-momentum equation. This results in the Rayleigh equation:

$$(U-c)(\frac{d^2\tilde{\psi}}{dy^2}-\alpha^2\tilde{\psi})-\frac{d^2U}{dy^2}\tilde{\psi}=0, \tag{3.2.10}$$

for the perturbation stream function.

3.3 Derivation of the Orr-Sommerfeld equation

To derive the Orr-Sommerfeld equation we keep the viscous term; the derivation is very similar to that of the Rayleigh equation. Again, we assume parallel basic flow $\underline{U}=U(y)\hat{\underline{i}}$ with $\nu\frac{d^2U}{dy^2}=\frac{1}{\rho}\frac{dP}{dx}$ if $\frac{dP}{dx}$ is constant. This can also work for nearly parallel flows $\underline{U}=\{U(x,y),V(x,y),0\}$ with $V<<U$ and $\frac{\partial U}{\partial x}<<1$ in effect.

Starting from the linearized Navier-Stokes equations (3.1.6-3.1.9), we assume the same two-dimensional wave-like forms for the disturbances as for the Rayleigh equation and substitute into the Navier-Stokes equations to obtain:

$$-i\alpha c\tilde{u}+i\alpha U\tilde{u}+v\frac{dU}{dy}=-i\alpha\tilde{p}-R^{-1}\alpha^2\tilde{u}+R^{-1}\frac{d^2\tilde{u}}{dy^2}, \tag{3.3.1}$$

$$-i\alpha c\tilde{v}+i\alpha U\tilde{u}\qquad\qquad=-\frac{d\tilde{p}}{dy}-R^{-1}\alpha^2\tilde{v}+R^{-1}\frac{d^2\tilde{v}}{dy^2}, \tag{3.3.2}$$

$$i\alpha\tilde{u}+\frac{d\tilde{v}}{dy}=0. \tag{3.3.3}$$

Rearranging the above to have terms involving $\tilde{u}$ and $\tilde{v}$, respectively, on the left hand side and other terms on the right hand side gives:

$$\{-i\alpha c+i\alpha U+R^{-1}\alpha^2-R^{-1}\frac{d^2}{dy^2}\}\tilde{u}=-i\alpha\tilde{p}-\tilde{v}\frac{dU}{dy}, \tag{3.3.4}$$

$$\{-i\alpha c+i\alpha U+R^{-1}\alpha^2-R^{-1}\frac{d^2}{dy^2}\}\tilde{v}=-\frac{d\tilde{p}}{dy}, \tag{3.3.5}$$

$$i\alpha\tilde{u} + \frac{d\tilde{v}}{dy} = 0. \tag{3.3.6}$$

The next step is to express $\tilde{u}$ and $\tilde{v}$ in terms of the perturbation stream-function (3.2.6-3.2.8), which takes the same form as given above for the derivation of the Rayleigh equation, and to use the x-momentum equation to eliminate $\tilde{p}$. Thus we obtain the following expression for the pressure:

$$\tilde{p} = \tilde{\psi}\frac{dU}{dy} + \{c - U - (i\alpha R)^{-1}\alpha^2 + (i\alpha R)^{-1}\frac{d^2}{dy^2}\frac{d\tilde{\psi}}{dy}. \tag{3.3.7}$$

Substituting the above into the y-momentum equation (3.12b) results in the Orr-Sommerfeld equation for $\tilde{\psi}$,

$$(i\alpha R)^{-1}(\frac{d^2}{dy^2} - \alpha^2)^2\tilde{\psi} = (U - c)(\frac{d^2}{dy^2} - \alpha^2)\tilde{\psi} - \frac{d^2U}{dy^2}\tilde{\psi} \tag{3.3.8}$$

The Orr-Sommerfeld equation presents an alternative way to derive the linearized triple-deck equations to the one we have shown in Chapter 2, where we derived the triple-deck equations directly from the Navier-Stokes equations and then linearized the system.

3.4 The Rayleigh equation for piecewise linear velocity profiles

The Rayleigh equation for small inviscid disturbances is given by equation (3.2.10) above. A detailed treatment of the following problems can be found in Drazin and Reid [55] for example but it is felt important to include a derivation here. In the case of piecewise linear velocity profiles the second derivative of the basic-flow velocity U vanishes. The Rayleigh equation (3.2.10) therefore simplifies to

$$(U - c)(\frac{d^2\tilde{\psi}}{dy^2} - \alpha^2\tilde{\psi}) = 0 \tag{3.4.1}$$

and from (3.4.1) we require in general

$$\frac{d^2\tilde{\psi}}{dy^2} - \alpha^2\tilde{\psi} = 0 \tag{3.4.2}$$

subject to two jump conditions at each discontinuity in the basic velocity profile or its slope, located at $y = y_0$ say. These two conditions stem from the requirements that the pressure as well as the normal velocity have to be continuous across the implied material interface. Positions where $U = c$ holds instead of (3.4.2) define critical layers if c is real but these are not usually of direct relevance in this chapter.

The pressure condition is:

$$[(U-c)\tilde{\psi}' - U'\tilde{\psi}] = \textit{continuous} \text{ at } y = y_0. \tag{3.4.3}$$

The condition on the normal velocity is:

$$\left[\frac{\tilde{\psi}}{U-c}\right] = \textit{continuous} \text{ at } y = y_0. \tag{3.4.4}$$

The above pressure condition and the condition on the normal velocity hold at each profile discontinuity in the fluid. Also, at a fixed solid wall, say at $y = 0$, we require

$$\tilde{\psi} = 0 \tag{3.4.5}$$

for the sake of the condition of tangential flow or zero penetration at such a wall.

In the case of a flexible wall we need to derive a different condition at the wall, involving the pressure. Now, we have two conditions at $y = 0$, the pressure-shape relation and the kinematic condition. These are given below:

$$p = e_1\eta_{xxxx} + e_2\eta_{xx} + e_3\eta + e_4\eta_{tt} + e_5\eta_t, \tag{3.4.6}$$

$$v = S\eta_t + u\eta_x. \tag{3.4.7}$$

Here the constant coefficients e_i are the same as defined in Chapter 2, $S = \frac{h}{UT}$ is the Strouhal number and $p_0 = 0$. For our purposes we recall we have normalized the Strouhal number to unity; this sets the time scale. The above equations (3.4.6 and 3.4.7) can be significantly simplified if we assume as in (3.2.1 and 3.2.2) small disturbances of the form:

$$p = \tilde{p}(y)e^{i\alpha(x-ct)} \text{ pressure}, \tag{3.4.8}$$

$$v = \tilde{v}(y)e^{i\alpha(x-ct)} \text{ velocity}, \tag{3.4.9}$$

$$\eta = \tilde{\eta}qe^{i\alpha(x-ct)} \text{ surface elevation}, \tag{3.4.10}$$

$$\psi = \tilde{\psi}(y)e^{i\alpha(x-ct)} \text{ stream function}, \tag{3.4.11}$$

where again the constants α and c are the wave number and the wave speed, respectively. The above assumptions in equations (3.4.8-3.4.11) allow us to eliminate η and express the pressure in terms of the streamfunction, i.e.

$$\tilde{p} = \frac{\alpha^4 e_1 - \alpha^2 e_2 + e_3 - \alpha^2 c^2 e_4 - i\alpha c e_5}{c - U}\tilde{\psi}. \tag{3.4.12}$$

Substituting this into the pressure equation, which is obtained when deriving the Rayleigh equation as above, i.e.

$$\tilde{p} = u'\tilde{\psi} - (U - c)\tilde{\psi}', \tag{3.4.13}$$

we obtain the following boundary condition on $\tilde{\psi}$ at the flexible wall:

$$\frac{\alpha^4 e_1 - \alpha^2 e_2 + e_3 - \alpha^2 c^2 e_4 - i\alpha c e_5}{c - U}\tilde{\psi} = U'\tilde{\psi} - (U - c)\tilde{\psi}' \qquad \text{at } y = 0. \tag{3.4.14}$$

For a given velocity profile $U(y)$ the aim then is to solve for the streamfunction $\tilde{\psi}$ and find the wave speed c (possibly complex) for prescribed real values of the wavenumber α or find the values for the wave number α (possibly complex) for prescribed real values of the wave speed c. In the following section the first approach is followed, with α real.

For instability to be present the wave speed c is required or allowed to be complex, i.e. $c = c_r + ic_i$, with the imaginary part c_i positive. The disturbances considered have complex exponential form, i.e. $\propto e^{i\alpha(x-ct)}$. Therefore a positive imaginary part of the wave speed c_i would give exponential growth, i.e. a factor $e^{\alpha c_i t}$ would appear. Prime examples of interest are studied in the subsequent subsections where we use the condition (3.4.14) to examine two simple flows, namely uniform shear flow and a uniform stream. Again the question we are interested in answering is whether instability is present in the flow and under what conditions it occurs. We will also compare the solid wall solutions with the flexible wall solutions to investigate how the presence of the flexible wall affects the flow.

3.4.1 Simple shear flow

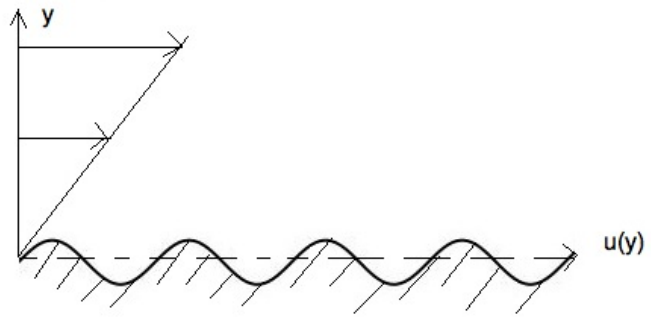

Figure 3.1: Schematic of simple basic shear flow over a flexible surface

The first step is to solve the Rayleigh equation (3.2.10) for the given basic velocity profile. The simple shear velocity profile $U = \lambda y$ for all positive y and for constant shear rate λ is a linear profile, which makes the Rayleigh equation particularly easy to solve. Taking into account that the

streamfunction has to be bounded at infinity we have from (3.2.10)

$$\tilde{\psi} = Ae^{-\alpha y}, \tag{3.4.15}$$

where A is constant. To determine the wavespeed in terms of the wavenumber and the flexibility parameters we have to use the wall condition derived in (3.4.14). Substituting the streamfunction into the wall condition (3.4.14) at $y = 0$ gives a quadratic equation for the wavespeed c:

$$(-\alpha^4 e_4 + \alpha)c^2 - (i\alpha e_5 + \lambda)c + (\alpha^4 e_1 - \alpha^2 e_2 + e_3) = 0, \tag{3.4.16}$$

and solving for the wavespeed gives:

$$c = \frac{1}{2(\alpha - \alpha^2 e_4)} \left[\lambda + i\alpha e_5 \pm \sqrt{(\lambda + i\alpha e_5)^2 - 4(\alpha - \alpha^2 e_4)(\alpha^4 e_1 - \alpha^2 e_2 + e_3)}\right]. \tag{3.4.17}$$

In general the implied wavespeed might be expected to be complex. For instabilities to be present we require c_i to be positive. We can plot the growth rate c_i as a function of frequency α. We have done this for an example of parameters $\lambda = 1$, $e_1 = -1$, $e_2 = 1$, $e_3 = -1$, $e_4 = -1$ and $e_5 = -1$ below. Taking the positive root, see figure 3.2 and taking the negative root, see figure 3.3. These results clearly show that there is instability present, in particular at small wavenumbers. It should be mentioned in addition that the square root in (3.4.17) indicates a delicate interplay between flow strength represented by λ and flexibility strength represented by $e_1 - e_5$, as far as instability is concerned.

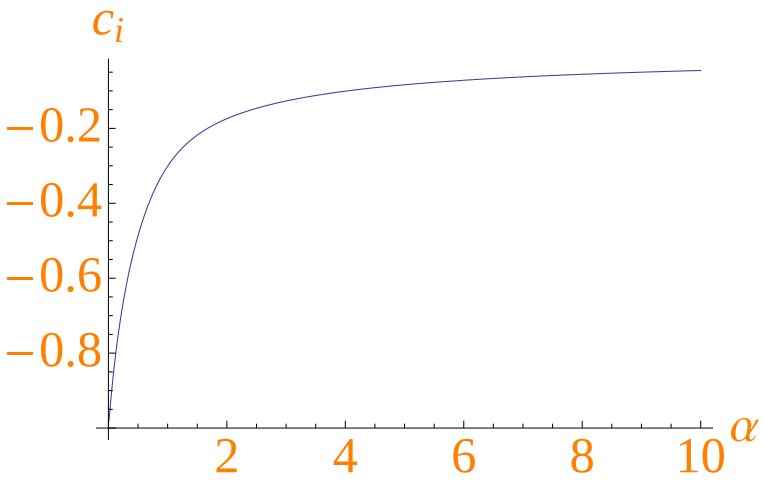

Figure 3.2: dispersion relation for $c = \frac{1}{2(\alpha-\alpha^2 e_4)}\left[\lambda + i\alpha e_5 + \sqrt{(\lambda+i\alpha e_5)^2 - 4(\alpha-\alpha^2 e_4)(\alpha^4 e_1 - \alpha^2 e_2 + e_3)}\right]$.

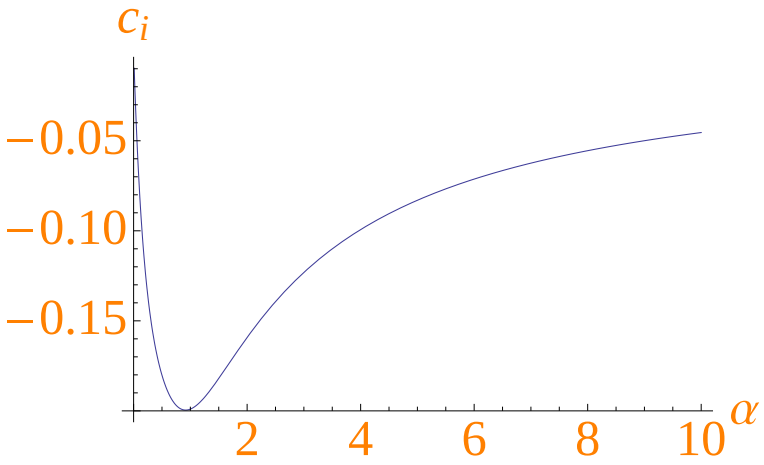

Figure 3.3: dispersion relation for $c = \frac{1}{2(\alpha-\alpha^2 e_4)}\left[\lambda + i\alpha e_5 - \sqrt{(\lambda+i\alpha e_5)^2 - 4(\alpha-\alpha^2 e_4)(\alpha^4 e_1 - \alpha^2 e_2 + e_3)}\right]$.

3.4.2 Uniform stream

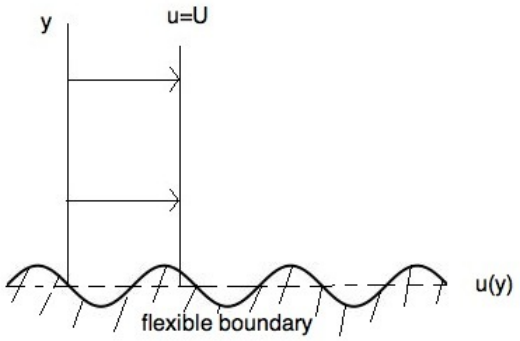

Figure 3.4: Schematic of uniform flow with a flexible boundary

Solving the Rayleigh equation (3.2.10) for the uniform stream, i.e. $U = constant$ for all $y > 0$, subject to the condition that the streamfunction remains bounded at infinity, gives the following solution:

$$\tilde{\psi} = Ae^{-\alpha y}. \tag{3.4.18}$$

In order to solve for the wavespeed c we substitute the solution for the streamfunction in (3.4.18) into the wall condition (3.4.14) at $y = 0$, which gives a quadratic for the wavespeed c:

$$(\alpha - \alpha^2 e_4)c^2 + (-i\alpha e_5 - 2\alpha U)c + (\alpha^4 e_1 - \alpha^2 e_2 + e_3 + \alpha U^2) = 0. \tag{3.4.19}$$

We obtain therefore the following solution for the wavespeed:

$$c = \frac{1}{2(\alpha - \alpha^2 e_4)}\left[i\alpha e_5 + 2\alpha U \pm \sqrt{(i\alpha e_5 + 2\alpha U)^2 - 4(\alpha - \alpha^2 e_4)(\alpha^4 e_1 - \alpha^2 e_2 + e_3 + \alpha U^2)}\right]. \tag{3.4.20}$$

As in subsection 3.4.1 we can plot the dispersion relation for an example of parameters $U = 1$, $e_1 = -1$, $e_2 = 1$, $e_3 = -1$, $e_4 = -1$ and $e_5 = -1$. Taking the positive root, see figure 3.5. And taking the negative root, see figure 3.6. Again we can see that we have instability, in particular at low wavenumbers. The interplay between flow strength and flexibility strength is also clearly present here through the U, $e_1 - e_5$ factors.

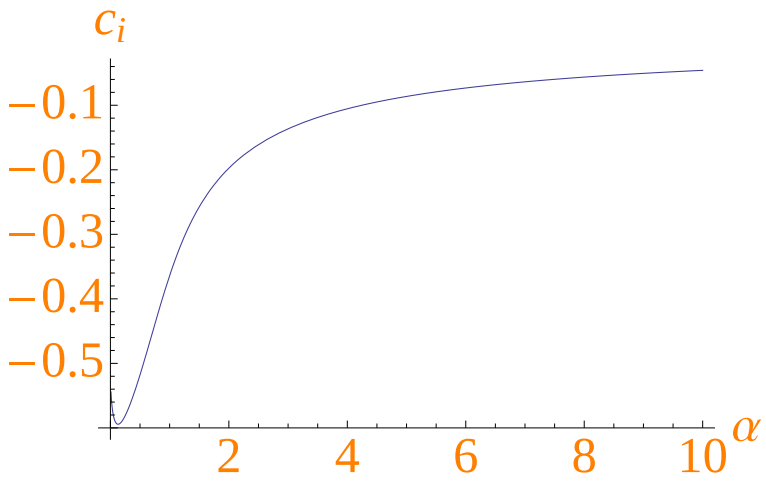

Figure 3.5: Dispersion relation for: $c = \frac{1}{2(\alpha+\alpha^2 e_4)}\left[i\alpha e_5 + 2\alpha U + \sqrt{(i\alpha e_5 + 2\alpha U)^2 - 4(\alpha + \alpha^2 e_4)(\alpha^4 e_1 - \alpha^2 e_2 + e_3 + \alpha U^2)}\right]$.

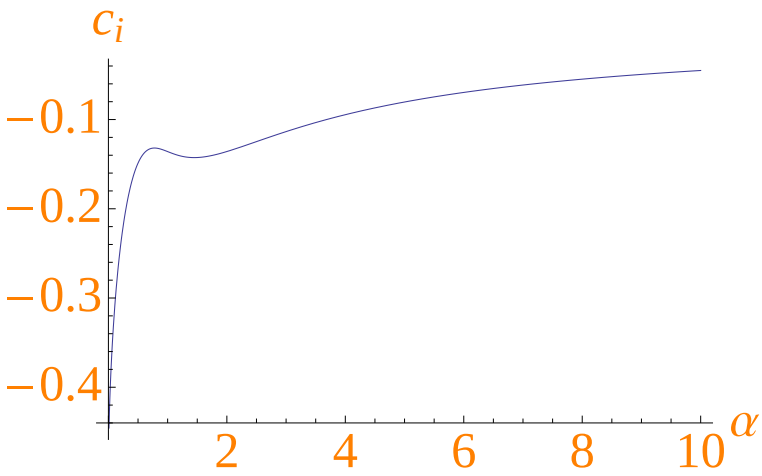

Figure 3.6: dispersion relation for $c = \frac{1}{2(\alpha+\alpha^2 e_4)}\left[i\alpha e_5 + 2\alpha U - \sqrt{(i\alpha e_5 + 2\alpha U)^2 - 4(\alpha+\alpha^2 e_4)(\alpha^4 e_1 - \alpha^2 e_2 + e_3 + \alpha U^2)}\right]$.

3.5 Comparison with solid-wall solution

In the case of a fixed solid wall we need to solve equation (3.4.2) with the jump conditions (3.4.3) and (3.4.4) at any discontinuity in the velocity profile or its slope and the wall condition $\tilde{\psi} = 0$ at $y = 0$.

In the velocity profiles we are considering below we do not have any discontinuities; therefore our solution to equation (3.4.2) is simply:

$$\tilde{\psi}(y) = Ae^{-\alpha y}, \tag{3.5.1}$$

of course. This takes into account that $\tilde{\psi}(y)$ has to be bounded as $y \to \infty$ and A is a constant that needs to be determined by the boundary condition. In the case of the solid wall the boundary condition is $\tilde{\psi}(0) = 0$ as mentioned above. This requires that $A = 0$. This result tells us that there are no linear disturbances of the assumed form present. Comparing this to the results from the section above we can see that by replacing the solid wall with a flexible wall we may in effect introduce some new disturbances. Although these appear to be stable.

These results are encouraging to continue with further work to investigate if these disturbances can give rise to instabilities or changes in instability that arise due to the presence of a flexible wall. In the next chapter we proceed to analyse the flexible-wall conditions in the triple-deck structure which is associated with Tollmien-Schlichting instabilities as in Smith [42] for a fixed solid wall.

Chapter 4

Flexible Wall Conditions in the Triple-Deck Structure

In real-world applications viscous forces are of great importance even at high Reynolds numbers; it is therefore necessary to use an appropriate viscous-inviscid model that includes these. At this stage the triple deck offers a suitable framework for investigating the flow behaviour inside the boundary layer since the triple-deck interaction captures Tollmien-Schlichting wave instabilities, see for example Smith [46, 47]. For a detailed treatment of the triple deck method see for example [31, 57]. In the next section 4.1 the dispersion relation for a flexible wall is derived: see fig 4.1. This dispersion relation is the basis for the rest of the current chapter. All numerical calculations in this chapter have been done by use of a Newton-Raphson method, details of which are described in the subsequent section 4.2.

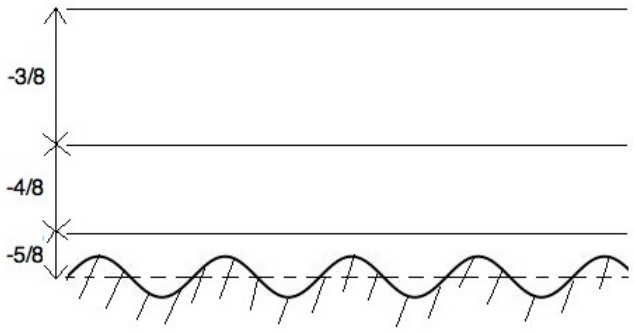

Figure 4.1: schematic diagram of layers in the triple-deck structure

At a later stage we will turn to structures similar to but smaller than the triple-deck case, leading on to the so-called condensed case.

4.1 Derivation of full dispersion relation

The argument here goes analogously to the conventional triple-deck case with a solid wall (see Chapter 2). In triple-deck theory the lower deck is a viscous sublayer close to the wall, the main deck contains the remainder of the boundary layer, and the upper deck lies just outside of the boundary layer. The boundary layer thickness is of order $R_e^{-\frac{1}{2}}$. The only major difference is in the wall condition, see for example [23] for the flexible wall condition. Instead of the no-slip wall condition of a solid wall we have to combine the pressure-shape relation with the kinematic condition. These are given immediately below:

$$P - p_0 = e_1\eta_{xxxx} + e_2\eta_{xx} + e_3\eta + e_4\eta_{tt} + e_5\eta_t, \tag{4.1.1}$$

$$V_W = \eta_t + u\eta_x. \tag{4.1.2}$$

Here P is the pressure, e_i are as defined in section 2.6, with the tilde dropped, η is the wall shape, V_W is the transverse velocity component at the wall and u is the streamwise velocity component.

However since in normalised terms $U = Z + U_1 + ... = 0$ at the wall the kinematic condition (4.1.2) can be expressed in terms of η alone. At the wall, i.e. at $Z = \eta$, we have that $u = \eta + U_1(Z = 0) + U_1'(Z = 0)\eta + ... = 0$, with U small. Hence to leading order we have that $U_1 = -\eta$ at $Z = 0$ and the kinematic condition becomes $V_W = \eta_t - \eta\eta_x$ at the effective wall at $Z = 0$. We still need another condition at the effective wall at $Z = 0$, which comes from the linearised x-momentum equation:

$$U_{1t} + ZU_{1x} + V_1 = -p_x + \tau_Z. \tag{4.1.3}$$

Using the above expressions for V_W and U_1 this simplifies to

$$-\eta\eta_x = -p_x + \tau_Z, \text{ at Z=0.} \tag{4.1.4}$$

where $\tau = U_Z$. Linearising (4.1.4) eliminates the term $-\eta\eta_x$. Now, we need to change variables from Z to the triple deck variable $\zeta = (i\alpha)^{\frac{1}{3}}(Z - \frac{\omega}{\alpha})$ in terms of waves $\propto exp(i\alpha x - i\omega t)$. With $p_x = i\alpha P_1$ effectively, instead of $V_W = 0$ we now obtain the following wall condition:

$$-i\alpha P_1 + U_{1ZZ} = 0. \tag{4.1.5}$$

The rest of the triple-deck equations are as follows. In the lower deck we have $y = \epsilon^5 Z$ and to leading order the equations become:

$$i(Z\alpha - \omega)U_1 + V_1 + i\alpha p_1 - U_{1ZZ} = 0 \qquad \text{x-momentum,} \tag{4.1.6}$$

$$i\alpha U_1 + V_{1Z} = 0 \qquad \text{continuity.} \tag{4.1.7}$$

The boundary condition is:

$$-i\alpha P_1 + U_{1ZZ} = 0 \qquad \text{wall condition at } Z = 0. \tag{4.1.8}$$

We also have the condition of matching with the main deck as $Z \to \infty$. In the main deck we have $y = \epsilon^4 Y$. For small y $U_{By} \to Y$ and to leading order the equations become:

$$U_B i\alpha u_1 + v_1 U_{BY} = i\alpha Y u_1 + v_1 = 0 \qquad x\text{-momentum}, \tag{4.1.9}$$

$$0 = -p_{1Y} \qquad y\text{-momentum}, \tag{4.1.10}$$

$$i\alpha u_1 + v_{1Y} = 0 \qquad \text{continuity}. \tag{4.1.11}$$

Here the boundary conditions are purely matching conditions with the upper deck as $Y \to \infty$ and the lower deck as $Y \to 0$. In the upper deck we have $y = \epsilon^3 \bar{y}$ and to leading order the governing equation becomes the Laplace equation for the pressure in effect:

$$\bar{p}_{1\bar{y}\bar{y}} + \bar{p}_{1xx} = \bar{p}_{1\bar{y}\bar{y}} - \alpha^2 \bar{p}_1 = 0 \qquad \text{governing equation}, \tag{4.1.12}$$

$$\bar{u}_{1x} + \bar{v}_{1\bar{y}} = 0 \qquad \text{continuity}. \tag{4.1.13}$$

Here the boundary conditions consist of one matching condition with the main deck as $\bar{y} \to 0$ and boundedness at infinity, i.e. as $\bar{y} \to \infty$.

The solutions are as follows. In the main deck we make use of the continuity equation (4.1.11) to replace $i\alpha u_1$ by $-v_{1y}$ within the x-momentum equation (4.1.9) and solve for v_1. We derive the following solutions:

$$v_1 = -i\alpha A_1 U_B, \tag{4.1.14}$$

$$u_1 = A_1 U_{BY}, \tag{4.1.15}$$

$$p_1 = P_1. \tag{4.1.16}$$

The constants A_1 and P_1 above need to be determined through matching. In the lower deck we differentiate the x-momentum equation (4.1.5) with respect to x and use the y-momentum equation,

i.e. $P_{1Z} = 0$, and the continuity equation (4.1.6) to obtain

$$i(Z\alpha - \omega)U_{1Z} - U_{1ZZZ} = 0. \tag{4.1.17}$$

Changing variables to $\zeta = (i\alpha)^{\frac{1}{3}}(Z - \frac{\omega}{\alpha})$ as stated previously one obtains Airy's equation for $U_{1\zeta}$:

$$U_{1\zeta} - U_{1\zeta\zeta\zeta} = 0, \tag{4.1.18}$$

with the following solution bounded at infinity:

$$U_{1\zeta} = B_1 Ai(\zeta). \tag{4.1.19}$$

Here Ai is Airy's function. With the above change of variables the wall condition (4.1.8) becomes:

$$-i\alpha P_1 + (i\alpha)^{\frac{2}{3}} U_{1\zeta\zeta} = 0. \tag{4.1.20}$$

Differentiating (4.1.19) and substituting the result into (4.1.20) we can obtain a relation between B_1 and P_1. We find that:

$$B_1 = (i\alpha)^{\frac{1}{3}} \frac{P_1}{Ai'(\zeta_0)}. \tag{4.1.21}$$

Next we need to match U_1 to u_1 from the main or middle deck. To leading order we have $u_1 = A_1 U_{BY} = U_1$. Above we have calculated $U_{1\zeta}$, so we need to integrate this to find U_1. This leads to the relation

$$(i\alpha)^{\frac{1}{3}} \frac{\kappa(\zeta_0)}{Ai'(\zeta_0)} P_1 - \eta = A_1 \tag{4.1.22}$$

where $\kappa = \int_{\zeta_0}^{\infty} Ai(q)dq$ and $\zeta_0 = -(i\alpha)^{\frac{1}{3}} \frac{\omega}{\alpha}$. In the upper deck we have:

$$\bar{p}_1 = \bar{P}_1 e^{-\alpha \bar{y}}. \tag{4.1.23}$$

Here we have assumed that α is positive and have chosen the negative exponential for boundedness at large $\bar{y}$. The last relation between P_1 and A_1 comes from matching the upper deck solution to the middle deck solution. This means that the pressure as well as the normal velocity need to be continuous, i.e. in essence $\bar{p}_1 = \bar{P}_1 = P_1$ as $\bar{y} \to 0$ and $\bar{v}_{1x} = -\bar{p}_{1y} = \alpha \bar{P}_1 e^{-\alpha \bar{y}} \to \alpha \bar{P}_1$ as $\bar{y} \to 0$ while $v_{1x} = -(i\alpha)^2 A_1$ as $Y \to \infty$, apart from exponential factors. Therefore we obtain:

$$P_1 = \alpha A_1. \tag{4.1.24}$$

Making use of the pressure-shape relation (4.1.1) with p_0 omitted for now and substituting the above into (4.1.21) we then obtain the dispersion relation:

$$(i\alpha)^{\frac{1}{3}} \frac{\kappa(\zeta_0)}{Ai'(\zeta_0)} = \frac{1}{e_1\alpha^4 - e_2\alpha^2 + e_3 - e_4\omega^2 - ie_5\omega} + \frac{1}{\alpha}, \tag{4.1.25}$$

or

$$(i\alpha)^{\frac{1}{3}} \frac{\kappa(\zeta_0)}{Ai'(\zeta_0)} = \frac{1}{\chi} + \frac{1}{\alpha}. \tag{4.1.26}$$

Here $\zeta_0 = -(i\alpha)^{(\frac{1}{3})} \frac{\omega}{\alpha}$ and $\chi = e_1\alpha^4 - e_2\alpha^2 + e_3 - e_4\omega^2 - ie_5\omega$. Generally the interest might be expected to lie in the range where ζ_0 is of order unity, suggesting therefore that $\omega \sim \alpha^{(2/3)}$.

We could go on to examine in great detail the instability properties of various different waves by starting with the Tollmien-Schlichting values [46, 47] mentioned above, varying the value of ω regarded as a fixed frequency say and finding the unknown value or values of α which in general must be complex and determines the spatial growth rate or decay rate of the small disturbances. Some work was done along those lines and is presented in the next sections. The following overall approach is felt to be more productive and relevant however partly because it allows flexible sections with finite length to be analyzed and understood much more readily and partly due to the eventual finding in a later chapter that nonlinear effects can be incorporated readily. These finite-length sections are often called blips in the present work and they are believed to correspond perhaps more

closely to practical configurations than do the unbounded cases that form the basis for the work on instability properties described above. The current approach adopted henceforth is founded on four significant features that stem directly from the relation (4.1.26) or from its derivation from the original triple-deck system in (4.1.1-4.1.25).

The first significant feature concerns relatively long length scales and temporal scales associated with small values of α and ω. Here the system becomes dominated by the wall relation (4.1.1) acting as if $P - p_0$ is prescribed (and in fact P is relatively small) and thus determining the wall shape η, after which the combined relation (4.1.26) becomes secondary and determines only a fluid flow correction corresponding to a viscous displacement thickness. This is as in the work on long surface-mounted humps by Smith, Brighton, Jackson and Hunt [58] and it tends to a classical boundary-layer description. Moreover on a longer scale the contribution p_0 varies due to being an effect imposed from the free stream just outside the main boundary layer, or in other words p_0 acts as function of $p_0(x)$ dependent on the body length scale x of O(1) rather than being as if a constant on the local length scale X which has x equal to some x_0 to leading order. Thus a form of interplay between the pressure force induced on a bluff body and the shape of the thin flexible surface on that body may be anticipated over the length scale x of order unity.

The second feature of significance here is for length scales which are shorter than in the case of (4.1.1-4.1.26). Hence in effect the typical alpha and omega values are large with $\omega \sim \alpha^{(\frac{2}{3})}$. The left-hand side of (4.1.15) is then large of order $\alpha^{(\frac{1}{3})}$ whereas the second term on the right-hand side is small as it is of order $\alpha^{(-1)}$. So in general we would expect the first term on the right-hand side of (4.1.26) to balance against the left-hand contribution. The way in which this balancing actually occurs is dependent on what are the largest factors within χ itself, which in turn depends on the values of the constants $e_1 - e_5$ and these are quite sensitive coefficients as we can see elsewhere in the thesis. However, to give an example, if the e_2 contribution is the largest then the balancing involved would have to be $\alpha^{(\frac{7}{3})}\, e_2^{(-1)}$ from (4.1.25-4.1.26) together with e_2 being small. The balance is in a sense between the flow force and the wall-flexibility force as represented respectively by the left-hand side and the first term on the right in (4.1.26). The neglect of the other force, given by

the $\frac{1}{\alpha}$ term, is equivalent to there being an absence of any substantial effect from the free stream as in Smith, Brighton, Jackson and Hunt [58] and is the opposite of that outlined for the first feature in the previous paragraph. Here we obtain the condensed setting of [46], with or without the unsteady effects contributing to the dynamics. This setting is taken up in a later chapter.

Third is the significant feature that resonance is clearly a distinct possibility. This is evident in the fact that the denominator χ in (4.1.25) or (4.1.26) can tend to zero, depending on α, ω and the details of the coefficients $e_1 - e_5$. An alternative form of resonance which holds for blips of finite length rather than the quasi-infinite ones supposed in (4.1.1-4.1.26) is for the χ effect to be in balance with another effect. The latter form is found to arise in scenarios that are discussed later on and includes single as well as multiple blips of finite length.

Fourth, along with the above aspects, it is found that the current approach can extend well to finite-length blip configurations in three spatial dimensions.

The thesis follows through on these four significant features in the subsequent chapters.

4.2 The Newton-Raphson method

To derive the Newton-Raphson method for a system of equations we start with Taylor expansion of the function $f_i(\underline{x})$ about the point $\underline{x}$:

$$f_i(\underline{x} + \Delta\underline{x}) = f_i(\underline{x}) + \sum_{j=1}^{n} \frac{\partial f_i}{\partial x_j} \Delta x_j + O(\Delta x^2). \tag{4.2.1}$$

We then linearize, i.e. dropping terms $O(\Delta x^2)$, this gives:

$$\underline{f}(\underline{x} + \Delta\underline{x}) = \underline{f}(\underline{x}) + \underline{J}(\underline{x})\Delta\underline{x}. \tag{4.2.2}$$

where $\underline{J}(\underline{x})$ is the Jacobian matrix:

$$J_{ij} = \frac{\partial f_i}{\partial x_j}. \tag{4.2.3}$$

Now, $\underline{x}$ is assumed to be the current approximation of the solution to $\underline{f}(\underline{x}) = \underline{0}$, and $\underline{x} + \Delta\underline{x}$ is the improved solution. The next step is to find $\Delta\underline{x}$. This is done by setting $\underline{f}(\underline{x} + \Delta\underline{x}) = \underline{0}$ and solving the following set of linear equations:

$$\underline{J}(\underline{x})\Delta\underline{x} = -\underline{f}(\underline{x}). \tag{4.2.4}$$

In other words the Newton-Raphson method is made up of the following steps:

1. Estimate the solution vector $\underline{x}$
2. Evaluate $\underline{f}(\underline{x})$
3. Compute the Jacobian matrix $\underline{J}(\underline{x})$ from $J_{ij} = \frac{\partial f_i}{\partial x_j}$
4. Set up the simultaneous equations $\underline{J}(\underline{x})\Delta\underline{x} = -\underline{f}(\underline{x})$ and solve for $\Delta\underline{x}$
5. Let $\underline{x} \to \underline{x} + \Delta\underline{x}$ and repeat steps 2-5.

The process is repeated until a break-off condition is fulfilled. In this case $\Delta\underline{x}$ needs to be smaller than some error tolerance ϵ. It should be noted that the Newton-Raphson procedure is very sensitive to the initial estimate of $\underline{x}$. It converges very quickly if the estimate is good but can give inaccurate results otherwise.

The procedure was implemented in Mathematica as follows:
$f_1 = Re[g[\alpha_r + i\alpha_i]]$
$f_2 = Im[g[\alpha_r + i\alpha_i]]$.

Here $g[\alpha_r + i\alpha_i]$ is the dispersion relation, written in the form such that the right-hand-side is equal

to zero.

The Jacobian is calculated from:

$$\underline{J}(\alpha_r, \alpha_i) = \begin{bmatrix} \frac{\partial f_1}{\partial \alpha_r} & \frac{\partial f_1}{\partial \alpha_i} \\ \frac{\partial f_2}{\partial \alpha_r} & \frac{\partial f_2}{\partial \alpha_i} \end{bmatrix},$$

where:

$\frac{\partial f_1}{\partial \alpha_r} \approx \frac{f_1(\alpha_r+i\alpha_i+h)-f_1(\alpha_r+i\alpha_i)}{h}$

$\frac{\partial f_1}{\partial \alpha_i} \approx \frac{f_1(\alpha_r+i\alpha_i+ih)-f_1(\alpha_r+i\alpha_i)}{h}$

$\frac{\partial f_2}{\partial \alpha_r} \approx \frac{f_2(\alpha_r+i\alpha_i+h)-f_2(\alpha_r+i\alpha_i)}{h}$

$\frac{\partial f_2}{\partial \alpha_i} \approx \frac{f_2(\alpha_r+i\alpha_i+ih)-f_2(\alpha_r+i\alpha_i)}{h}$.

The implemented procedure was tested extensively for the known Tollmien-Schlichting dispersion relation. It was found to give results in agreement with established results.

4.3 Results for the time-dependent reduced p-η case

In this section we examine a simplified time-dependent problem, where we ignore the two spatial derivatives, i.e. we only include parameters e_3, e_4 and e_5 and omit e_1 and e_2. Thus now,

$$(i\alpha)^{\frac{1}{3}} \frac{\kappa(\zeta_0)}{Ai'(\zeta_0)} = \frac{1}{e_3 - e_4\omega^2 - ie_5\omega} + \frac{1}{\alpha}, \tag{4.3.1}$$

from (4.1.25). This approximation of the pressure-shape relation is analogous to the one used in the investigation by Green at al [38], which in turn refers to Larose and Grotberg [59] and Gaver et al [60] among others. The instability results for (4.3.1) are presented in figures 4.2 - 4.7 for a number of different representative values of the e_3 - e_5 parameters. These results show the flexible-wall dispersion relation in blue which over most of the range is indistinguishable from the solid-wall solution in purple. However, for some cases of parameters ($e_4 = 10$ and $e_3 = 10^{-3}$ as well as $e_4 = 10$

and $e_3 = 10^{-4}$ below), we can see a deviation at small frequencies.

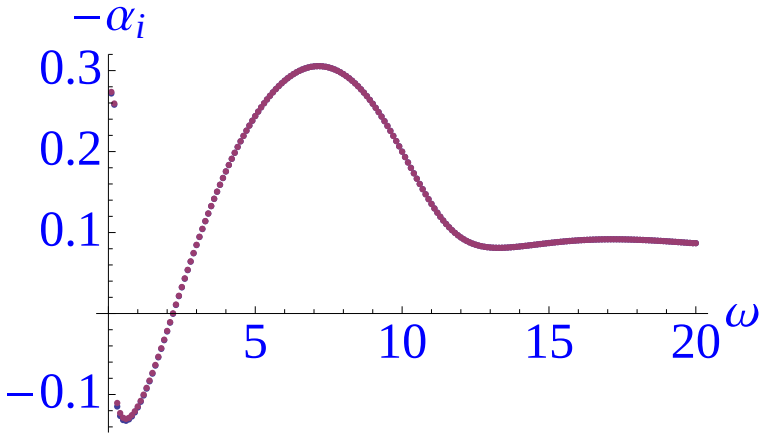

Figure 4.2: scaled spatial growth rate for: $e_4 = 10^2$; $e_3 = 10^{-3}$; $e_5 = 0$

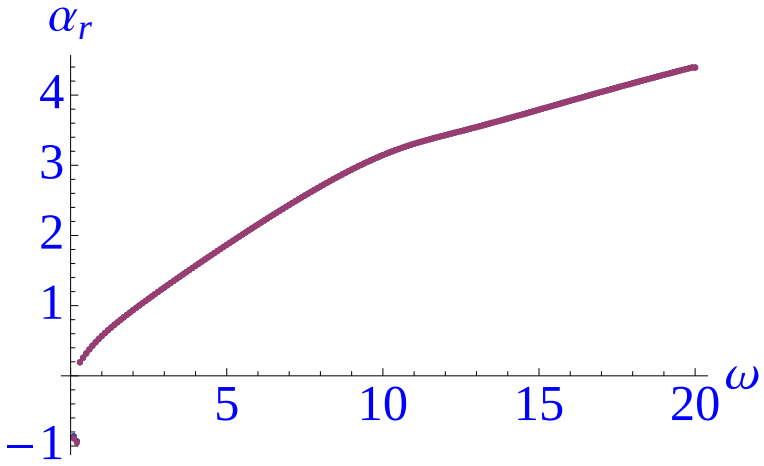

Figure 4.3: scaled wavenumber for: $e_4 = 10^2$; $e_3 = 10^{-3}$; $e_5 = 0$

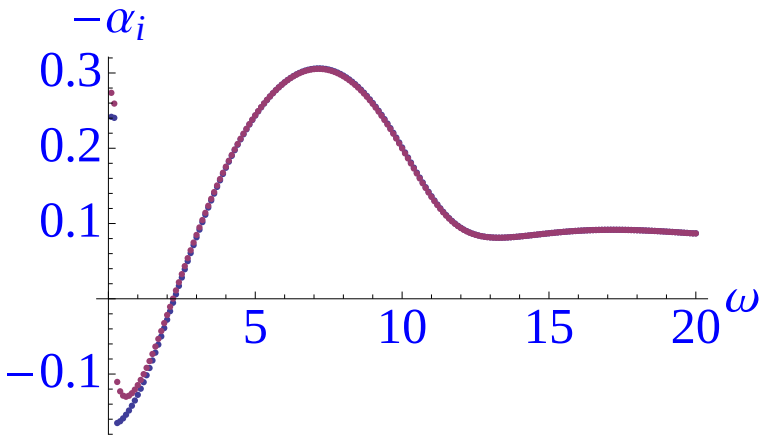

Figure 4.4: scaled spatial growth rate for: $e_4 = 10$; $e_3 = 10^{-3}$; $e_5 = 0$

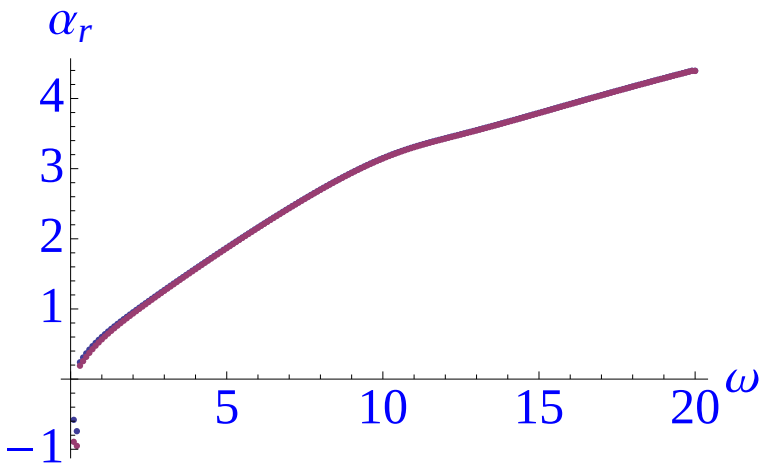

Figure 4.5: scaled wavenumber for: $e_4 = 10$; $e_3 = 10^{-3}$; $e_5 = 0$

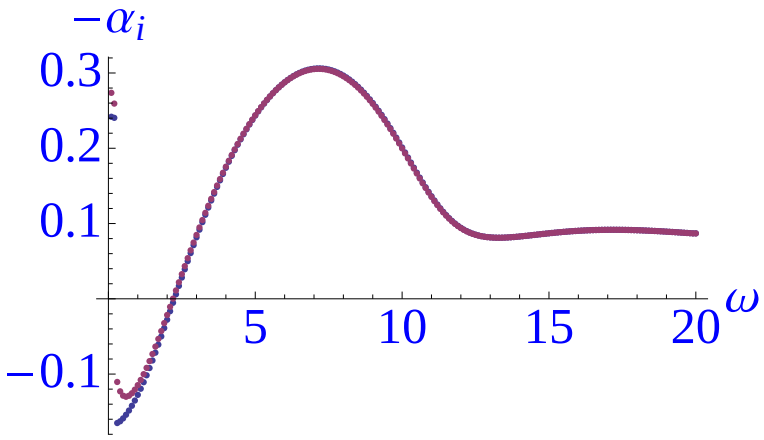

Figure 4.6: scaled spatial growth rate for: $e_4 = 10$; $e_3 = 10^{-4}$; $e_5 = 0$

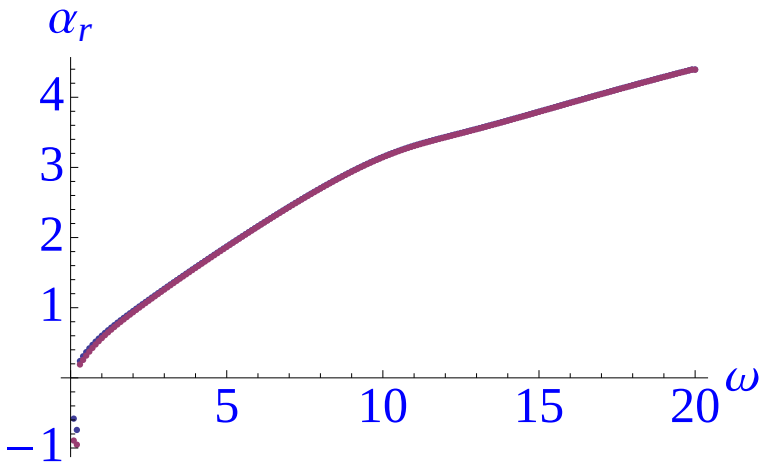

Figure 4.7: scaled wavenumber for: $e_4 = 10$; $e_3 = 10^{-4}$; $e_5 = 0$

4.4 Results for the time-independent reduced p-η case

In this section we consider a time-independent approximation to the flexible-wall relation, i.e. we examine the case

$$e_1 \frac{\partial^4 \eta}{\partial x^4} + e_2 \frac{\partial^2 \eta}{\partial x^2} + e_3 \eta = P - p_0. \tag{4.4.1}$$

This leads from (4.11a) to the following dispersion relation:

$$(i\alpha)^{\frac{1}{3}}\frac{\kappa(\zeta_0)}{Ai'(\zeta_0)} = \frac{1}{e_1\alpha^4 - e_2\alpha^2 + e_3} + \frac{1}{\alpha}. \tag{4.4.2}$$

We investigate the effects of varying each of the parameters e_i in turn. These results show again the flexible-wall dispersion relation in blue and the solid-wall dispersion relation in purple. In figures 4.6 and 4.7 we can see some deviation from the solid wall dispersion relation at small frequencies. Next we will increase each parameter in turn, see figures 4.7-4.12. Increasing each parameter seems to decrease the flexibility effect. So we will decrease the parameters e_1 and e_2, see figures 4.13-4.17. The kink in the graphs in figures 4.18 and 4.19 might at first indicate some difficulty being encountered with the Airy function, which we call from Mathematica's library. So in figure 4.20 we plot the real and imaginary parts of $(i\alpha)^{\frac{1}{3}}$ for the case of figures 4.18, 4.19. These are found to remain positive, as assumed. Decreasing the parameters increases the flexibility effect. This is especially so for decreasing e_1, which shifts almost the whole curve of the dispersion relation relative to the solid-wall solution, see figures 4.21 and 4.22. However for larger frequency values the flexible-wall dispersion recovers to that of the solid-wall solution.

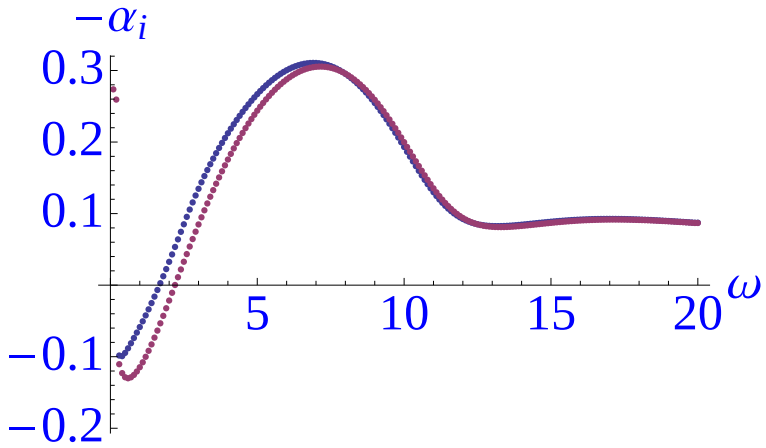

Figure 4.8: scaled spatial growth rate for: $e_1 = -1$; $e_2 = 1$; $e_3 = -1$

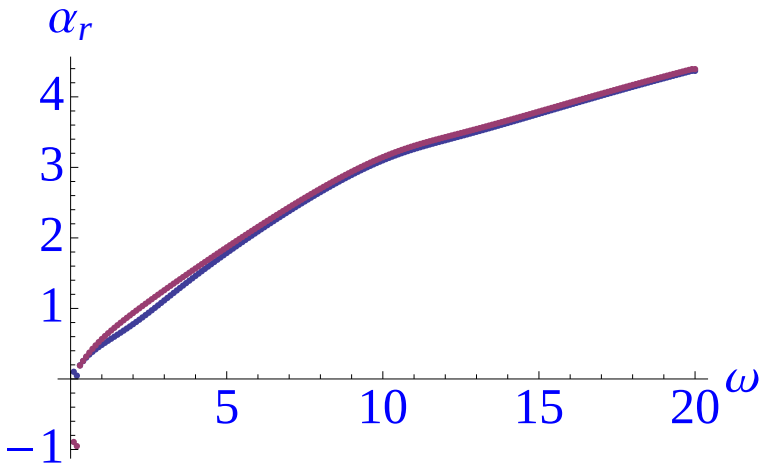

Figure 4.9: scaled wavenumber for: $e_1 = -1$; $e_2 = 1$; $e_3 = -1$

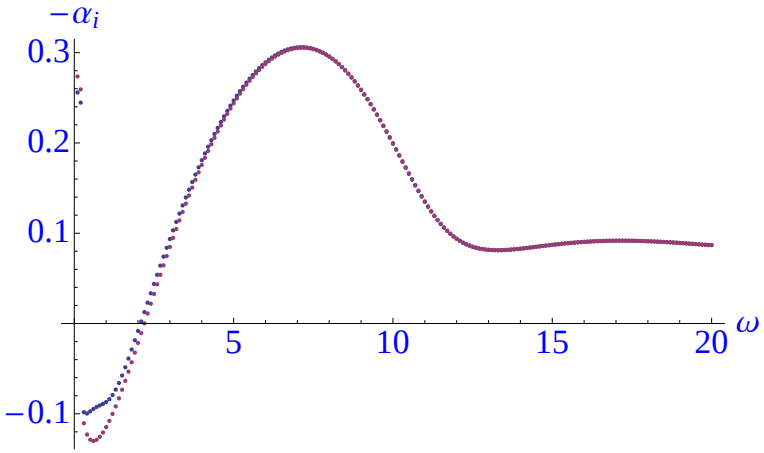

Figure 4.10: scaled spatial growth rate for: $e_1 = -10$; $e_2 = 1$; $e_3 = -1$

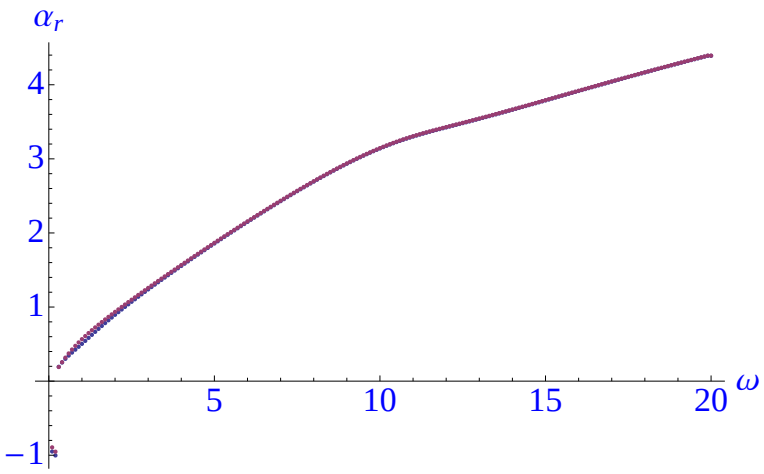

Figure 4.11: scaled wavenumber for: $e_1 = -10$; $e_2 = 1$; $e_3 = -1$

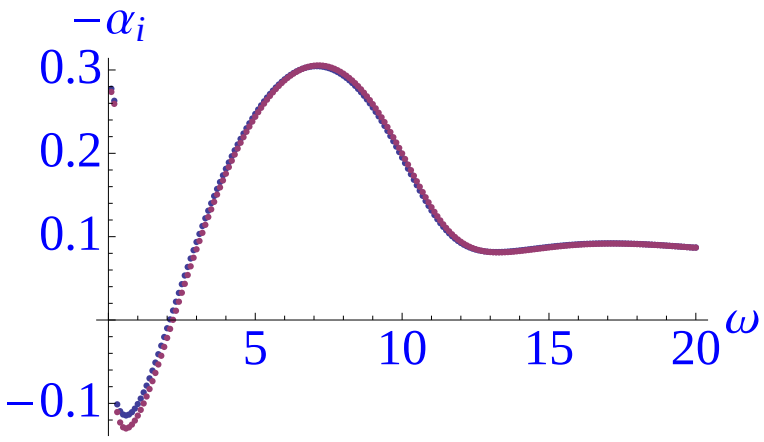

Figure 4.12: scaled spatial growth rate for: $e_1 = -1$; $e_2 = 10$; $e_3 = -1$

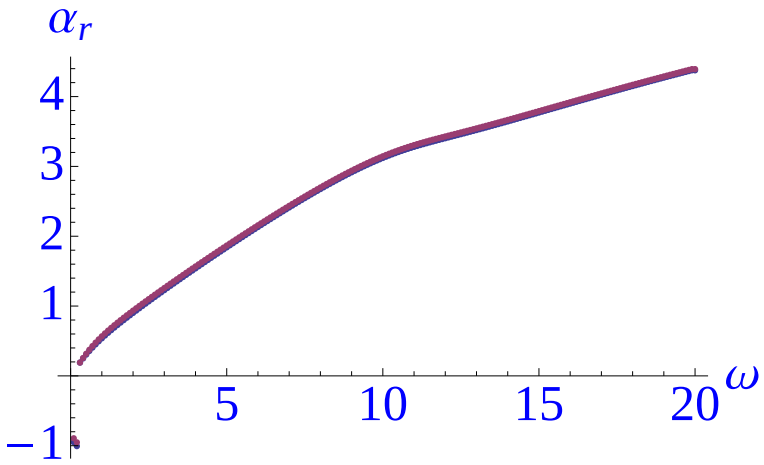

Figure 4.13: scaled wavenumber for: $e_1 = -1$; $e_2 = 10$; $e_3 = -1$

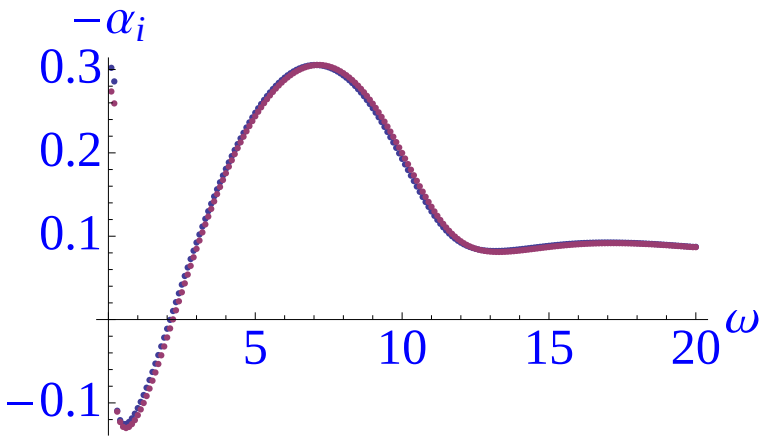

Figure 4.14: scaled spatial growth rate for: $e_1 = -1$; $e_2 = 1$; $e_3 = -10$

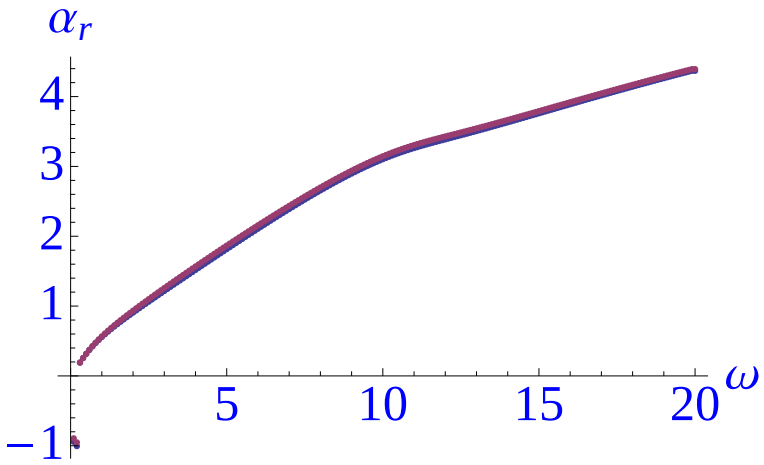

Figure 4.15: scaled wavenumber for: $e_1 = -1$; $e_2 = 1$; $e_3 = -10$

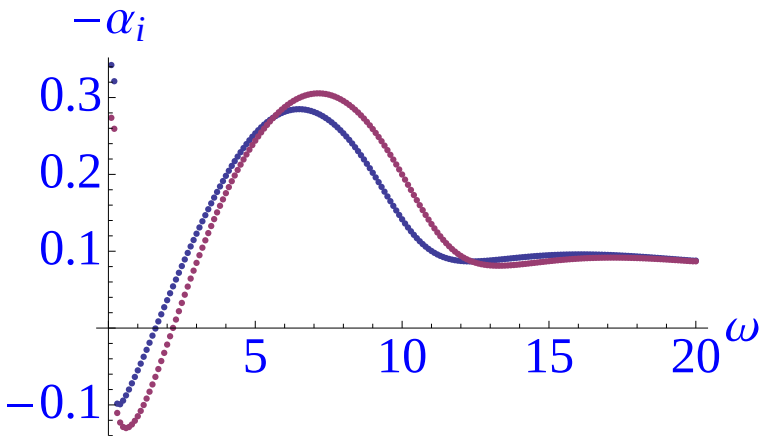

Figure 4.16: scaled spatial growth rate for: $e_1 = -0.1$; $e_2 = 1$; $e_3 = -1$

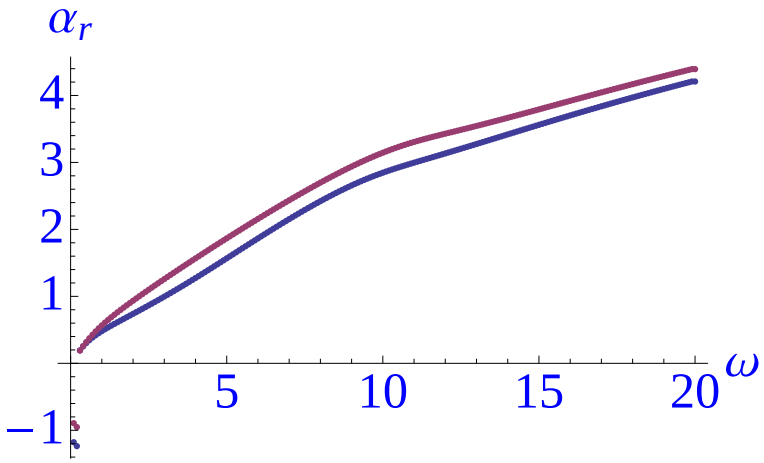

Figure 4.17: scaled wavenumber for: $e_1 = -0.1$; $e_2 = 1$; $e_3 = -1$

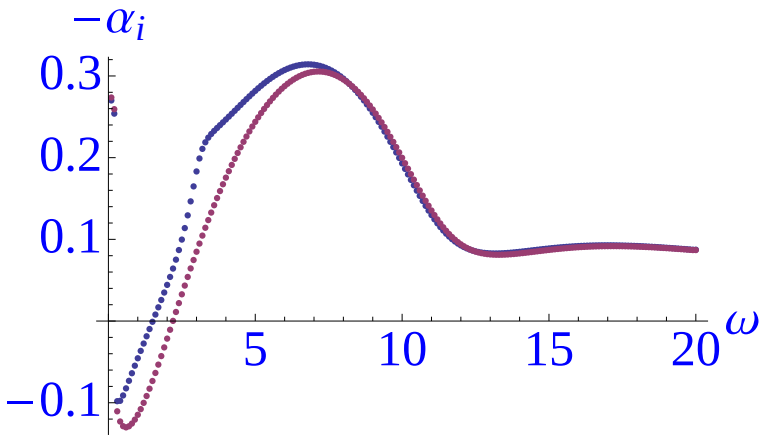

Figure 4.18: scaled spatial growth rate for: $e_1 = -1$; $e_2 = 0.1$; $e_3 = -1$

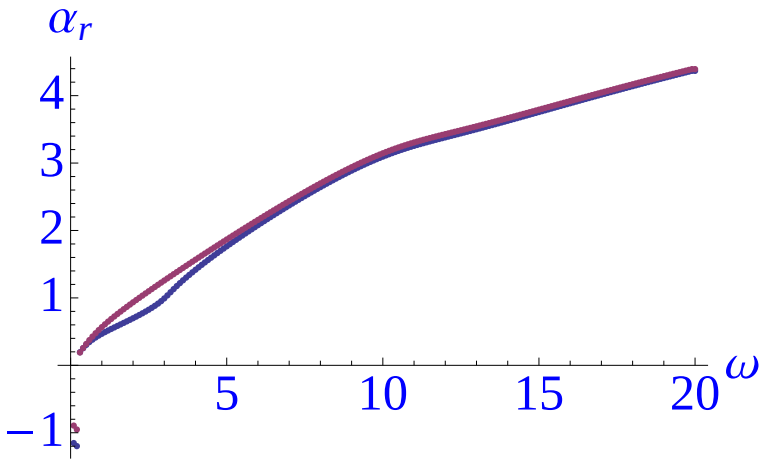

Figure 4.19: scaled wavenumber for: $e_1 = -1$; $e_2 = 0.1$; $e_3 = -1$

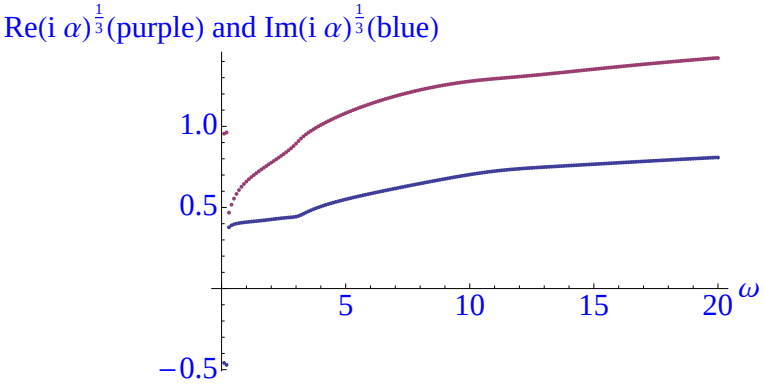

Figure 4.20: $(i\alpha)^{\frac{1}{3}}$ for: $e_1 = -1$; $e_2 = 0.1$; $e_3 = -1$

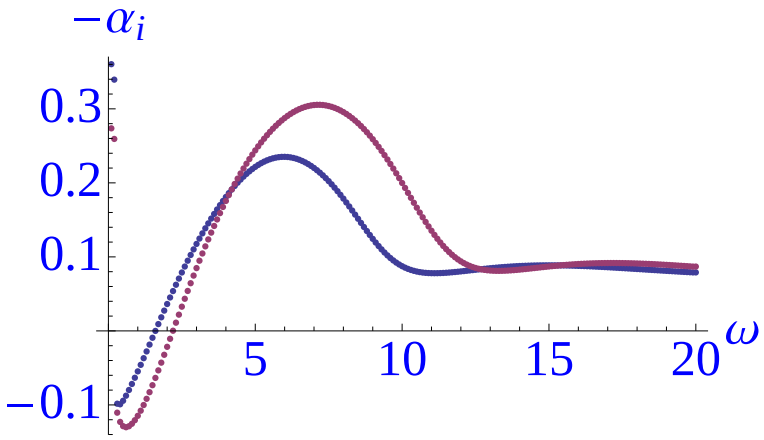

Figure 4.21: scaled spatial growth rate for: $e_1 = -0.01$; $e_2 = 1$; $e_3 = -1$

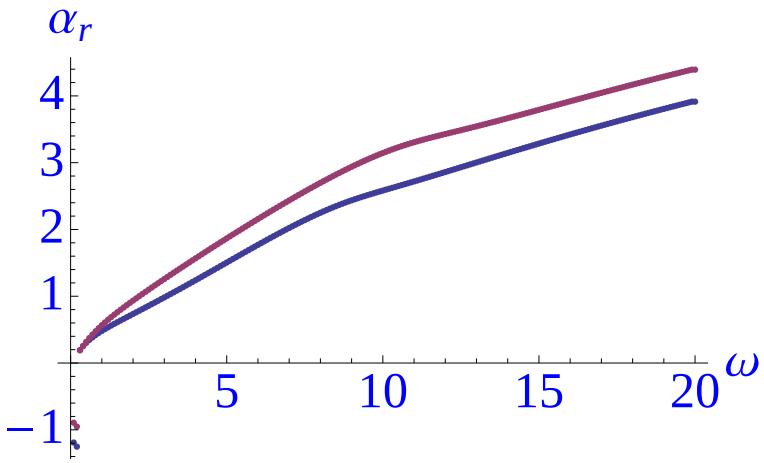

Figure 4.22: scaled wavenumber for: $e_1 = -0.01$; $e_2 = 1$; $e_3 = -1$

4.5 Results for the full dispersion relation

In this section we consider the full dispersion relation from equation (4.1.25):

$$(i\alpha)^{\frac{1}{3}} \frac{\kappa(\zeta_0)}{Ai'(\zeta_0)} = \frac{1}{e_1\alpha^4 - e_2\alpha^2 + e_3 - e_4\omega^2 - ie_5\omega} + \frac{1}{\alpha}. \tag{4.5.1}$$

As above we have the solid-wall solution in purple and the flexible-wall solution in blue. Results are given in figures 4.23 - 4.37. Again we vary the magnitude of some of the parameters, see figures 4.25 and 4.26.

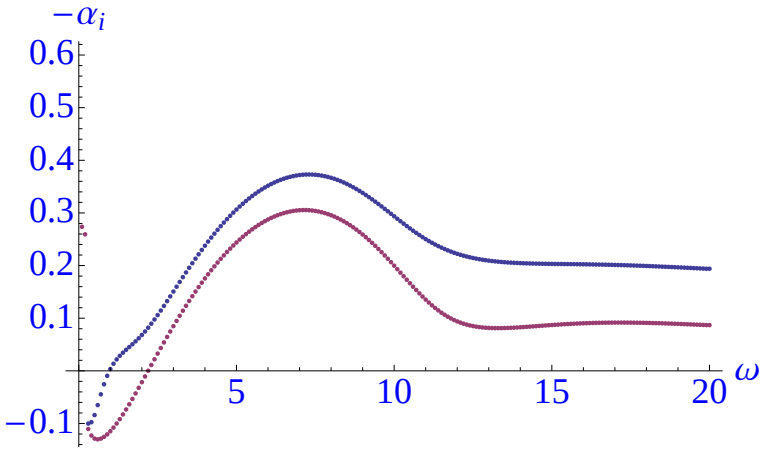

Figure 4.23: scaled spatial growth rate for: $e_1 = -1$; $e_2 = 1$; $e_3 = -1$; $e_4 = -1$; $e_5 = -1$

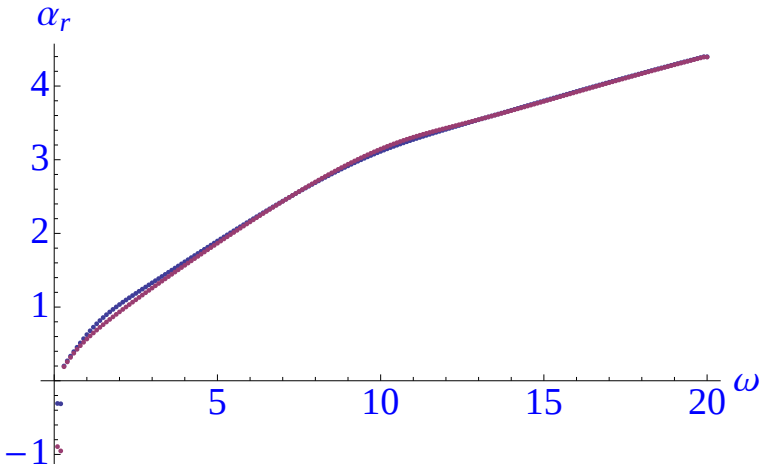

Figure 4.24: scaled wavenumber for: $e_1 = -1$; $e_2 = 1$; $e_3 = -1$; $e_4 = -1$; $e_5 = -1$

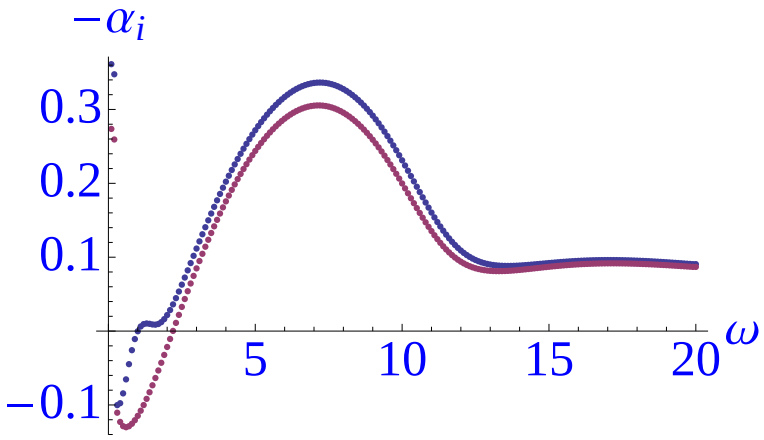

Figure 4.25: scaled spatial growth rate for: $e_1 = -0.1$; $e_2 = 1$; $e_3 = -1$; $e_4 = -1$; $e_5 = -1$

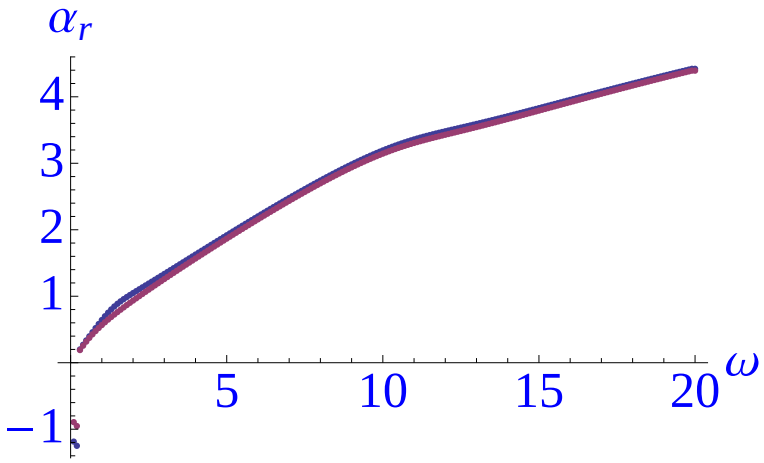

Figure 4.26: scaled wavenumber for: $e_1 = -0.1$; $e_2 = 1$; $e_3 = -1$; $e_4 = -1$; $e_5 = -1$

The kink in the graphs here might at first indicate some difficulty being encountered with the Airy function, which we call from Mathematica's library. So below we plot the real and imaginary parts of $(i\alpha)^{\frac{1}{3}}$ for the case of figures 4.25, 4.26. These are found to remain positive, as assumed.

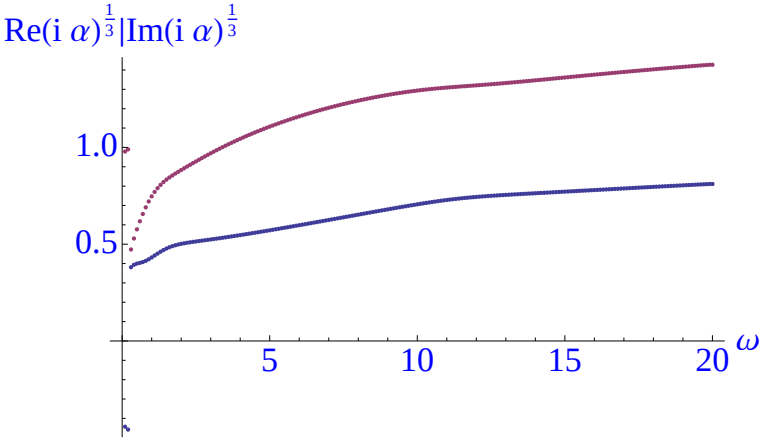

Figure 4.27: $(i\alpha)^{\frac{1}{3}}$ for: $e_1 = -0.1$; $e_2 = 1$; $e_3 = -1$; $e_4 = -1$; $e_5 = -1$

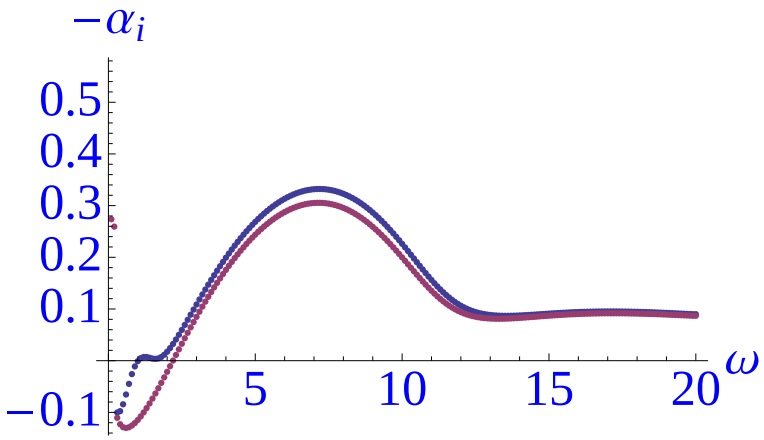

Figure 4.28: scaled spatial growth rate for: $e_1 = -0.01$; $e_2 = 1$; $e_3 = -1$; $e_4 = -1$; $e_5 = -1$

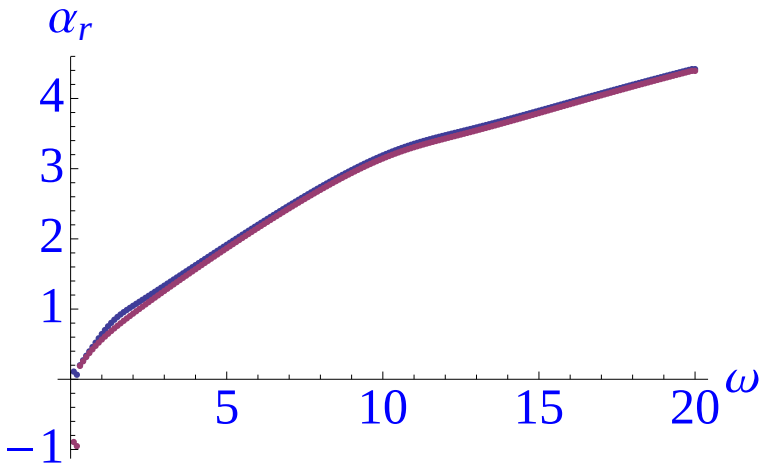

Figure 4.29: scaled wavenumber for: $e_1 = -0.01$; $e_2 = 1$; $e_3 = -1$; $e_4 = -1$; $e_5 = -1$

The kink in the graphs might indicate some problem with the Airy function, which we call from Mathematica's library. So below we plot the real and imaginary parts of $(i\alpha)^{\frac{1}{3}}$.

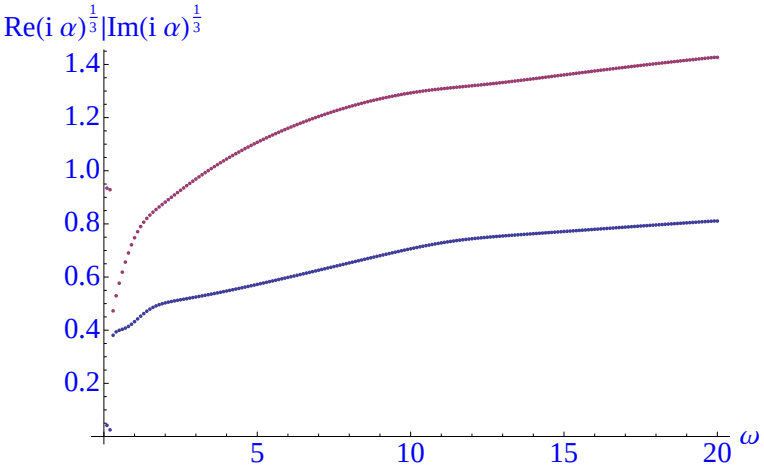

Figure 4.30: $(i\alpha)^{\frac{1}{3}}$ for: $e_1 = -.001$; $e_2 = 1$; $e_3 = -1$; $e_4 = -1$; $e_5 = -1$

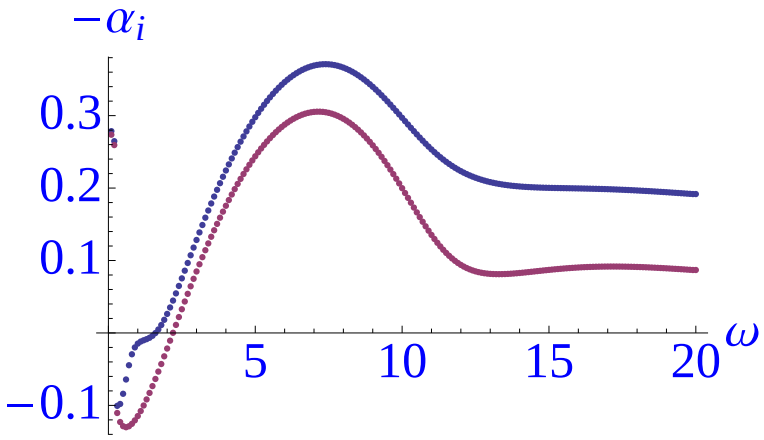

Figure 4.31: scaled spatial growth rate for: $e_1 = -1$; $e_2 = 0.1$; $e_3 = -1$; $e_4 = -1$; $e_5 = -1$

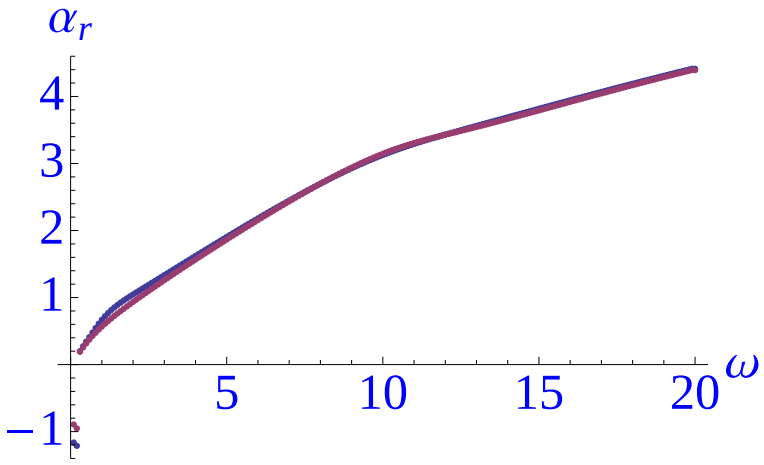

Figure 4.32: scaled wavenumber for: $e_1 = -1$; $e_2 = 0.1$; $e_3 = -1$; $e_4 = -1$; $e_5 = -1$

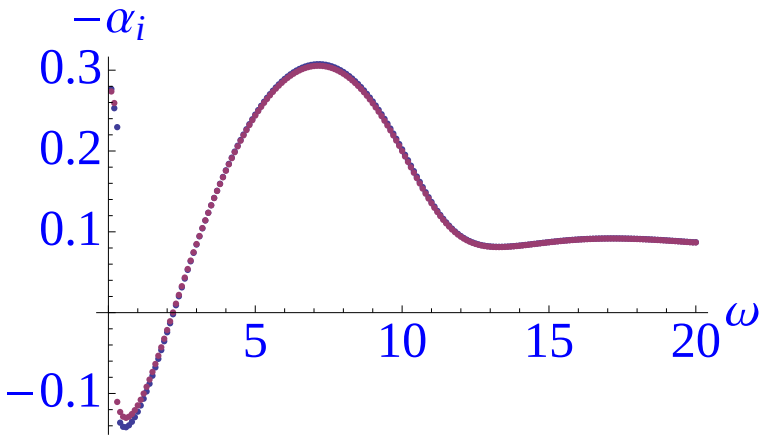

Figure 4.33: scaled spatial growth rate for: $e_1 = -1$; $e_2 = 1$; $e_3 = -1$; $e_4 = -10$; $e_5 = -1$

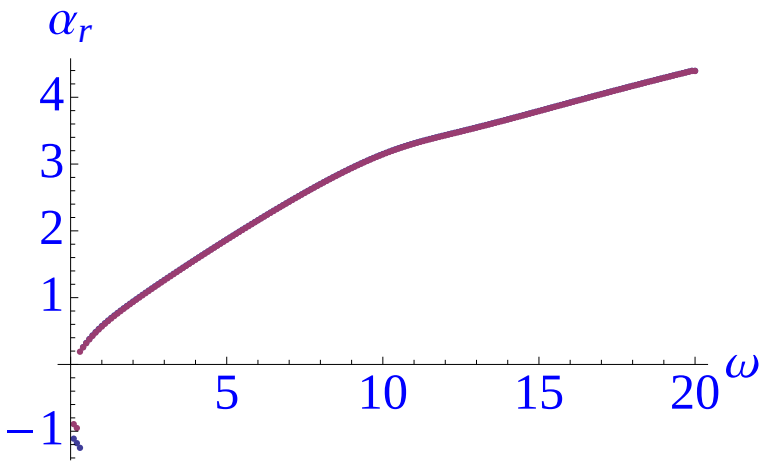

Figure 4.34: scaled wavenumber for: $e_1 = -1$; $e_2 = 1$; $e_3 = -1$; $e_4 = -10$; $e_5 = -1$

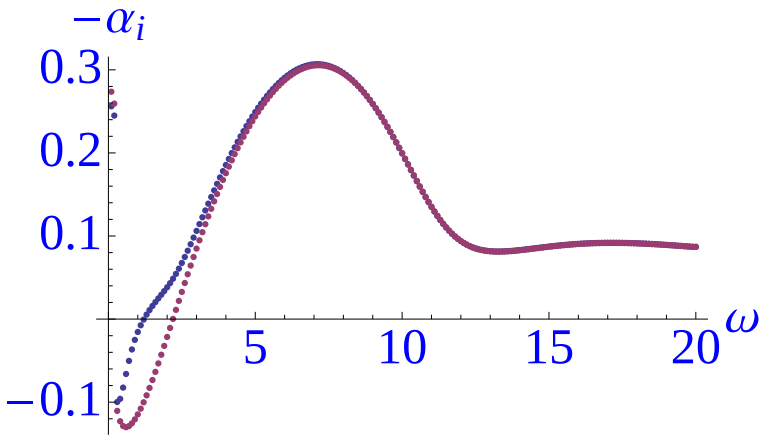

Figure 4.35: scaled spatial growth rate for: $e_1 = -10$; $e_2 = 1$; $e_3 = -1$; $e_4 = -1$; $e_5 = -1$

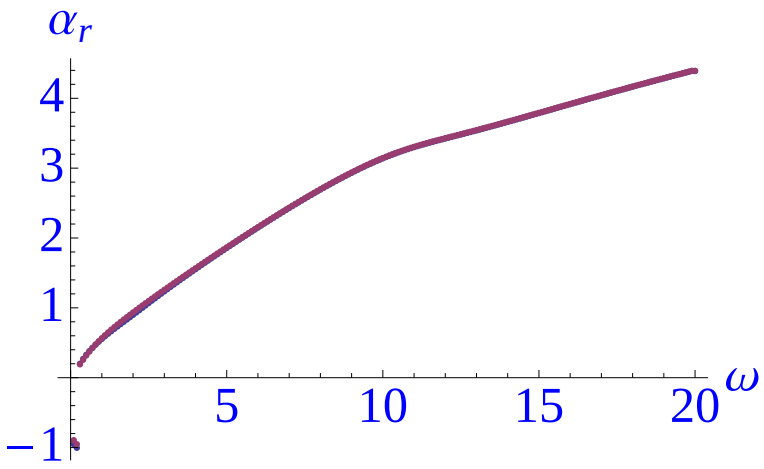

Figure 4.36: scaled wavenumber for: $e_1 = -10$; $e_2 = 1$; $e_3 = -1$; $e_4 = -1$; $e_5 = -1$

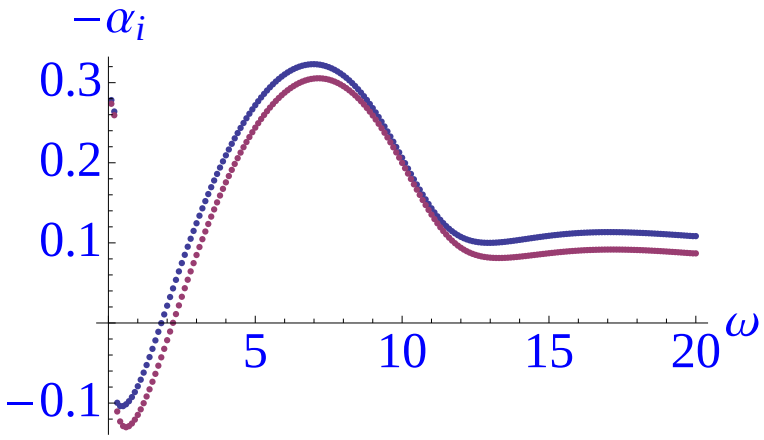

Figure 4.37: scaled spatial growth rate for: $e_1 = -1$; $e_2 = 10$; $e_3 = -1$; $e_4 = -1$; $e_5 = -1$

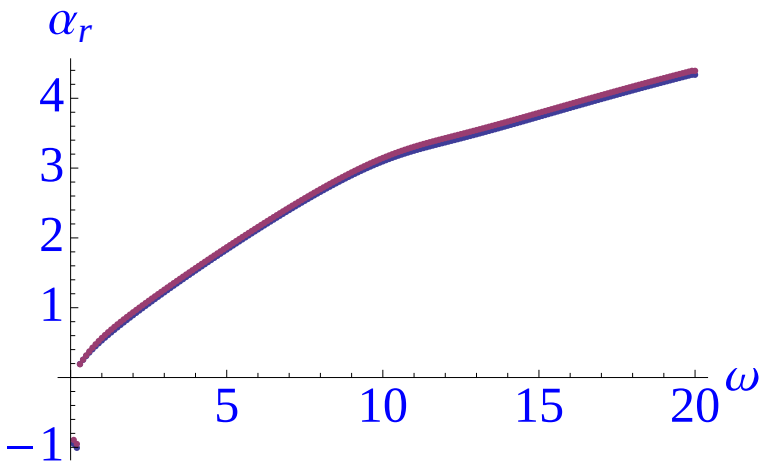

Figure 4.38: scaled wavenumber for: $e_1 = -1$; $e_2 = 10$; $e_3 = -1$; $e_4 = -1$; $e_5 = -1$

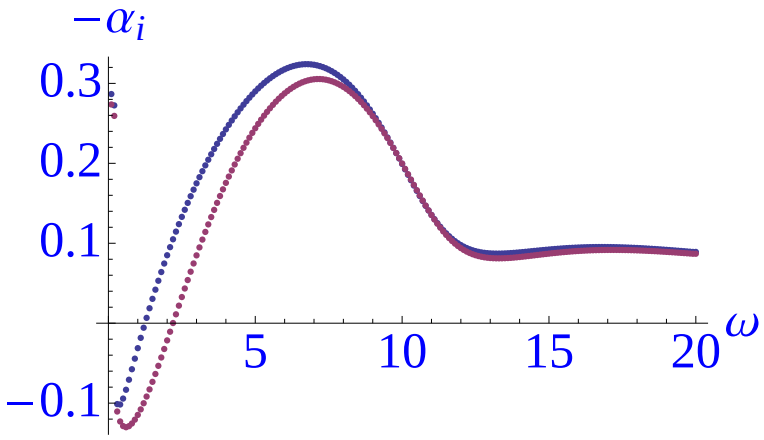

Figure 4.39: scaled spatial growth rate for: $e_1 = -1$; $e_2 = 1$; $e_3 = -1$; $e_4 = -10$; $e_5 = -1$

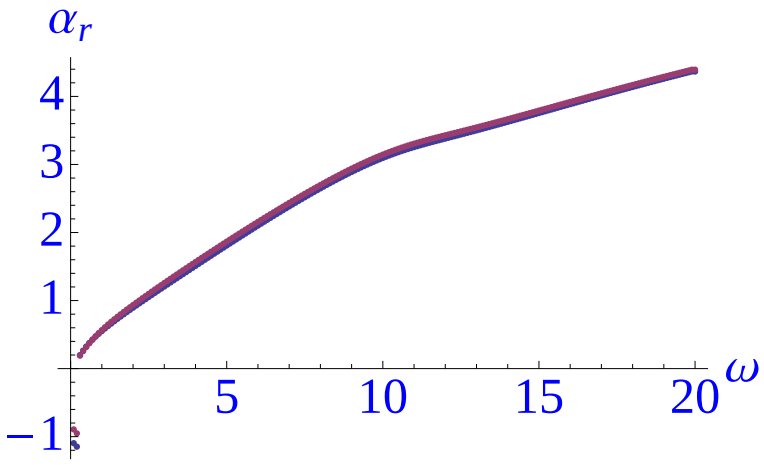

Figure 4.40: scaled wavenumber for: $e_1 = -1$; $e_2 = 1$; $e_3 = -1$; $e_4 = -10$; $e_5 = -1$

The full dispersion relation gives some results where the whole curve of the flexible-wall solution is displaced with respect to the solid-wall dispersion relation. This effect seems largest when all parameters e_i are of the same magnitude. Decreasing the magnitude of e_1 does not have as much an effect on the results of the full dispersion relation (with all other parameters of magnitude one) as in the time-independent solution in the previous section. Decreasing e_2 on the other hand seems to have a larger effect on the full dispersion relation (with all other parameters of magnitude one)

than it has on the time-independent solution in the previous section.

In all of the above results there are some data points at small ω which do not lie on the main curve. These points could indicate a different branch or they could simply be numerical glitches. To determine the nature of these data points further analysis could be done. However, it has been considered more useful to concentrate on finite blips of flexible material instead.

Chapter 5

Flexible Wall Conditions on the Boundary Layer Scale and Large Blips

In this chapter we are considering larger blip sizes as indicated in fig 5.1. This aspect corresponds to the scaling given in section 4.1, $\bar{e}_1 = -\frac{hB}{\rho U^2 L^3}$, $\bar{e}_2 = \frac{hT_t}{\rho U^2 L}$, $\bar{e}_3 = -\frac{h\kappa L}{\rho U^2}$, $\bar{e}_4 = -\frac{hM}{\rho L}$, $\bar{e}_5 = -\frac{hC}{\rho U}$, where the constants $\bar{e}_1 - \bar{e}_5$ are generally of order unity.

Properties of instability have been found in chapter 3 for these longer length scales but there are good reasons to focus more on certain interesting steady-flow features since these features can remain intact and affect the global flow behaviour past a bluff body in particular substantially in principle. Therefore we move on to investigate steady-flow properties instead of instabilities. In section 5.1 we will examine steady-flow properties on the boundary layer length scale. In section 5.3 we will examine large blips, which span from the front stagnation point to the separation point. For this we make use of the computational method of variation of parameters, details of which can be found in section 5.2.

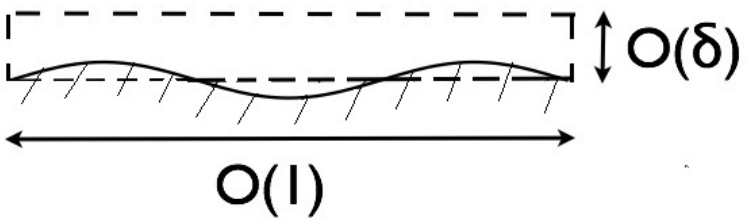

Figure 5.1: schematic for the boundary layer. Here $\delta \sim Re^{-\frac{1}{2}}$ is the typical boundary-layer thickness as well as the representative height or depth of the blip, over an O(1) length scale in the streamwise direction.

5.1 Boundary Layer Scale

For smaller scaled frequencies ω in chapter 4 the wavelength of the disturbances becomes large and the whole boundary layer may be affected. In this case the x-scale becomes of order one rather than the short length scale of the previous chapter. With this new scaling the Navier-Stokes equations reduce to the classical boundary-layer equations

$$u_t + uu_x + vu_y = -p_x + u_{yy}, \tag{5.1.1}$$

$$p_y = 0, \tag{5.1.2}$$

$$u_x + v_y = 0. \tag{5.1.3}$$

The boundary conditions are the pressure shape relation and the kinematic condition at the wall and matching to the outer flow such that $u \to u_e(x,t)$ say as $y \to \infty$. Concerning the wall we have

$$p - p_0 = \bar{e}_3\eta + \bar{e}_2\eta_{xx} + \bar{e}_1\eta_{xxxx} \text{ (pressure-shape relation)}, \tag{5.1.4}$$

$$v = \eta_t + u\eta_x \text{ (kinematic condition) at } y = \eta. \tag{5.1.5}$$

We are seeking solutions of a flow over an unknown surface shape η which is assumed to differ by an $O(\delta)$ amount vertically from the flat surface. A convenient technique to use is the "Prandtl transposition" [31, 61]. For this technique we shift v and y in the form

$$y = \eta + \bar{y}, \tag{5.1.6}$$

$$v = \eta_t + u\eta_x + \bar{v}. \tag{5.1.7}$$

This implies the same boundary-layer equations hold as for the flat surface but for the variables $(x, \bar{y}, t, u, \bar{v}, p)$ with the simpler boundary conditions

$$u = \bar{v} = 0 \text{ at } \bar{y} = 0, \tag{5.1.8}$$

$$u \to u_e(x, t) \text{ as } \bar{y} \to \infty. \tag{5.1.9}$$

In a sense the boundary layer rides up and over the surface shape. The pressure is determined from matching with the known outer flow pressure using

$$u_{et} + u_e u_{ex} = -p_x(x, t), \tag{5.1.10}$$

where u_e is the external flow velocity. Making use of the pressure shape relation (5.1.4) we can then determine the shape function η.

5.2 Variation of parameters

We are given the steady pressure-shape relation

$$\bar{e}_1\eta_{xxxx} + \bar{e}_2\eta_{xx} + \bar{e}_3\eta = p(x) - p_0 \tag{5.2.1}$$

for convenience; we call the right hand side of (5.2.1) $b(x)$, i.e. $b(x) = p(x) - p_0$, which is the given pressure distribution in essence. The first step of this method is to calculate the roots of the complementary equation, which are given below:

$$\lambda_1 = \sqrt{\frac{1}{2\bar{e}_1}(a - \bar{e}_2)}, \tag{5.2.2}$$

$$\lambda_2 = \sqrt{\frac{1}{2\bar{e}_1}(-a - \bar{e}_2)}, \tag{5.2.3}$$

$$\lambda_3 = \sqrt{\frac{1}{2\bar{e}_1}(a - \bar{e}_2)}, \tag{5.2.4}$$

$$\lambda_4 = \sqrt{\frac{1}{2\bar{e}_1}(-a - \bar{e}_2)}, \tag{5.2.5}$$

where $a = \sqrt{\bar{e}_2^2 - 4\bar{e}_3}$. It is possible (as is well known) that these roots are not unique and so we have to check that this is not the case. If all roots are unique we obtain the simple complementary solutions:

$$y_1 = e^{\lambda_1 x} \tag{5.2.6}$$

$$y_2 = e^{\lambda_2 x} \tag{5.2.7}$$

$$y_3 = e^{\lambda_3 x} \tag{5.2.8}$$

$$y_4 = e^{\lambda_3 x}. \tag{5.2.9}$$

If we have repeated roots we need to be a bit more careful. If for example we have $\lambda_1 = \lambda_2$ we need to change our solution to include a factor x, this means that (5.2.6 and 5.2.7) become

$$y_1 = e^{\lambda_1 x} \tag{5.2.10}$$

$$y_2 = xe^{\lambda_2 x}. \tag{5.2.11}$$

Once we have calculated solutions y_1 to y_4, making adjustments for repeated roots if necessary, we need to calculate the Wronskian

$$W = \begin{vmatrix} y_1 & y_2 & y_3 & y_4 \\ y_1' & y_2' & y_3' & y_4' \\ y_1'' & y_2'' & y_3'' & y_4'' \\ y_1''' & y_2''' & y_3''' & y_4''' \end{vmatrix}.$$

We also need to calculate variations of the Wronskian, which we label W_i with $i = 1$ to 4, where the i^{th} column is replaced by $(0, 0, 0, b(x))$. Once we have calculated these we calculate the coefficients $C_i(x)$ of y_i in the particular integral

$$y_p(x) = \sum_{i=1}^{4} C_i(x) y_i(x), \tag{5.2.12}$$

where

$$C_i(x) = \int \frac{W_i(x)}{W(x)} dx. \tag{5.2.13}$$

Then the general solution is

$$\eta(x) = y_{cf}(x) + y_p(x), \tag{5.2.14}$$

where the complementary solution is

$$y_{cf} = a_1 y_1(x) + a_2 y_2(x) + a_3 y_3(x) + a_4 y_4(x), \tag{5.2.15}$$

and the constants a_1 to a_4 need to be determined by the boundary conditions.

5.3 Large Blips

Now we consider particular forms of large blip. By large blips we mean here that the blip spans from the front stagnation point to the separation point on a bluff body such as a circular cylinder. In this case we consider the pressure $p(x)$ to be prescribed between these two points, say $x = 0$, 1, and we calculate the blip shape from the time-independent pressure-shape relation

$$p(x) - p_0 = \bar{e}_3 \eta + \bar{e}_2 \eta_{xx} + \bar{e}_1 \eta_{xxxx}, \tag{5.3.1}$$

with boundary conditions $\eta(x) = 0$ and $\eta'(x) = 0$ at $x = 0$ and $x = 1$. Preliminary calculations for the numerical method have been done for prescribed pressures of $p(x) = x$ and $p(x) = -x$ and $p_0 = 0$, giving the results in figs. 5.2 and 5.3.

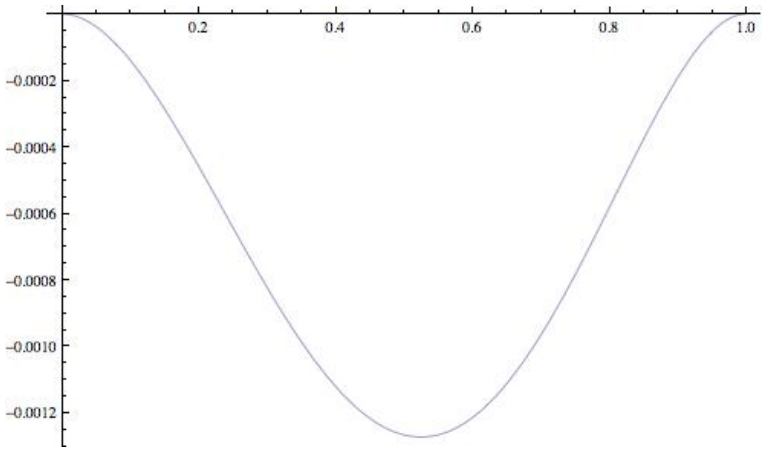

Figure 5.2: numerical results for surface shape η for $p(x) = x$ with $p_0 = 0$; all other coefficients in the pressure shape relation (5.2.1) equal unity

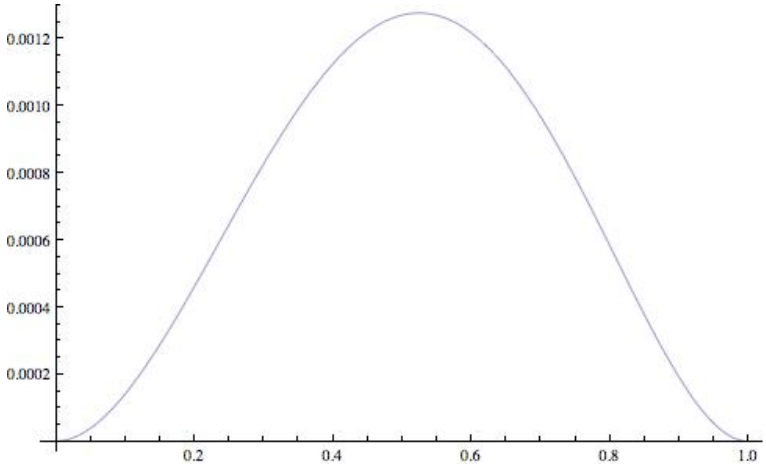

Figure 5.3: numerical results for surface shape for $p(x) = -x$ with $p_0 = 0$, all other coefficients in the pressure shape relation (5.6) are again unity

These results can be verified analytically based on the complementary functions of (5.2.1) which are exponential functions and on the particular integral which has $\eta = \frac{\pm x p_0}{b}$. The analytical results are plotted in figures 5.4 and 5.5.

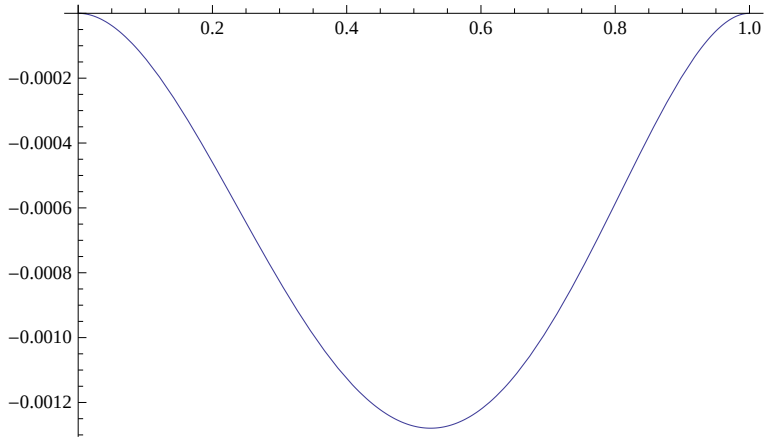

Figure 5.4: analytical results for the surface shape f for $p(x) = x$ with $p_0 = 0$; all other coefficients in the pressure shape relation (5.6) equal unity

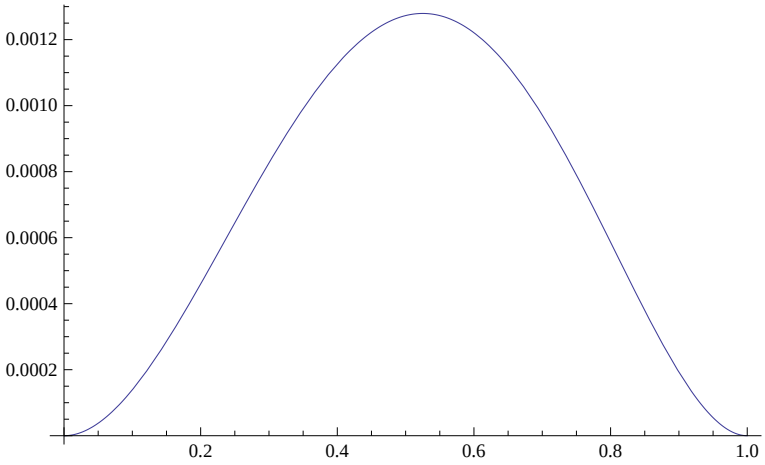

Figure 5.5: analytical results for the surface shape for $p(x) = -x$ with $p_0 = 0$, all other coefficients in the pressure shape relation (5.6) are again unity

As we can see from comparing figures 5.2-5.5 our numerical method appears to produce accurate results. So now we can move on to more realistic pressure distributions. If the shape of the blip produces a hump-like effect near the pressure minimum near $x = 1$ such an effect might influence the laminar separation via the triple deck process that occurs close to $x = 1$, see Smith [46]; this relates back to our remark at the start of the present chapter on affecting the global flow behaviour substantially. We consider the following pressure distribution

$$p(x) = \frac{1}{\bar{e}_1} exp(-4x^2) cos(5x) \tag{5.3.2}$$

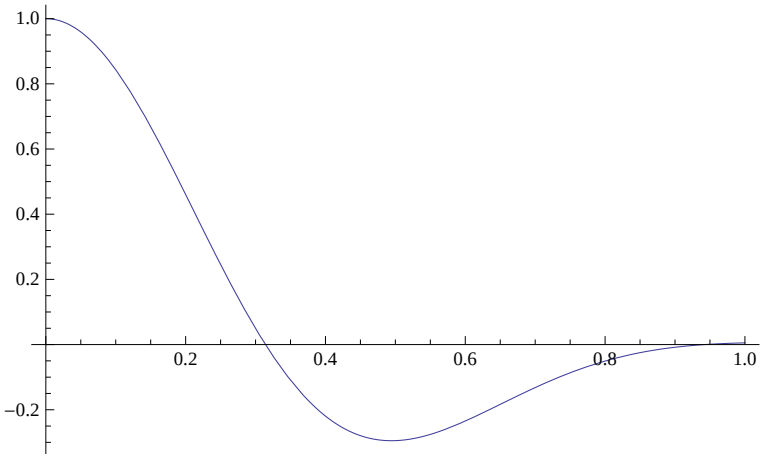

Figure 5.6: plot of the imposed pressure $p(x) = \frac{1}{\bar{e}_1} exp(-4x^2)cos(5x)$

and $p_0 = 0$: see figure 5.6. Now we consider varying each parameter separately. This is specifically varying $\bar{e}_1$ from -100 to 100 in steps of 20 while keeping the other two constant, with $\bar{e}_2 = 1$ and $\bar{e}_3 = -1$, then varying $\bar{e}_2$ from -100 to 100 in steps of 20 while keeping the other two constant, with $\bar{e}_1 = -1$ and $\bar{e}_3 = -1$, and finally varying $\bar{e}_3$ from -100 to 100 while keeping the other two constant, with $\bar{e}_4 = -1$ and $\bar{e}_2 = 1$. The signs of the constant parameters were chosen according to their signs in the real world applications of interest, since the latter have $\bar{e}_1 < 0$, $\bar{e}_2 > 0$ and $\bar{e}_3 < 0$. The results for varying $\bar{e}_1$ are given in figures 5.7-5.18.

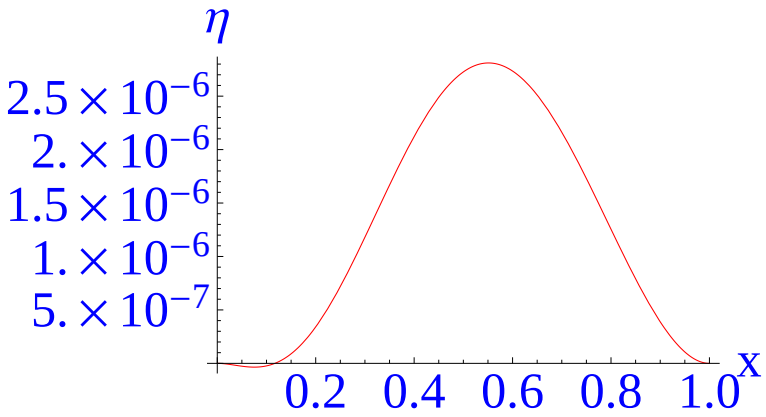

Figure 5.7: hump shape for: $\bar{e}_1$=-100; $\bar{e}_2$=1; $\bar{e}_3 = -1$

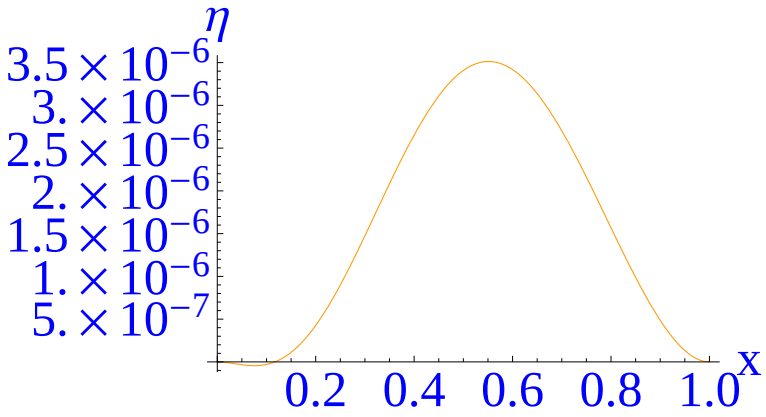

Figure 5.8: hump shape for: $\bar{e}_1$=-80; $\bar{e}_2$=1; $\bar{e}_3 = -1$

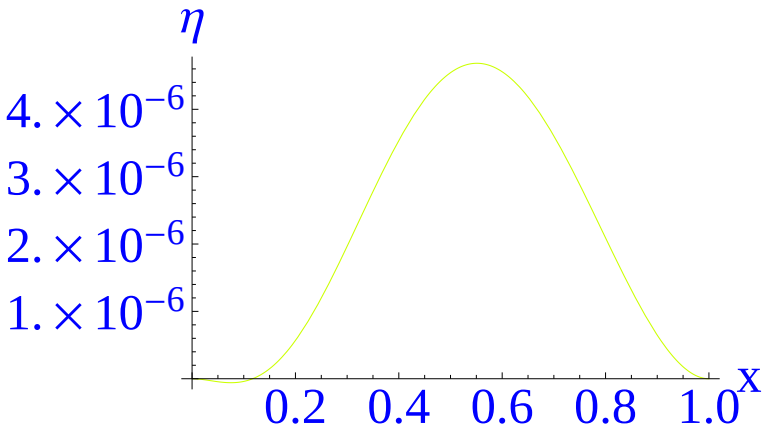

Figure 5.9: hump shape for: $\bar{e}_1$=-60; $\bar{e}_2$=1; $\bar{e}_3 = -1$

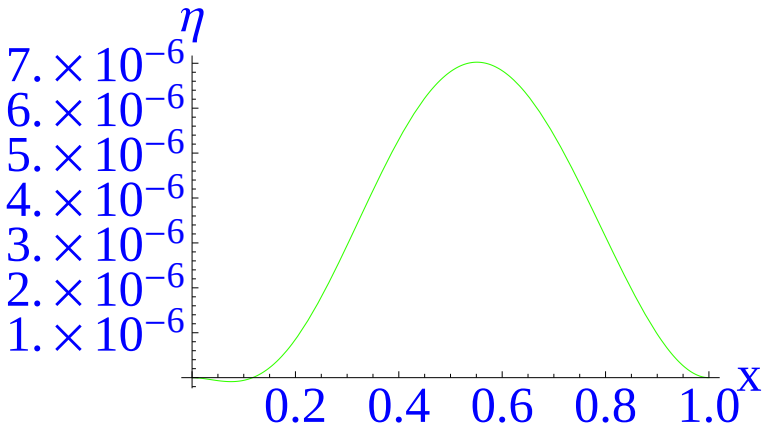

Figure 5.10: hump shape for: $\bar{e}_1$=-40; $\bar{e}_2$=1; $\bar{e}_3 = -1$

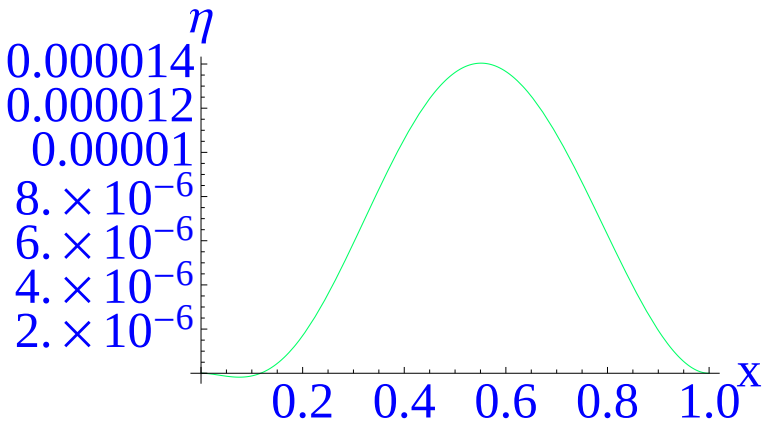

Figure 5.11: hump shape for: $\bar{e}_1$=-20; $\bar{e}_2$=1; $\bar{e}_3 = -1$

We can clearly see that as $\bar{e}_1$ increases from -100 to -20 the hump becomes larger.

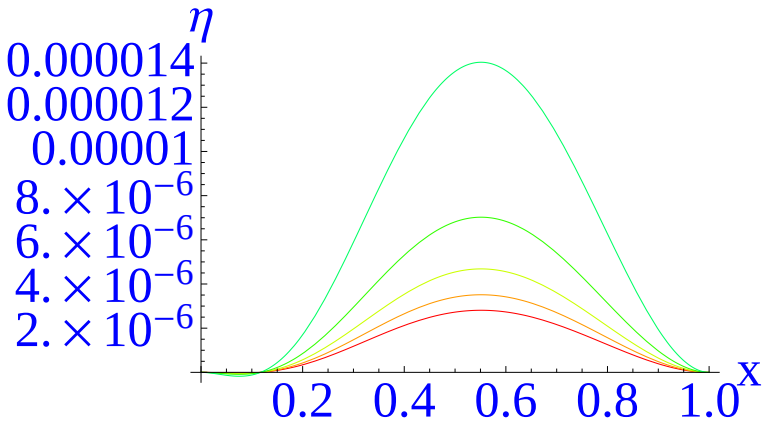

Figure 5.12: hump shape for: $\bar{e}_1$=-100 to -20 in steps of 20; $\bar{e}_2$=1; $\bar{e}_3 = -1$

In our flexible-wall equation $\bar{e}_1$ should be negative but for completeness we have done some calculations with $\bar{e}_1$ positive.

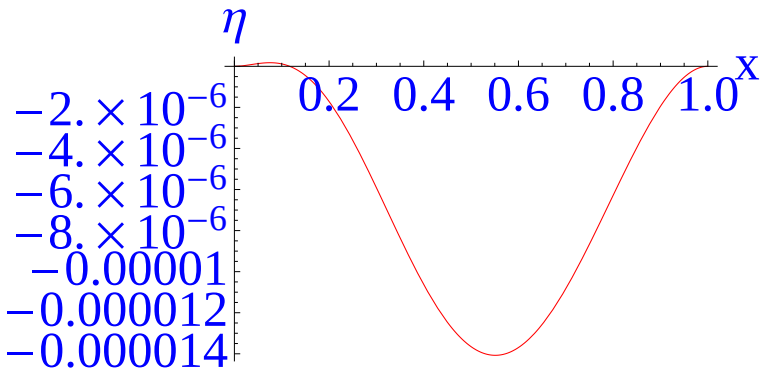

Figure 5.13: hump shape for: $\bar{e}_1$=20; $\bar{e}_2$=1; $\bar{e}_3 = -1$

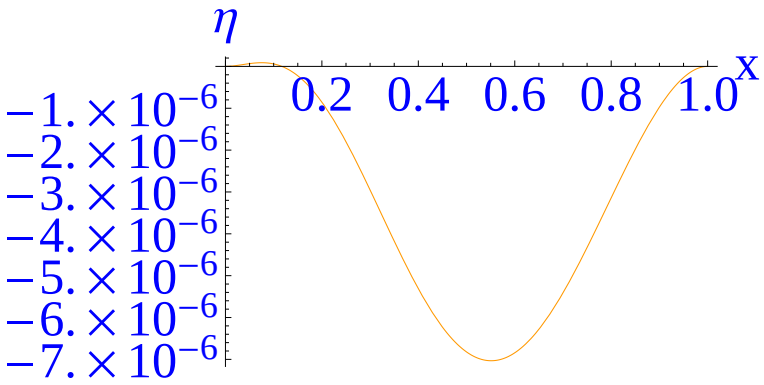

Figure 5.14: hump shape for: $\bar{e}_1$=40; $\bar{e}_2$=1; $\bar{e}_3 = -1$

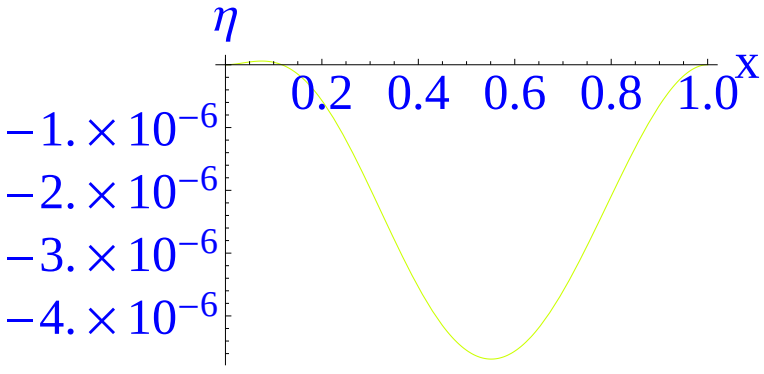

Figure 5.15: hump shape for: $\bar{e}_1$=60; $\bar{e}_2$=1; $\bar{e}_3 = -1$

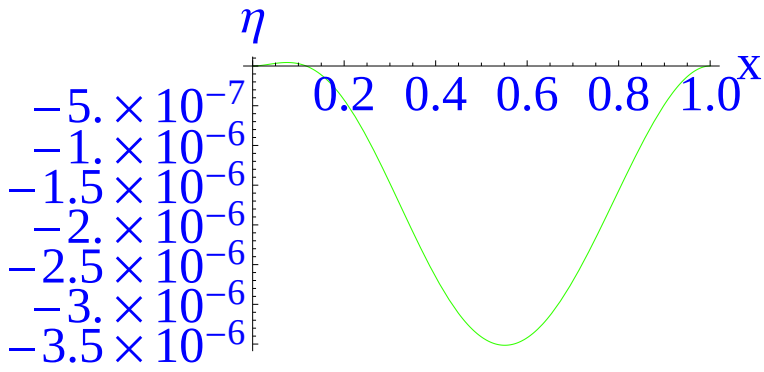

Figure 5.16: hump shape for: $\bar{e}_1$=80; $\bar{e}_2$=1; $\bar{e}_3 = -1$

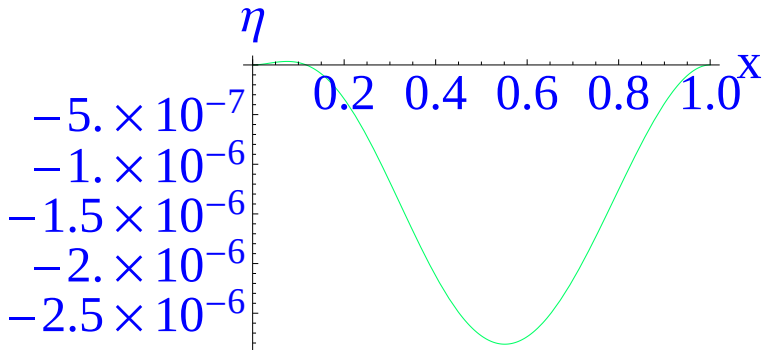

Figure 5.17: hump shape for: $\bar{e}_1$=100; $\bar{e}_2$=1; $\bar{e}_3 = -1$

We can clearly see that as e_1 increases from 20 to 100 the dent becomes smaller.

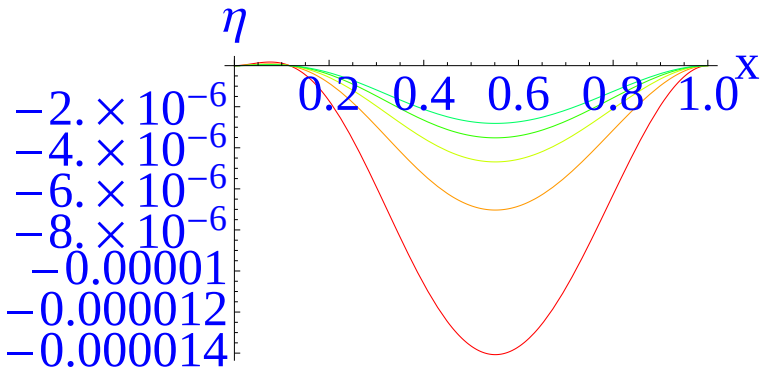

Figure 5.18: hump shape for: $\bar{e}_1$=20 to 100 in steps of 20; $\bar{e}_2$=1; $\bar{e}_3 = -1$

The results for varying $\bar{e}_2$ are given below in figures 5.19-5.31.

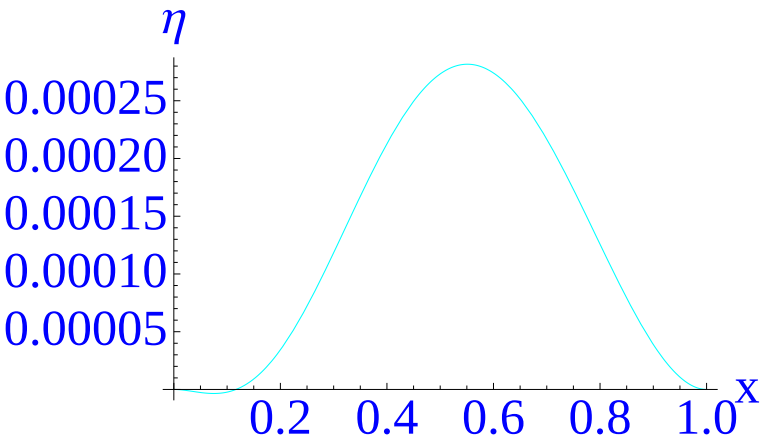

Figure 5.19: hump shape for: $\bar{e}_1$=-1; $\bar{e}_2$=0; $\bar{e}_3 = -1$

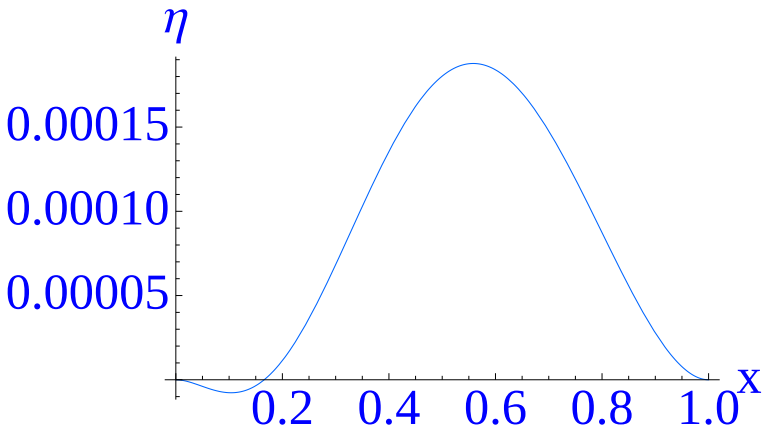

Figure 5.20: hump shape for: $\bar{e}_1$=-1; $\bar{e}_2$=20; $\bar{e}_3 = -1$

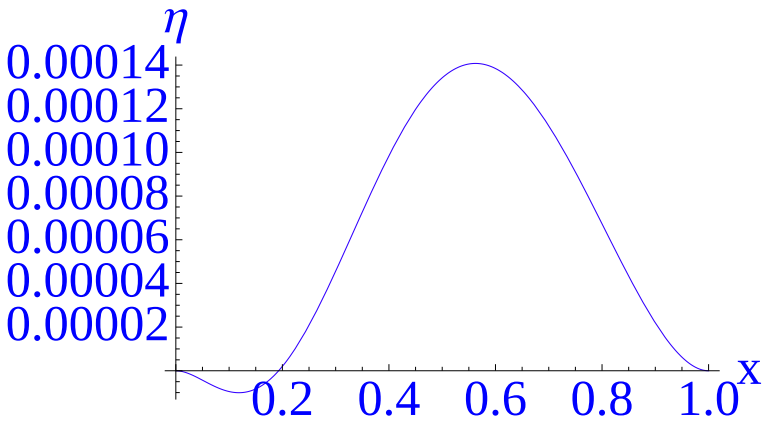

Figure 5.21: hump shape for: $\bar{e}_1$=-1; $\bar{e}_2$=40; $\bar{e}_3 = -1$

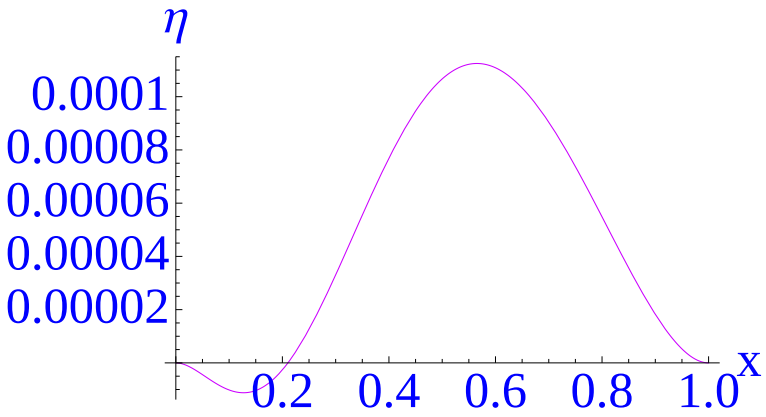

Figure 5.22: hump shape for: $\bar{e}_1$=-1; $\bar{e}_2$=60; $\bar{e}_3 = -1$

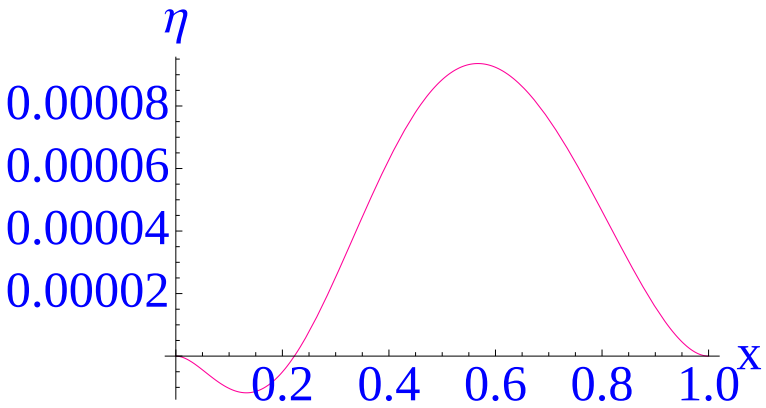

Figure 5.23: hump shape for: $\bar{e}_1$=-1; $\bar{e}_2$=80; $\bar{e}_3 = -1$

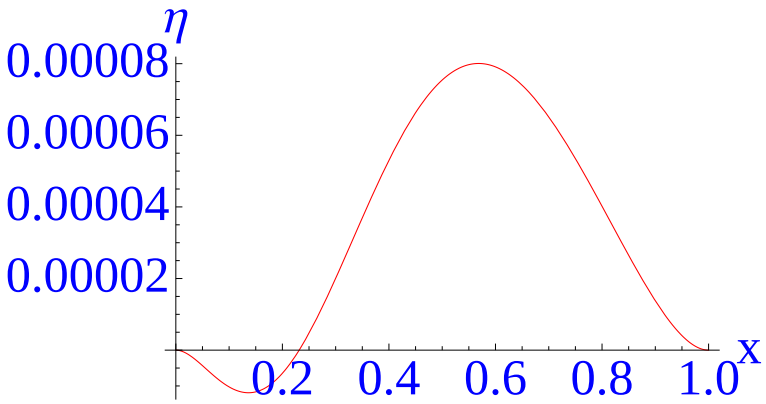

Figure 5.24: hump shape for: $\bar{e}_1$=-1; $\bar{e}_2$=100; $\bar{e}_3 = -1$

We can clearly see that as we increase $e2$ from 0 to 100 the height of the hump decreases.

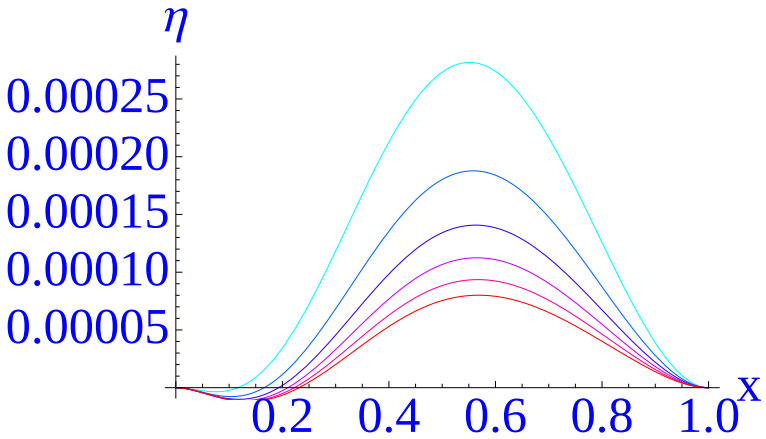

Figure 5.25: hump shape for: $\bar{e}_1$=-1; $\bar{e}_2$=0 to 100 in steps of 20; $\bar{e}_3 = -1$

Again, in our flexible-wall equation $\bar{e}_2$ should be positive but for completeness we have performed some calculations with $\bar{e}_2$ negative.

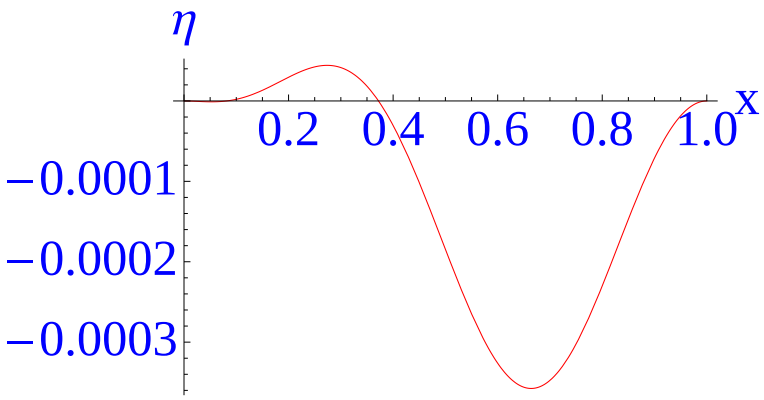

Figure 5.26: hump shape for: $\bar{e}_1$=-1; $\bar{e}_2$=-100; $\bar{e}_3 = -1$

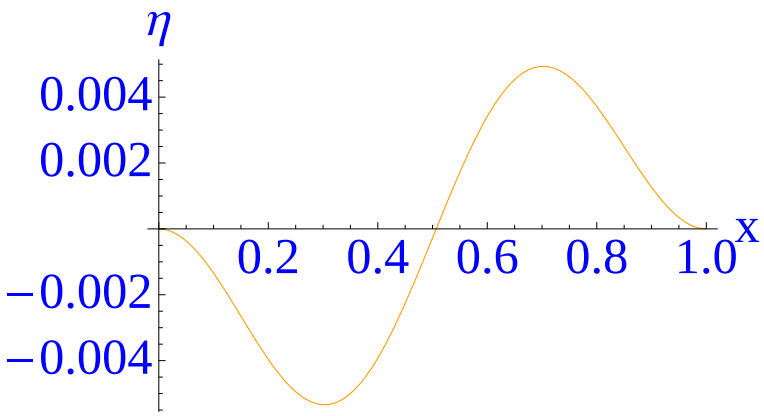

Figure 5.27: hump shape for: $\bar{e}_1$=-1; $\bar{e}_2$=-80; $\bar{e}_3 = -1$

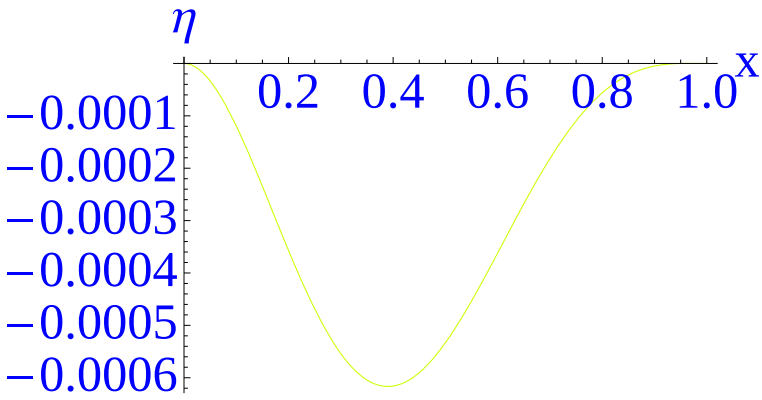

Figure 5.28: hump shape for: $\bar{e}_1$=-1; $\bar{e}_2$=-60; $\bar{e}_3 = -1$

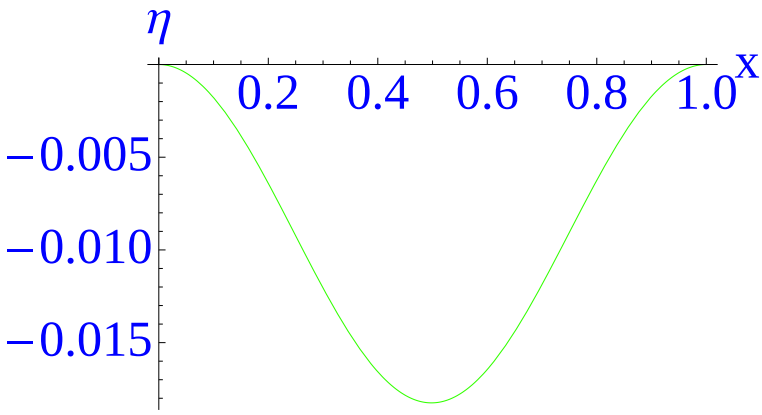

Figure 5.29: hump shape for: $\bar{e}_1$=-1; $\bar{e}_2$=-40; $\bar{e}_3 = -1$

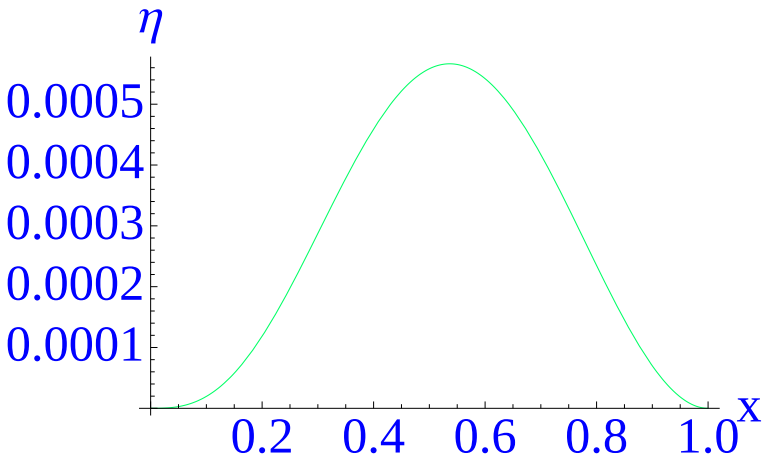

Figure 5.30: hump shape for: $\bar{e}_1$=-1; $\bar{e}_2$=-20; $\bar{e}_3 = -1$

The results for $\bar{e}_2$ negative vary quantitatively. However we should note that e_2 is positive in our wall-relation.

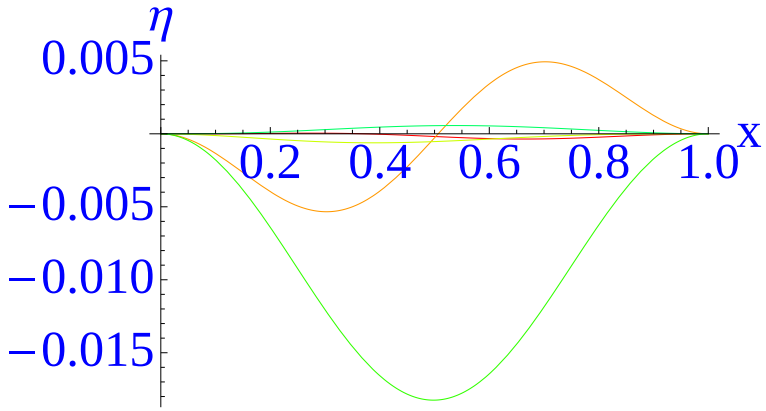

Figure 5.31: hump shape for: $\bar{e}_1$=-1; $\bar{e}_2$=0 to 100 in steps of 20; $\bar{e}_3 = -1$

The results for varying $\bar{e}_3$ are given below in figures 5.32-5.44.

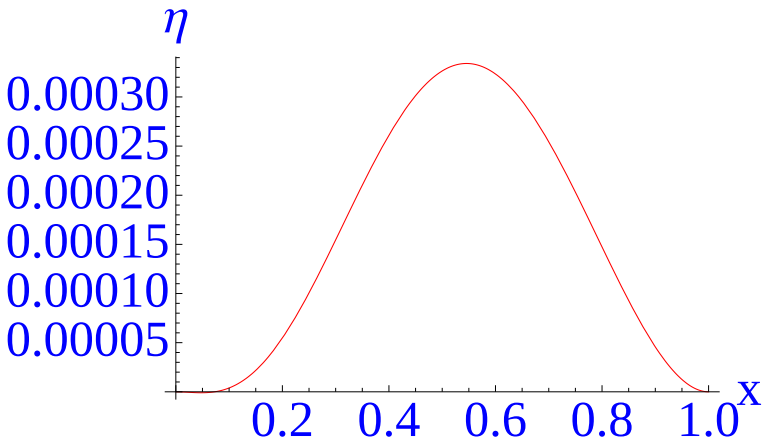

Figure 5.32: hump shape for: $\bar{e}_1$=-1; $\bar{e}_2$=1; $\bar{e}_3 = -100$

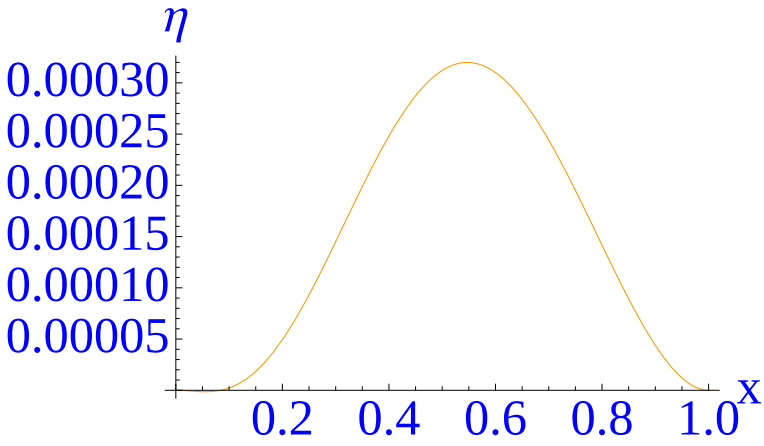

Figure 5.33: hump shape for: $\bar{e}_1$=-1; $\bar{e}_2$=1; $\bar{e}_3 = -80$

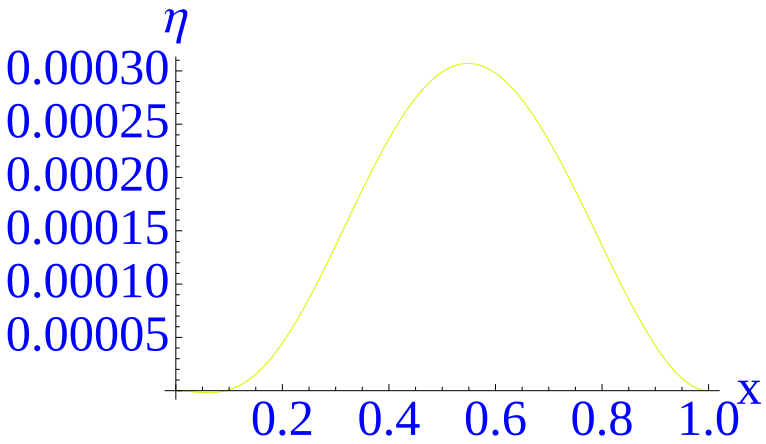

Figure 5.34: hump shape for: $\bar{e}_1$=-1; $\bar{e}_2$=1; $\bar{e}_3 = -60$

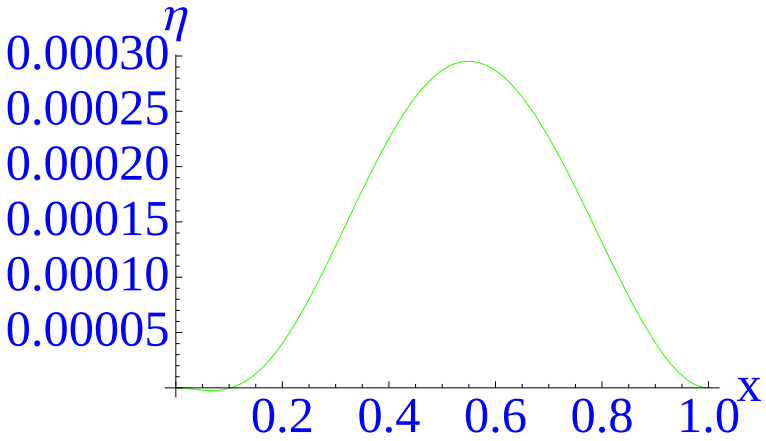

Figure 5.35: hump shape for: $\bar{e}_1$=-1; $\bar{e}_2$=1; $\bar{e}_3 = -40$

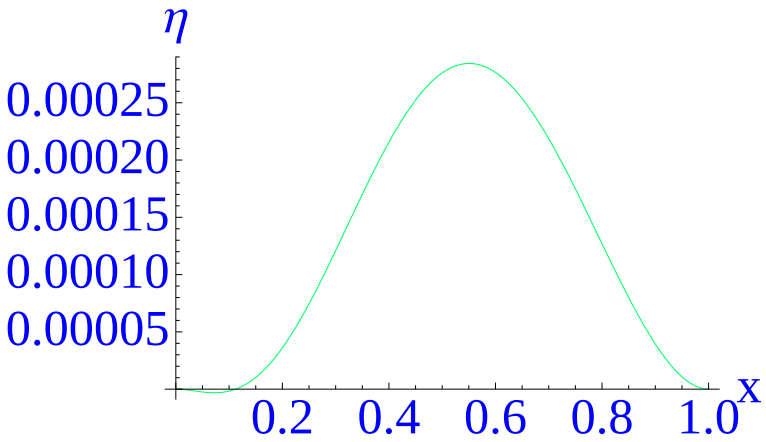

Figure 5.36: hump shape for: $\bar{e}_1$=-1; $\bar{e}_2$=1; $\bar{e}_3 = -20$

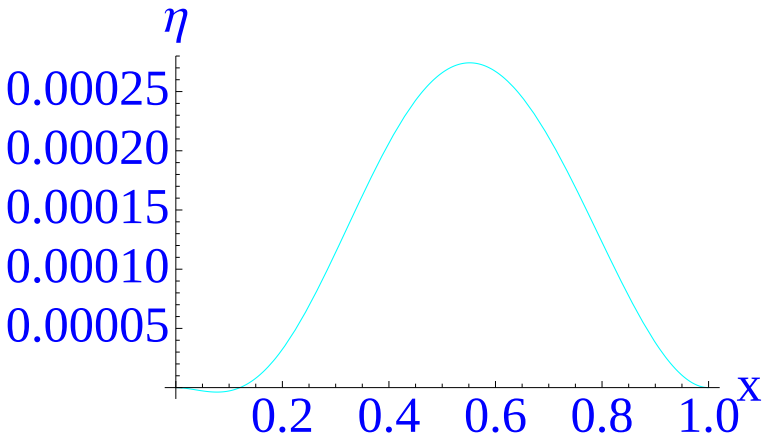

Figure 5.37: hump shape for: $\bar{e}_1$=-1; $\bar{e}_2$=1; $\bar{e}_3 = 0$

We can clearly see that as we increase $\bar{e}_3$ from -100 to 0 the height of the hump decreases.

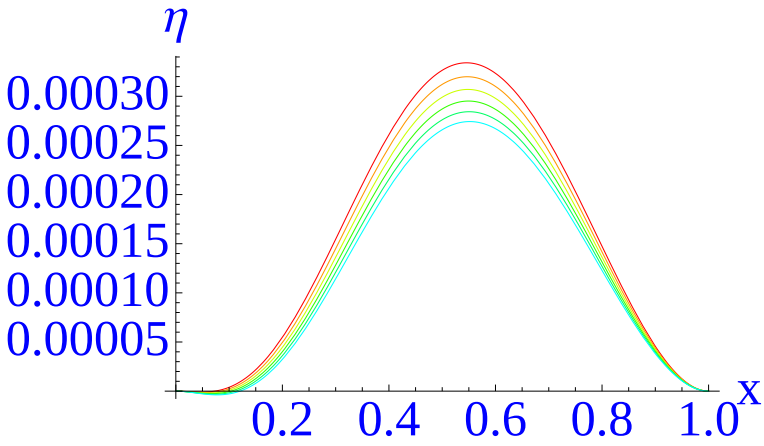

Figure 5.38: hump shape for: $\bar{e}_1$=-1; $\bar{e}_2$=1; $\bar{e}_3 = -100$ to 0 in steps of 20

Once more, in our flexible-wall equation $\bar{e}_3$ should be negative but for completeness we have done some calculations with $\bar{e}_3$ positive.

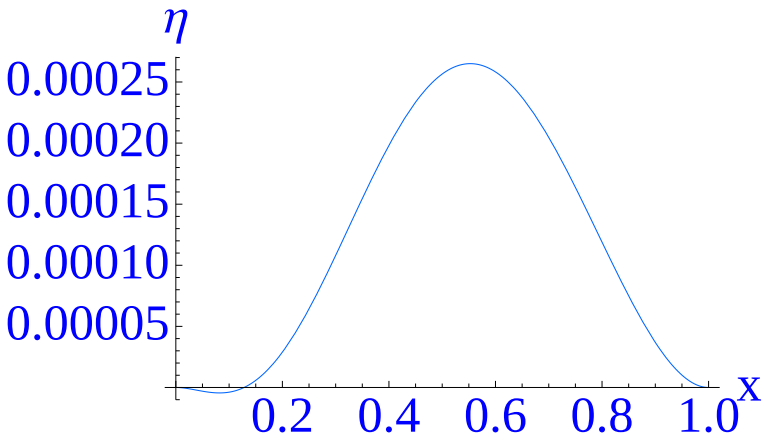

Figure 5.39: hump shape for: $\bar{e}_1$=-1; $\bar{e}_2$=1; $\bar{e}_3 = 20$

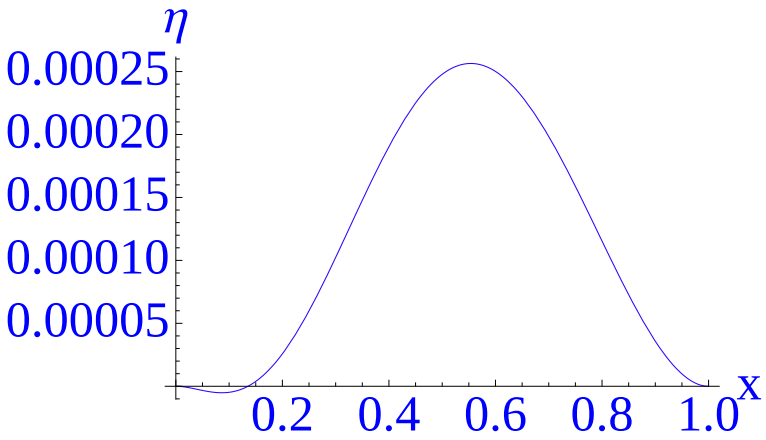

Figure 5.40: hump shape for: $\bar{e}_1$=-1; $\bar{e}_2$=1; $\bar{e}_3 = 40$

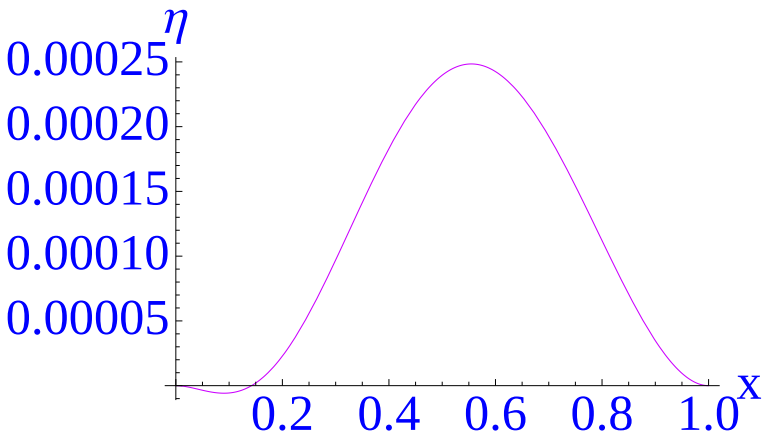

Figure 5.41: hump shape for: $\bar{e}_1$=-1; $\bar{e}_2$=1; $\bar{e}_3 = 60$

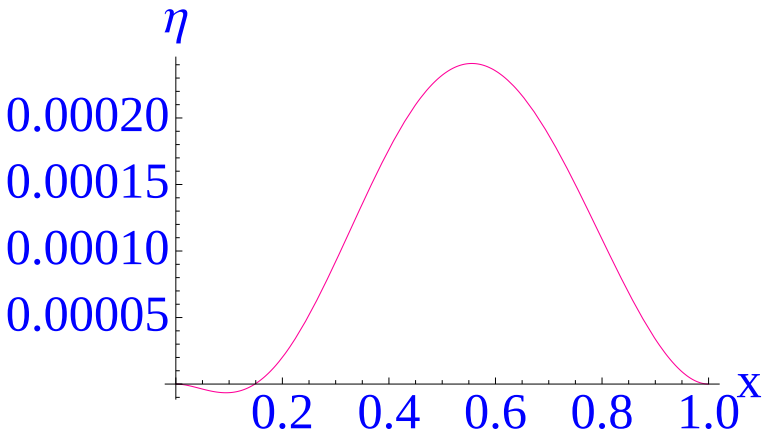

Figure 5.42: hump shape for: $\bar{e}_1$=-1; $\bar{e}_2$=1; $\bar{e}_3$ = 80

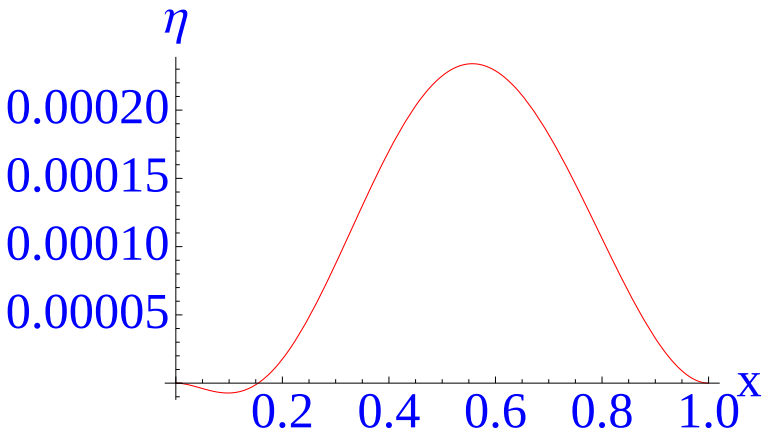

Figure 5.43: hump shape for: $\bar{e}_1$=-1; $\bar{e}_2$=1; $\bar{e}_3$ = 100

The results for e_3 positive continue in the same trend as for e_3 negative.

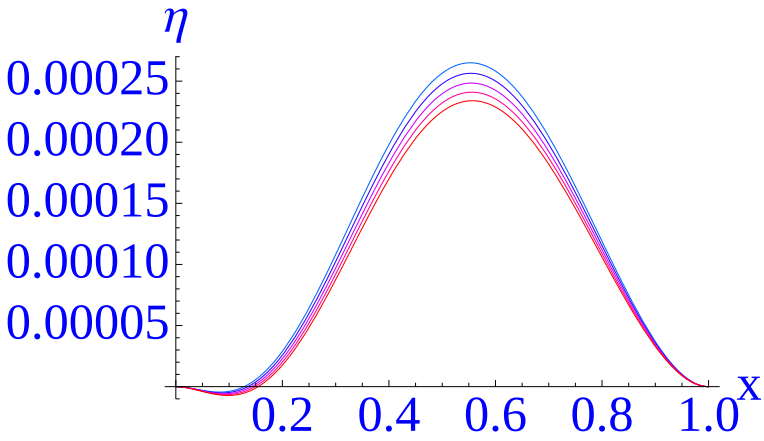

Figure 5.44: hump shape for: $\bar{e}_1$=-1; $\bar{e}_2$=1; $\bar{e}_3$=20 to 100 in steps of 20

Next we consider another pressure distribution, which is more realistic for the flow over a circular cylinder. The distribution is given by

$$p(x) = (1 - ax^2)(1 - x^2)^{\frac{1}{2}}, \tag{5.3.3}$$

where $a > 1$. The analytical method used above does not work for this distribution, therefore we consider a simplified pressure-wall relation by dropping the terms containing e_1 and e_3, i.e.

$$e_2\eta''(x) = p(x) - p_0 \tag{5.3.4}$$

or with $p(x)$ substituted by (5.3.3)

$$e_2\eta''(x) = (1 - ax^2)(1 - x^2)^{\frac{1}{2}} - p_0. \tag{5.3.5}$$

Integrating twice we obtain the following expressions for $\eta(x)$

$$\eta(x) = \frac{1}{e_2}(\frac{1}{6}(\sqrt{\frac{1}{x^2} - 1} + 2\sqrt{1 - x^2} - 2) + \frac{a}{120}(\sqrt{\frac{1}{x^2} - 1}x^3(7 - 6x^2) - 16(\sqrt{1 - x^2} - 1))$$

$$-15(a-4)xArcSin(x) - \frac{1}{2}p_0x^2) + cx + b \tag{5.3.6}$$

where constants c and b need to be determined from the boundary conditions $\eta(0) = \eta(1) = 0$. We can immediately see that b must equal zero and we find $c = \frac{80-32a+120p_0-60\pi+15a\pi}{240e_2}$. We plot the above for several values of e_2, p_0 and a in figures 5.45 -5.52 below.

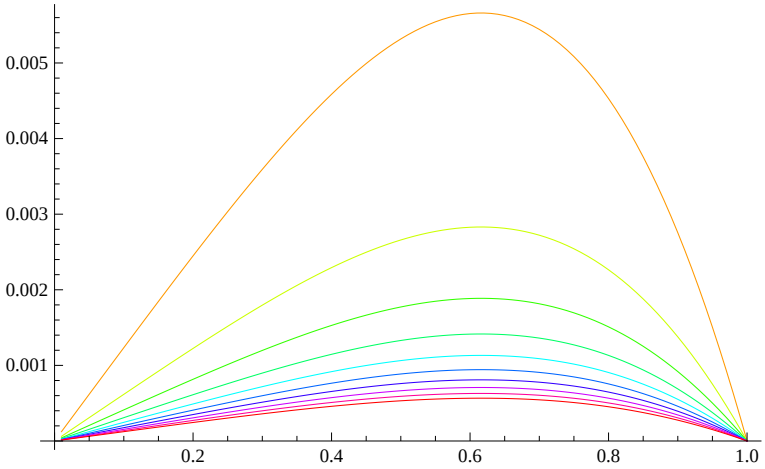

Figure 5.45: $\eta(x)$ for: $\bar{e}_2 = 10$ to $\bar{e}_2 = 100$ in steps of 10; $p_0 = 1$ $a = 1.2$

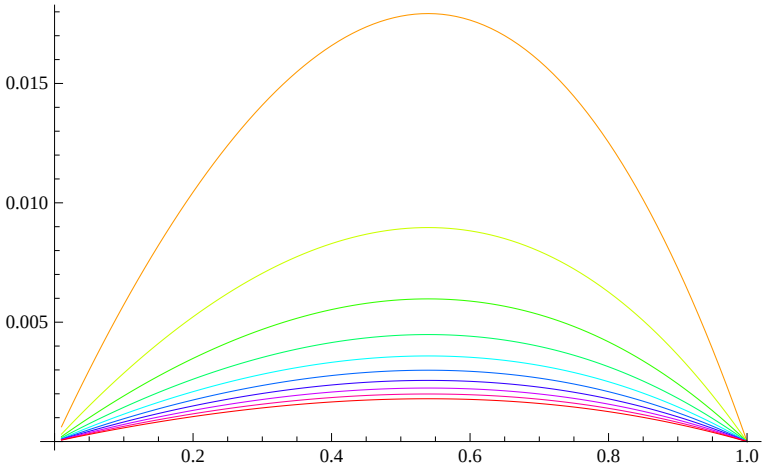

Figure 5.46: $\eta(x)$ for: $\bar{e}_2 = 10$ to $\bar{e}_2 = 100$ in steps of 10; $p_0 = 2$ $a = 1.2$

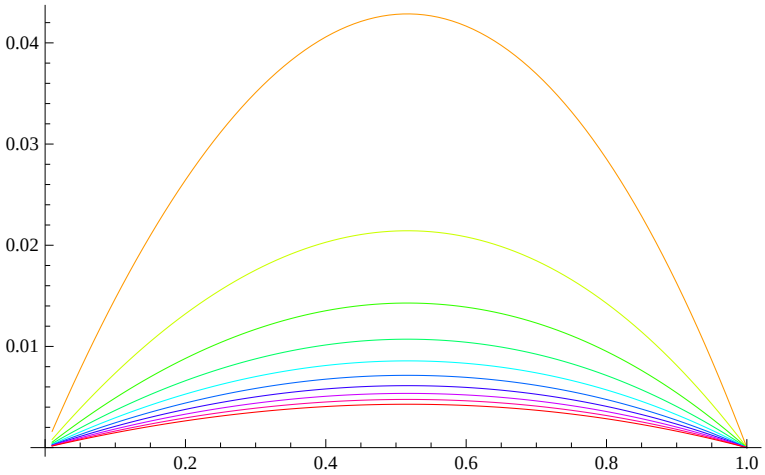

Figure 5.47: $\eta(x)$ for: $\bar{e}_2 = 10$ to $\bar{e}_2 = 100$ in steps of 10; $p_0 = 4$ $a = 1.2$

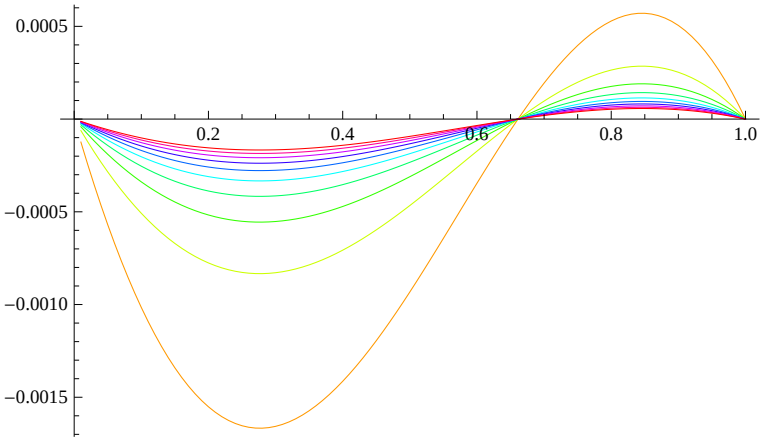

Figure 5.48: $\eta(x)$ for: $\bar{e}_2 = 10$ to $\bar{e}_2 = 100$ in steps of 10; $p_0 = .5$ $a = 1.2$

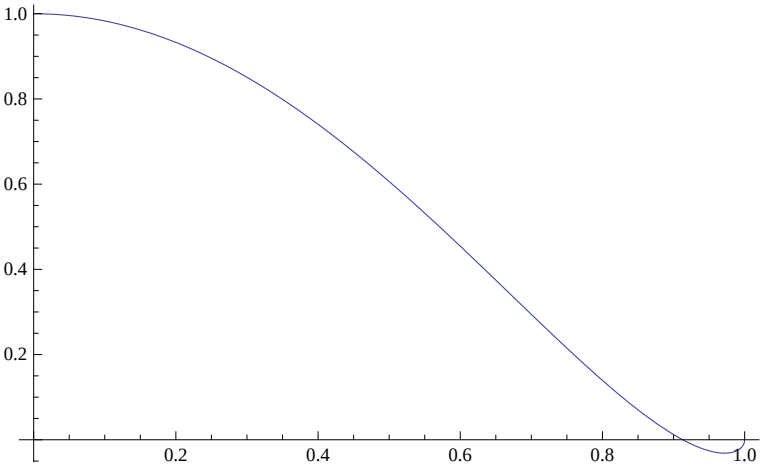

Figure 5.49: pressure plot for $p_0 = .5$ $a = 1.2$

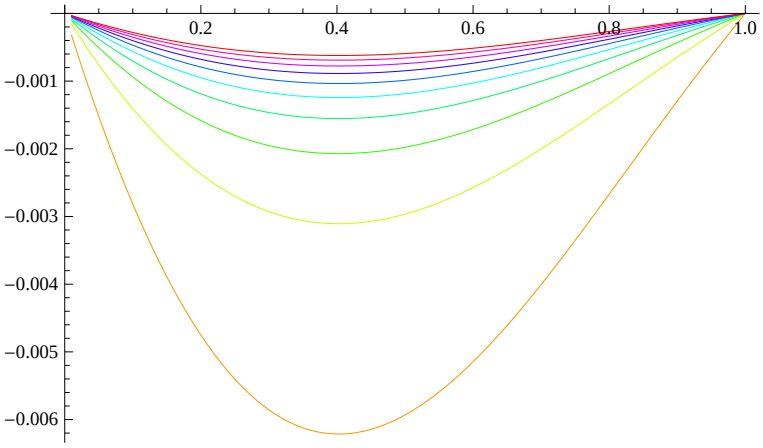

Figure 5.50: $\eta(x)$ for: $\bar{e}_2 = 10$ to $\bar{e}_2 = 100$ in steps of 10; $p_0 = .1$ $a = 1.2$

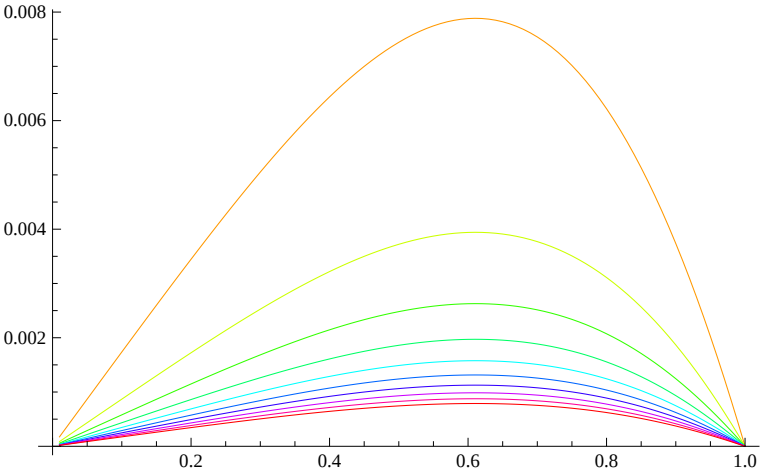

Figure 5.51: $\eta(x)$ for: $\bar{e}_2 = 10$ to $\bar{e}_2 = 100$ in steps of 10; $p_0 = 1$ $a = 2$

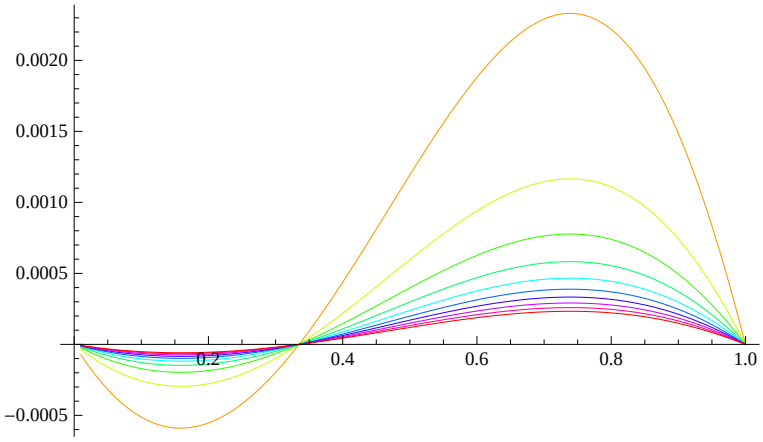

Figure 5.52: $\eta(x)$ for: $\bar{e}_2 = 10$ to $\bar{e}_2 = 100$ in steps of 10; $p_0 = .5$ $a = 2$

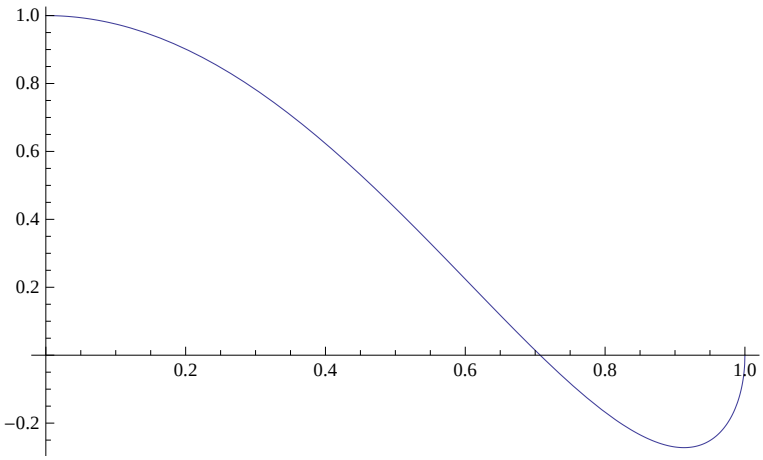

Figure 5.53: pressure plot for $p_0 = .5$ $a = 2$

In each case the orange line corresponds to $\eta(x)$ with $e_2 = 10$ increasing to the red line $\eta(x)$ with $e_2 = 100$. So the effect of increasing e_2 only affects the height of the blip, the smaller e_2 the larger the blip height or dip in some cases. A more qualitative change in the blip shape comes from varying the parameters a and p_0. For smaller values of p_0 the blip starts to become a dip. For some combinations of p_0 and a the maximum in blip height seems to be near the minimum in pressure.

So there is potential for the breakaway separation from a bluff body described by the triple-deck structure. However more work needs to be done to determine exactly for which combinations of a and p_0 this will happen.

Chapter 6

Short Blips and Resonance

In this chapter are are considering a sub-layer of the boundary layer as indicated in figure 6.1 below, and within it the blips are small compared to the ones from previous chapters. We focus mainly on a computational and analytical investigation of the influence of the parameter "a" in the linear case and "b" in the nonlinear case, which measure the ratio of the flow strength to flexibility strength. We find that increasing these parameters leads to resonance.

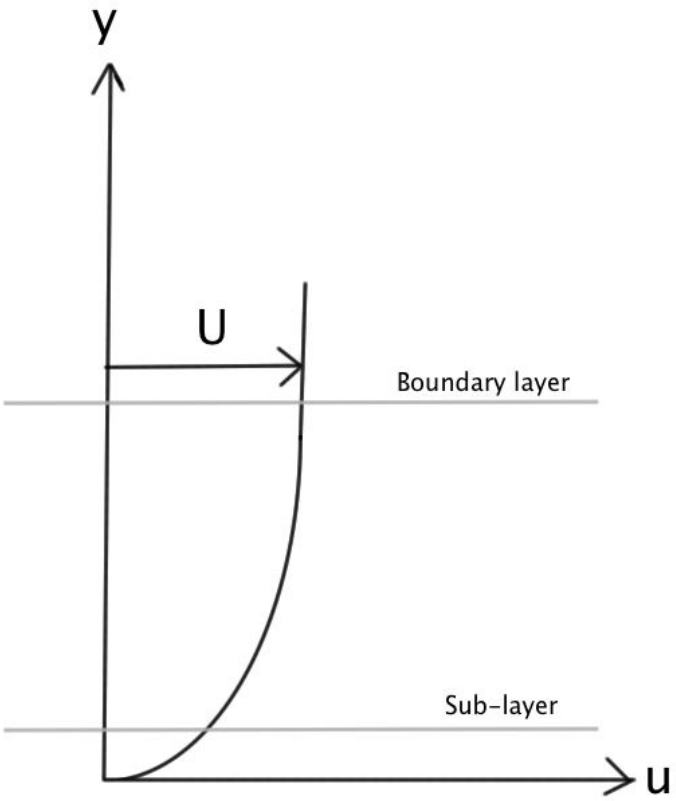

Figure 6.1: Schematic of the sub-layer

6.1 Linear behaviour

Here we solve the time-independent wall-relation (2..4.14) together with the linear boundary layer equations. Below we will derive the set of equations that we will use to solve for this model.

6.1.1 Equations for the linear model

So our set of equations is the relation between p and η at the wall

$$p - p_0 = e_1\eta_{xxxx} + e_2\eta_{xx} + e_3\eta, \tag{6.1.1}$$

and the linear boundary layer equations

$$u_x + v_y = 0 \qquad \text{continuity}, \tag{6.1.2}$$

$$yu_x + v = -p_x + u_{yy} \qquad \text{momentum}, \tag{6.1.3}$$

where we have assumed a basic flow of $U = y$. We have no-slip boundary conditions at $y = 0$, $u = v = 0$ and the wall displacement effect $u \to \eta$ as $y \to \infty$. We can derive a new relation between p and η from the boundary layer equations analytically as follows. Differentiate (6.1.3) with respect to the vertical coordinate y and use (6.1.2) to eliminate v_y and substitute $\tau = u_y$:

$$y\tau_x = \tau_{yy}. \tag{6.1.4}$$

Next we apply a Fourier transform to (6.1.4) which results in

$$yik\tau^* = \tau^*{}_{yy}. \tag{6.1.5}$$

where we have assumed that $\tau \to 0$ as $x \to \pm\infty$. Now, if we change variable to $\zeta = (ik)^{\frac{1}{3}}y$ we obtain Airy's equation for τ^*

$$\zeta\tau^* - \tau^*{}_{\zeta\zeta} = 0 \tag{6.1.6}$$

This has the known solution

$$\tau^*(k) = B^*(k)Ai(\zeta) \tag{6.1.7}$$

where we have discarded the $Bi(\zeta)$ solution because we need to have boundedness at infinity. The boundary conditions are used to eliminate $B^*(k)$. Using (6.1.3) at $y = 0$ we obtain

$$ikp^*(k) = B^*(k)(ik)^{\frac{1}{3}} Ai'(0) \tag{6.1.8}$$

and for $y \to \infty$ we make use of $u^*(k) = \int_0^\infty \tau^*(y)dy = \eta^*$ since $\tau = u_y$ to obtain

$$(ik)^{-\frac{1}{3}} \int_0^\infty B^*(k)Ai(\zeta)d\zeta = \eta^* \tag{6.1.9}$$

or

$$(ik)^{-\frac{1}{3}} B^*(k)\kappa = \eta^* \tag{6.1.10}$$

where $\kappa = \int_0^\infty Ai(\zeta)d\zeta (= \frac{1}{3})$. So we have

$$B^*(k) = \frac{(ik)^{\frac{1}{3}}}{\kappa}\eta^*. \tag{6.1.11}$$

Substituting the above into (6.1.8) gives

$$ikp^* = \frac{(ik)^{\frac{2}{3}}}{\kappa} Ai'(0)\eta^* \tag{6.1.12}$$

or

$$p^* = \frac{Ai'(0)}{\kappa} G^*(k)\eta^* \tag{6.1.13}$$

where $G^*(k) = (ik)^{-\frac{1}{3}}$. Now we apply the inverse Fourier transform to (6.1.13) to get

$$p = \frac{Ai'(0)}{\kappa} \frac{1}{\sqrt{2\pi}} \int_{-\infty}^{\infty} G^*(k)\eta^*(k)e^{ikx}dk \tag{6.1.14}$$

and making use of the convolution theorem we get

$$p = \frac{Ai'(0)}{\kappa} \frac{1}{\sqrt{2\pi}} \int_{-\infty}^{\infty} \eta(s) G(x-s) ds. \tag{6.1.15}$$

We need to calculate $G(x)$, in order to do this we apply the inverse Fourier transform to $G^*(k) = (ik)^{-\frac{1}{3}}$.

$$G(x) = \frac{1}{\sqrt{2\pi}} \int_{-\infty}^{\infty} G^*(k) e^{ikx} dk \tag{6.1.16}$$

or

$$G(x) = \frac{1}{\sqrt{2\pi}} \int_{-\infty}^{\infty} (ik)^{-\frac{1}{3}} e^{ikx} dk \tag{6.1.17}$$

and integrating we obtain

$$G(x) = \frac{\sqrt{2\pi}}{\Gamma(\frac{1}{3})} x^{-\frac{2}{3}} \qquad \text{for } x > 0. \tag{6.1.18}$$

Finally, substituting (6.1.18) into (6.1.15) we obtain the parabolic result

$$p = \frac{Ai'(0)}{\Gamma(\frac{1}{3})\kappa} \int_{-\infty}^{x} \eta(s)(x-s)^{-\frac{2}{3}} ds. \tag{6.1.19}$$

However, when we implement the above equation into our Mathematica code the negative exponent in the integral causes some difficulties. There is an alternative way of solving (6.1.19), which is to apply a Laplace transform to it in combination with (6.1.1). This approach is described in section 7.1 in detail. Here, to get around the implementation difficulty we can manipulate the equation by integrating by parts. Also it should be noted that $\eta \equiv 0$ for $x < 0$,

$$\int_0^x \eta(s)(x-s)^{-\frac{2}{3}} ds = [-3\eta(s)(x-s)^{\frac{1}{3}}]_{s=0}^{s=x} + 3\int_0^x \eta'(s)(x-s)^{\frac{1}{3}} ds, \tag{6.1.20}$$

but we know from our boundary conditions that $\eta(s=0)=0$ and also $(x-s)^{\frac{1}{3}}=0$ at $s=x$, so the first term on the right hand side in the above equation is identically zero.

This leaves us with a set of two equations and two unknowns to solve for in the linear case, namely

$$p - p_0 = e_1\eta_{xxxx} + e_2\eta_{xx} + e_3\eta \tag{6.1.21}$$

which is only valid inside the blip and

$$p = \frac{3Ai'(0)}{\Gamma(\frac{1}{3})\kappa}\int_0^x \eta'(s)(x-s)^{\frac{1}{3}}ds \tag{6.1.22}$$

which is valid everywhere.

6.1.2 Computational methods for the linear model

To solve (6.1.21) numerically we implement a second order centred finite differencing scheme as follows. We define two quantities A_j to represent the second derivative of η and B_j to represent the fourth derivative of η

$$A_j = \frac{\eta_{j+1} - 2\eta_j + \eta_{j-1}}{(\delta x)^2} \tag{6.1.23}$$

and

$$B_j = \frac{A_{j+1} - 2A_j + A_{j-1}}{(\delta x)^2}. \tag{6.1.24}$$

The latter can also be expressed in terms of η_j , since we can write A_{j+1} and A_{j-1} as follows

$$A_{j+1} = \frac{\eta_{j+2} - 2\eta_{j+1} + \eta_j}{(\delta x)^2} \tag{6.1.25}$$

and

$$A_{j-1} = \frac{\eta_j - 2\eta_{j-1} + \eta_{j-2}}{(\delta x)^2}. \tag{6.1.26}$$

Substituting this into (6.1.24) we have

$$B_j = \frac{1}{(\delta x)^4}(\eta_{j+2} - 4\eta_{j+1} + 6\eta_j - 4\eta_{j-1} + \eta_{j-2}) \tag{6.1.27}$$

Hence we can rewrite our differential equation (6.1.21) in terms of finite differences and group terms of η_j

$$\frac{e_1}{(\delta x)^4}\eta_{j+2}+(\frac{e_2}{(\delta x)^2}-\frac{4e_1}{(\delta x)^4})\eta_{j+1}+(\frac{6e_1}{(\delta x)^4}-\frac{2e_2}{(\delta x)^2}+e_3)\eta_j+(\frac{e_2}{(\delta x)^2}-\frac{4e_1}{(\delta x)^4})\eta_{j-1}+\frac{e_1}{(\delta x)^4}\eta_{j-2} = p_i-p_0 \tag{6.1.28}$$

From this we can define six quantities a_i, b_i, c_i, d_i, e_i and f_i. We need to be cautious not to confuse the quantity we call e_i with our parameters e_1, e_2 and e_3.

$$a_i = \frac{e_1}{(\delta x)^4} \tag{6.1.29}$$

$$b_i = \frac{e_2}{(\delta x)^2} - \frac{4e_1}{(\delta x)^4} \tag{6.1.30}$$

$$c_i = \frac{6e_1}{(\delta x)^4} - \frac{2e_2}{(\delta x)^2} + e_3 \tag{6.1.31}$$

$$d_i = \frac{e_2}{(\delta x)^2} - \frac{4e_1}{(\delta x)^4} \tag{6.1.32}$$

$$e_i = \frac{e_1}{(\delta x)^4} \tag{6.1.33}$$

$$f_i = p_i - p_0 \tag{6.1.34}$$

This allows us to write the finite difference equations in matrix form

$$\mathbf{M}.\underline{\eta} = \underline{f} \tag{6.1.35}$$

where

$$M = \begin{pmatrix} c_1 & d_1 & e_1 & 0 & 0 & 0 & ... & 0 & 0 \\ b_2 & c_2 & d_2 & e_2 & 0 & 0 & ... & 0 & 0 \\ a_3 & b_3 & c_3 & d_3 & e_3 & 0 & ... & 0 & 0 \\ 0 & & & & ... & & & & 0 \\ 0 & & & & ... & & & & 0 \\ 0 & & & & ... & & & & 0 \\ 0 & 0 & 0 & ... & a_{n-2} & b_{n-2} & c_{n-2} & d_{n-2} & e_{n-2} \\ 0 & 0 & 0 & ... & 0 & a_{n-1} & b_{n-1} & c_{n-1} & d_{n-1} \\ 0 & 0 & 0 & ... & 0 & 0 & a_n & b_n & c_n \end{pmatrix},$$

which we can solve by applying the Thomas algorithm. The algorithm works by eliminating the off-diagonals until the matrix is purely diagonal and which will then be trivial to solve. In our case we have a pentadiagonal matrix. First we eliminate the diagonal containing entries a_i and then the one containing b_i; here we start at the top and work our way to the bottom. For the remaining two, where we start eliminating the diagonal containing entries e_i and then the one containing d_i, we start at the bottom and work our way to the top. In order to remove the entries containing a_i multiply the $(i-1)^{\text{th}}$ row by $\frac{a_i}{b_{i-1}}$ and subtract the result from the i^{th} row as follows

$$\dot{a}_i = a_i - b_{i-1}\frac{a_i}{b_{i-1}} \equiv 0, \tag{6.1.36}$$

$$\dot{b}_i = b_i - c_{i-1}\frac{a_i}{b_{i-1}}, \tag{6.1.37}$$

$$\dot{c}_i = c_i - d_{i-1}\frac{a_i}{b_{i-1}}, \tag{6.1.38}$$

$$\dot{d}_i = d_i - e_{i-1}\frac{a_i}{b_{i-1}}, \tag{6.1.39}$$

$$\dot{e}_i = e_i, \tag{6.1.40}$$

$$\dot{f}_i = f_i - f_{i-1}\frac{a_i}{b_{i-1}}. \tag{6.1.41}$$

Repeat this for $i \geq 3$ to $i = n$ and the first two rows remain unchanged. To remove the entries containing now $\dot{b}_i$ multiply the $(i-1)^{\text{th}}$ row by $\frac{\dot{b}_i}{\dot{c}_{i-1}}$ and subtract the result from the i^{th} row as follows

$$\ddot{a}_i \equiv 0, \tag{6.1.42}$$

$$\ddot{b}_i = \dot{b}_i - \dot{c}_{i-1}\frac{\dot{b}_i}{\dot{c}_{i-1}} \equiv 0, \tag{6.1.43}$$

$$\ddot{c}_i = \dot{c}_i - \dot{d}_{i-1}\frac{\dot{b}_i}{\dot{c}_{i-1}}, \tag{6.1.44}$$

$$\ddot{d}_i = \dot{d}_i - \dot{e}_{i-1}\frac{\dot{b}_i}{\dot{c}_{i-1}}, \tag{6.1.45}$$

$$\ddot{e}_i = \dot{e}_i, \tag{6.1.46}$$

$$\ddot{f}_i = \dot{f}_i - \dot{f}_{i-1}\frac{\dot{b}_i}{\dot{c}_{i-1}}. \tag{6.1.47}$$

Repeat this for $i \geq 2$ to $i = n$ and the first row remains unchanged. To remove the entries containing now $\ddot{e}_i$ multiply the $(i+1)^{\text{th}}$ row by $\frac{\ddot{e}_i}{\ddot{d}_{i+1}}$ and subtract the result from the i^{th} row as follows

$$\dddot{a}_i \equiv 0, \tag{6.1.48}$$

$$\dddot{b}_i \equiv 0, \tag{6.1.49}$$

$$\dddot{c}_i = \ddot{c}_i, \tag{6.1.50}$$

$$\dddot{d}_i = \ddot{d}_i - \ddot{c}_{i+1}\frac{\ddot{e}_i}{\ddot{d}_{i+1}}, \tag{6.1.51}$$

$$\ddot{e}_i = \ddot{e}_i - \ddot{d}_{i+1}\frac{\ddot{e}_i}{\ddot{d}_{i+1}} \equiv 0, \tag{6.1.52}$$

$$\dddot{f}_i = \ddot{f}_i - \ddot{f}_{i+1}\frac{\ddot{e}_i}{\ddot{d}_{i+1}}. \tag{6.1.53}$$

Repeat this for $i \leq n-2$ to $i = 1$ and the last two rows remain unchanged. Lastly, to remove the entries containing now $\dddot{d}_i$ multiply the $(i+1)^{\text{th}}$ row by $\frac{\dddot{d}_i}{\ddot{c}_{i+1}}$ and subtract the result from the i^{th} row as follows

$$\ddddot{a}_i \equiv 0, \tag{6.1.54}$$

$$\ddddot{b}_i \equiv 0, \tag{6.1.55}$$

$$\ddddot{c}_i = \ddot{c}_i, \tag{6.1.56}$$

$$\ddddot{d}_i = \dddot{d}_i - \dddot{c}_{i+1}\frac{\dddot{d}_i}{\ddot{c}_{i+1}} \equiv 0, \tag{6.1.57}$$

$$\ddot{e}_i \equiv 0, \tag{6.1.58}$$

$$\ddddot{f}_i = \dddot{f}_i - \dddot{f}_{i+1}\frac{\dddot{d}_i}{\ddot{c}_{i+1}}. \tag{6.1.59}$$

The only non-zero entries left are the diagonal containing $\dddot{c}_i$ and the results vector $\ddddot{f}_i$. We only need to set the boundary conditions and then we can solve for η. The boundary conditions on η are $\eta = \eta_x = 0$ at $x = 0$ and $x = 1$. So we have

$$a_1 = b_1 = d_1 = e_1 = f_1 = 0 \text{ and } c_1 = 1 \tag{6.1.60}$$

which corresponds to $\eta = 0$ at $x = 0$,

$$a_n = b_n = d_n = e_n = f_n = 0 \text{ and } c_n = 1 \tag{6.1.61}$$

which corresponds to $\eta = 0$ at $x = 1$,

$$c_2 = 7e_1 - 2e_2(\delta x)^2 + e_3(\delta x)^4 \text{ and } a_2 = 0 \tag{6.1.62}$$

which corresponds to $\eta' = 0$ at $x = 0$ and e_1, e_2 and e_3 here are the flexibility parameters

$$c_{n-1} = 7e_1 - 2e_2(\delta x)^2 + e_3(\delta x)^4 \text{ and } e_{n-1} = 0 \tag{6.1.63}$$

this corresponds to $\eta' = 0$ at $x = 1$ and e_1, e_2 and e_3 here again are the flexibility parameters. This has been implemented in Mathematica. We should note here that for the linear case it is possible to solve (6.1.21) using a Laplace transform method. However this becomes complicated because we consider the fourth, second and zeroth derivatives of η in the wall-relation. In chapter 7 we expand our model to three dimensions, so to simplify the calculations there we only consider the second derivative of η. For this case the Laplace transform is a useful and computationally fast method. We will leave discussion of the Laplace transform until the next chapter.

6.1.3 Results for the linear model

Above we have set up the system of equations that need to be solved as well as explained the computational methods used to achieve this. Since we are using a numerical approach we need to make an initial guess for the pressure distribution over the blip, which is substituted into (6.1.21) to solve for the blip-shape η as explained above. We then use this calculated η to calculate a corrected pressure using (6.1.22). These two steps are iterated until a convergence criterion is satisfied, i.e. the change in pressure Δp between two steps in the iteration is less than some small parameter ϵ. In figures 6.2-6.5 below are results for several values of the wall flexibility parameters e_i.

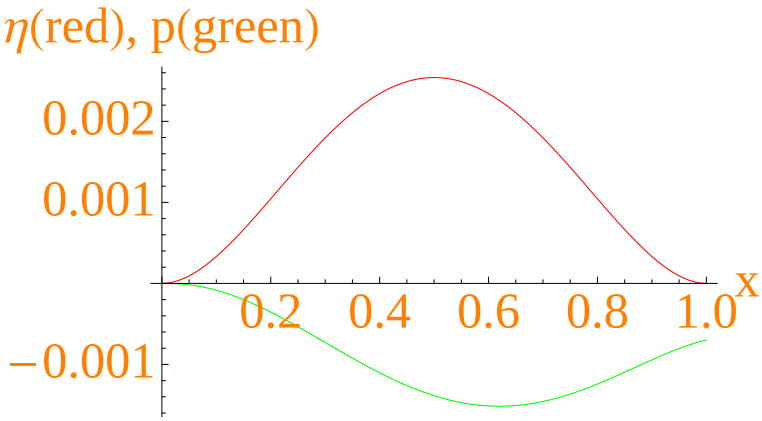

Figure 6.2: blip shape and pressure for $e_1 = -1$, $e_2 = 1$ and $e_3 = -1$

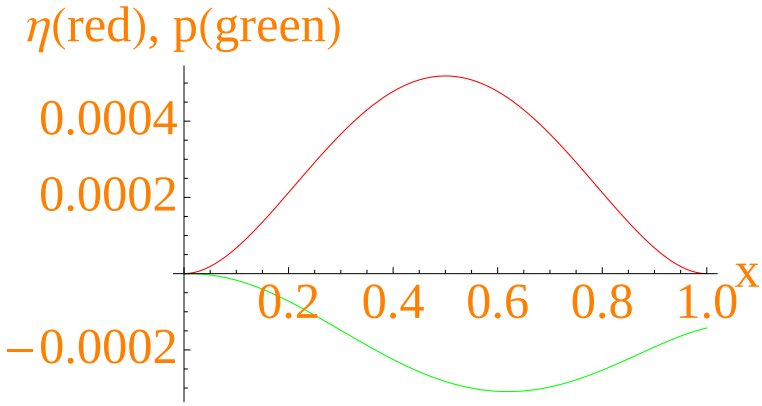

Figure 6.3: blip shape and pressure for $e_1 = -5$, $e_2 = 1$ and $e_3 = -1$

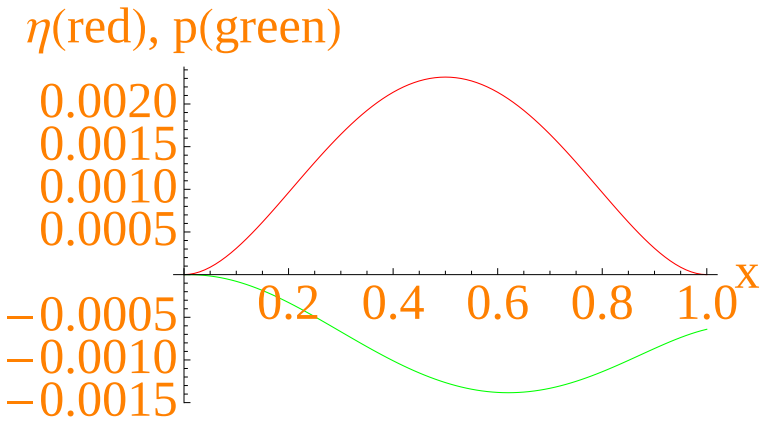

Figure 6.4: blip shape and pressure for $e_1 = -1$, $e_2 = 5$ and $e_3 = -1$

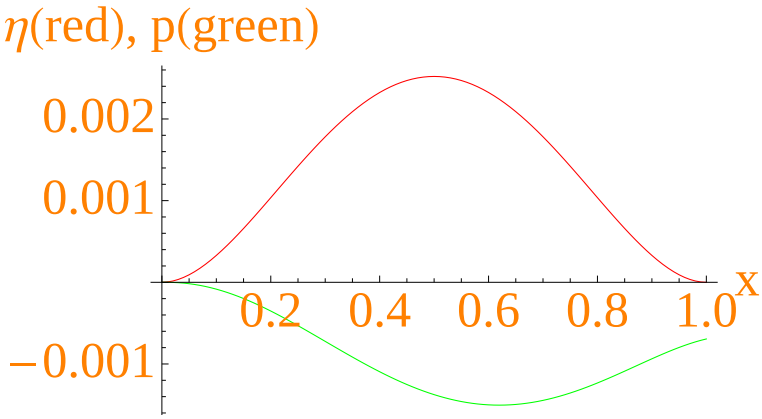

Figure 6.5: blip shape and pressure for $e_1 = -1$, $e_2 = 1$ and $e_3 = -5$

It is worth remarking here that the typical values of η, p are comparatively small at this stage (unlike later) and that the shape of η is notably sinusoidal-like.

In the results presented above in figures 6.2-6.5 we have varied e_1 to e_3 and kept $p_0 = 1$ constant. Now we investigate the effect of p_0 on the blip shape and pressure. In figures 6.6 and 6.7 we show results for doubling p_0.

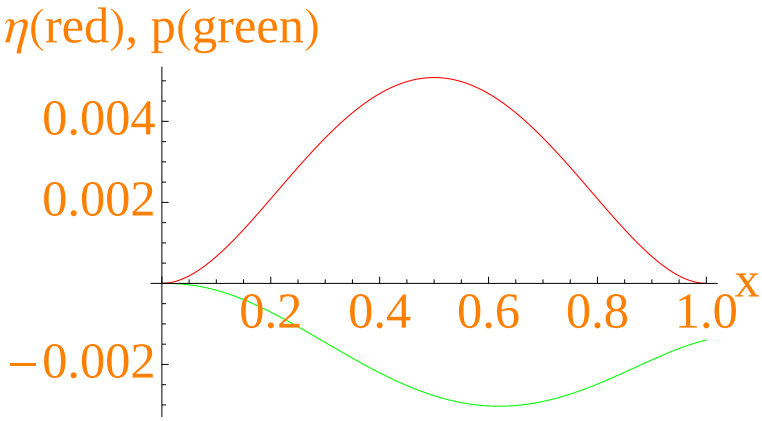

Figure 6.6: blip shape and pressure for $e_1 = -1$, $e_2 = 1$ and $e_3 = -1$ and $p_0 = 2$

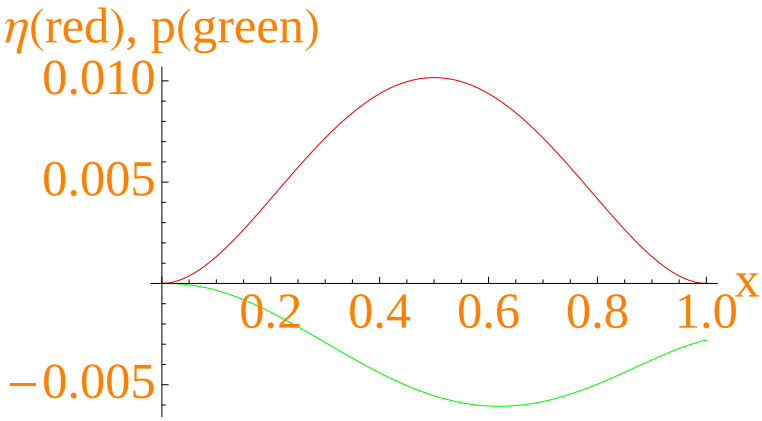

Figure 6.7: blip shape and pressure for $e_1 = -1$, $e_2 = 1$ and $e_3 = -1$ and $p_0 = 4$

As we can see doubling p_0 doubles the blip height, similarly the overall pressure dip doubles.

6.1.4 Resonance in the linear model

We now introduce the factor "a" into (6.1.21), which we have mentioned at the beginning of this chapter; as noted above "a" measures the ratio of flow strength to flexibility strength. Smaller

values of "a" correspond to larger values of the flexibility parameters. Thus

$$e_1\eta_{xxxx} + e_2\eta_{xx} + e_3\eta = a(p - p_0). \tag{6.1.64}$$

For convenience we could scale parameters e_i on "a" as follows

$$\hat{e}_i = \frac{1}{a}e_i, \tag{6.1.65}$$

but the following results show the maximum height of the blip as well as the maximum pressure over the blip as a function of the parameter "a" while keeping e_i and p_0 constant; see figures 6.8-6.15 below.

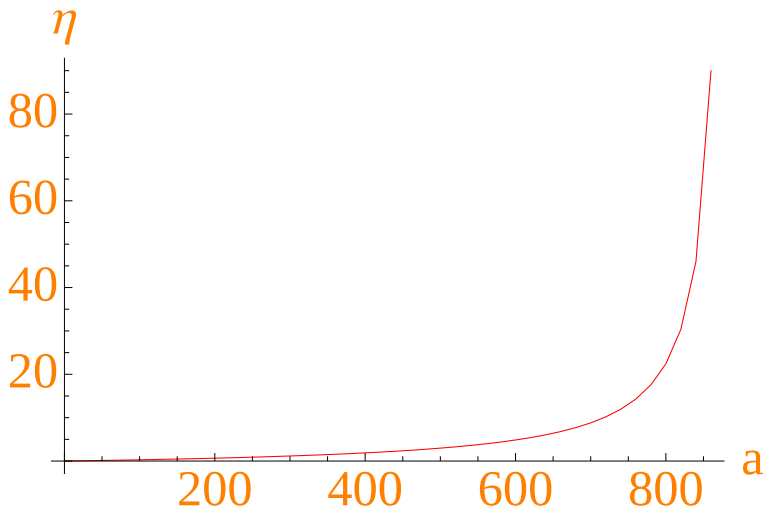

Figure 6.8: resonance plot showing η_{max} for $e_1 = -1$, $e_2 = 1$ and $e_3 = -1$

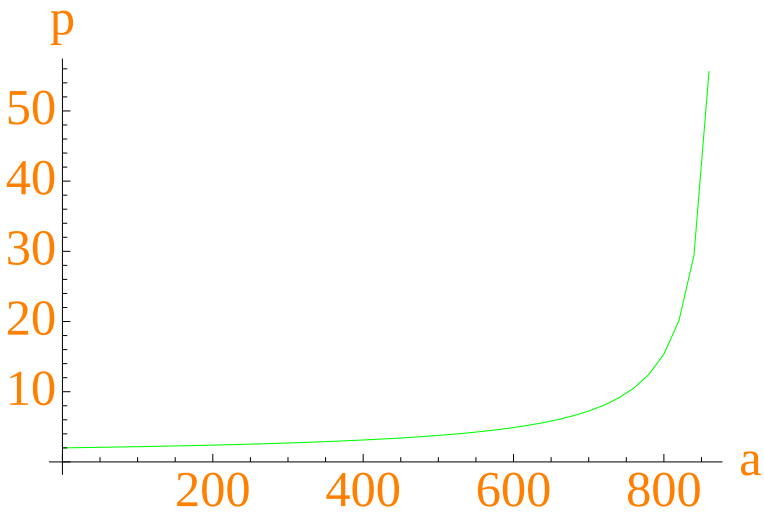

Figure 6.9: resonance plot showing p_{max} for $e_1 = -1$, $e_2 = 1$ and $e_3 = -1$

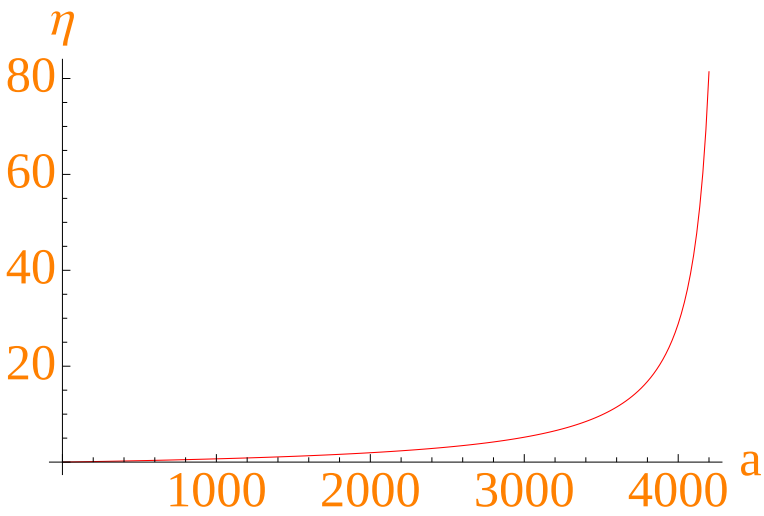

Figure 6.10: resonance plot showing η_{max} for $e_1 = -5$, $e_2 = 1$ and $e_3 = -1$

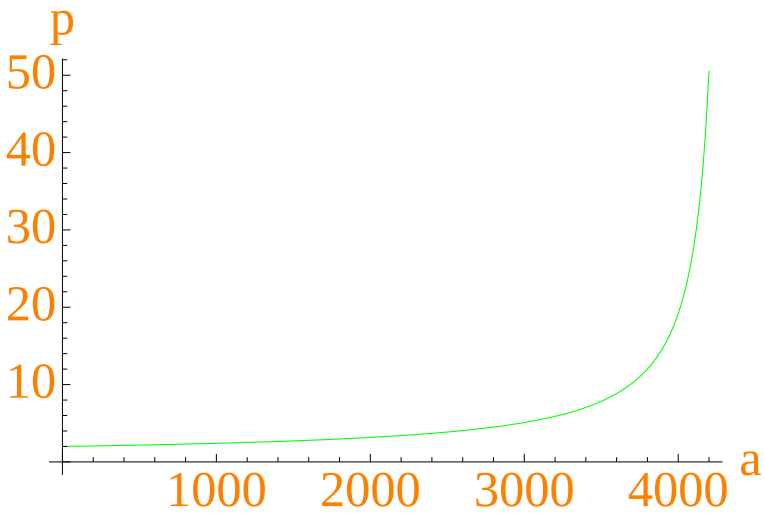

Figure 6.11: resonance plot showing p_{max} for $e_1 = -5$, $e_2 = 1$ and $e_3 = -1$

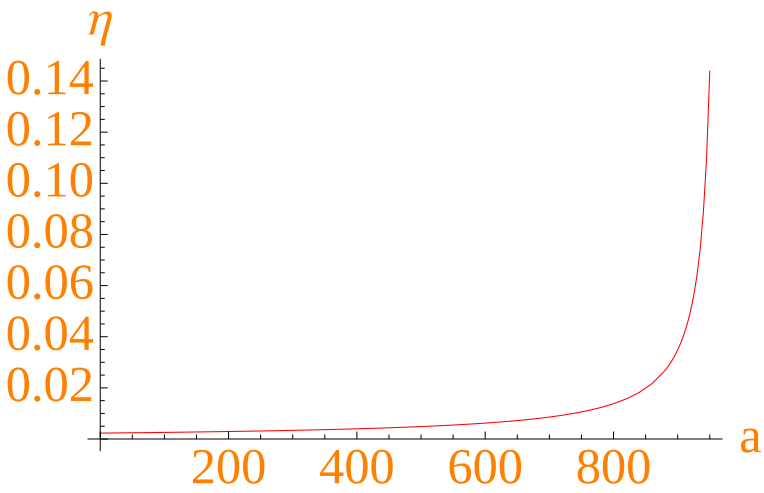

Figure 6.12: resonance plot showing η_{max} for $e_1 = -1$, $e_2 = 5$ and $e_3 = -1$

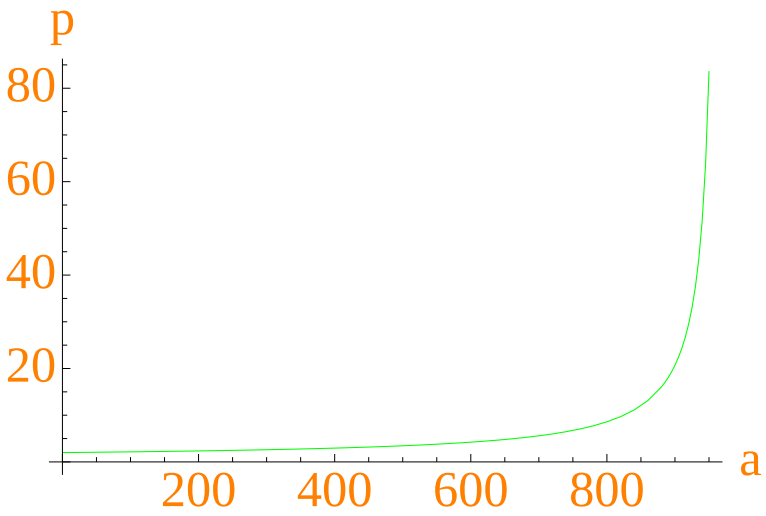

Figure 6.13: resonance plot showing p_{max} for $e_1 = -1$, $e_2 = 5$ and $e_3 = -1$

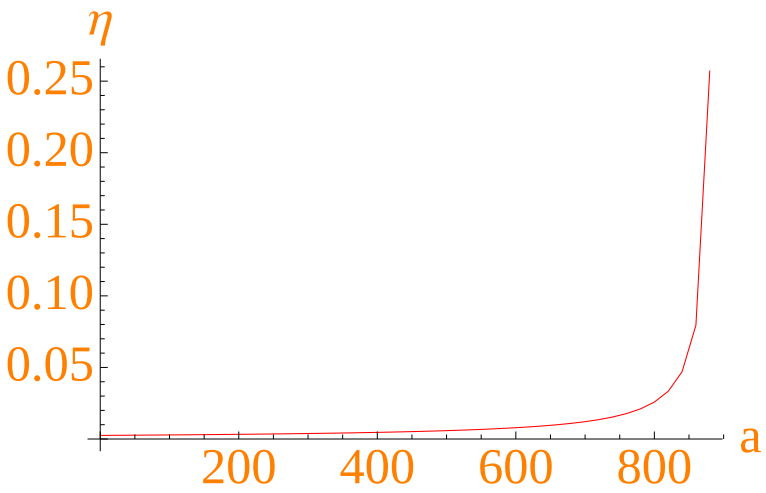

Figure 6.14: resonance plot showing η_{max} for $e_1 = -1$, $e_2 = 1$ and $e_3 = -5$

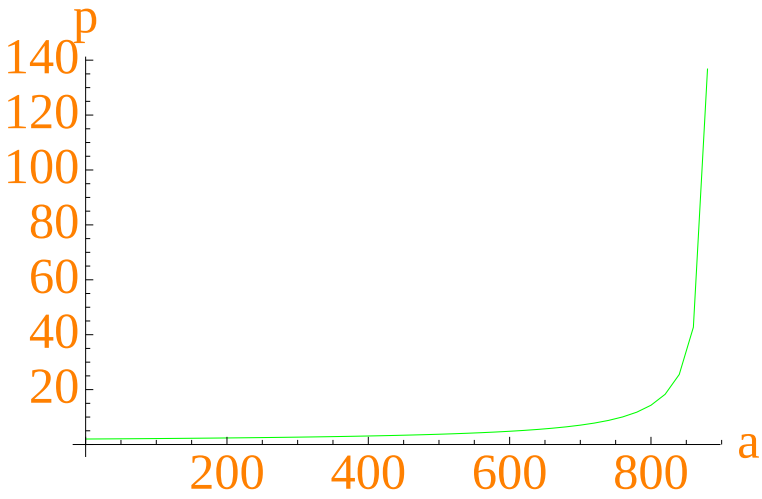

Figure 6.15: resonance plot showing p_{max} for $e_1 = -1$, $e_2 = 1$ and $e_3 = -5$

Resonance is found to occur at a finite "a" value. We can see that as we increase e_i we need a larger value of "a" to achieve resonance. However it should be noted that the effect of increasing e_1 is the strongest whereas increasing e_3 affects the resonance value for "a" very little.

When investigating the resonance graphs we draw the conclusion that resonance occurs at a finite value for "a". To give further evidence of this conclusion we present here a convergence test for larger a and a Runga-Kutta shooting method to predict "a" as an eigenvalue problem.

First the convergence test was done with the grid which was used throughout the calculations in chapter 6 with $\delta x = 0.01$ and a refined grid with $\delta x = 0.001$. In figure 6.16-6.20 below we show the graphs for both grids for values for "a" of 0, 100, 200, 300, 400, 500 and 600.

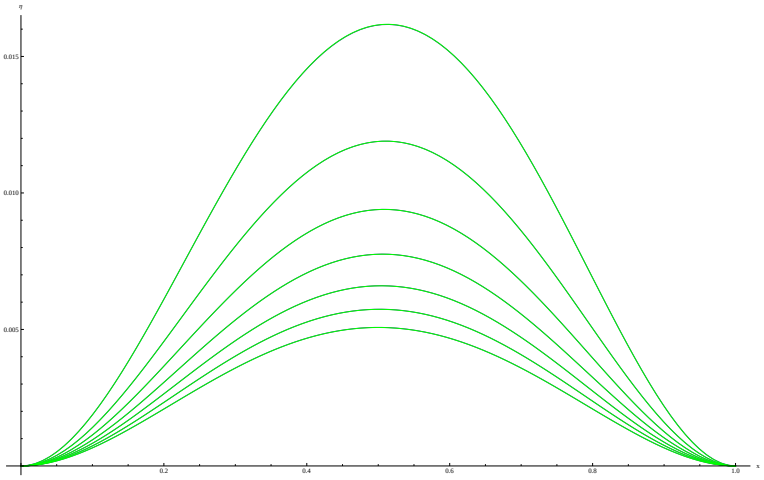

Figure 6.16: Grid test for large "a" (0, 100, 200, 300, 400, 500, 600) for $\delta x = 0.01$ (blue) and $\delta x = 0.001$ (green)

The graphs show very good agreement over the range of "a" tested. (The blue line is hardly visible as it is almost completely overlapped by the green line).

To predict the value of "a" where resonance occurs we have implemented a Runga-Kutta shooting method for the unforced system (i.e. $p_0 = 0$). We use the boundary conditions $\eta(0) = 0$, $\eta'(0) = 0$ as well as the normalisation condition $\eta''(0) = 1$ and $\eta'''(0) = L$ where the value of L needs to be adjusted such that $\eta'(1) = 0$ and "a" is found such that we have $\eta(1) = 0$ by an iterative procedure which terminates when $\eta(1) < \epsilon$ where $\epsilon = 10^{-6}$. We have done this calculation for several grids with $\delta x = 10^{-2}$, $\delta x = 0.5 * 10^{-2}$, $\delta x = 10^{-3}$ and $\delta x = 0.8 * 10^{-3}$. The resulting values for "a" are roughly 870, 875, 880 and 880 respectively. See figures .... below.

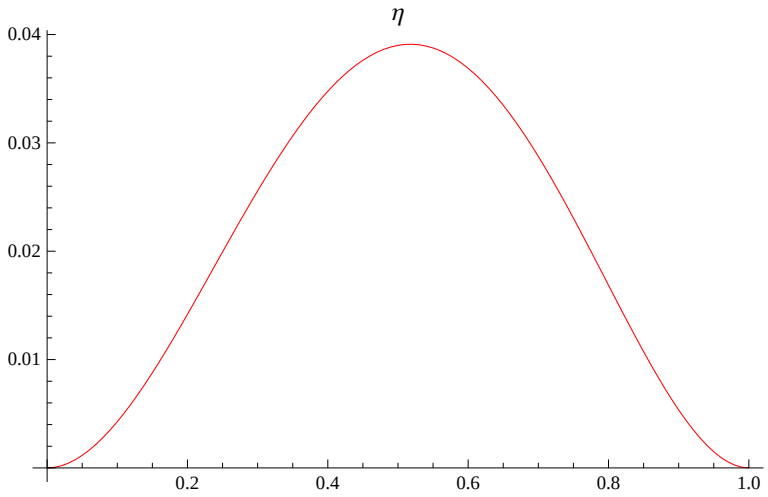

Figure 6.17: $a = 869.971$ and $\eta(1) = 7.33158 * 10^{-7}$

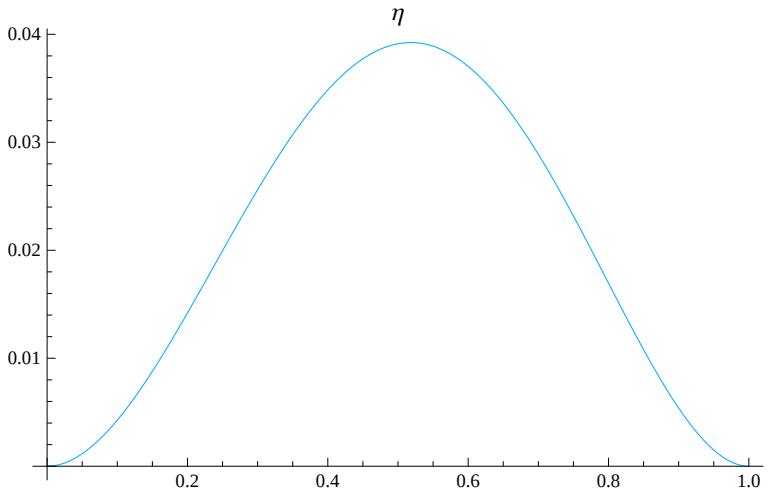

Figure 6.18: $a = 875.513$ and $\eta(1) = -6.18481 * 10^{-7}$

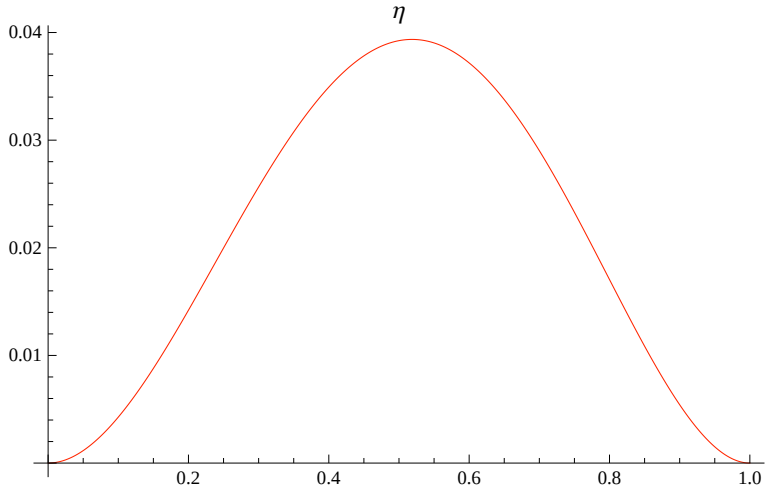

Figure 6.19: $a = 880.249$ and $\eta(1) = 6.09913 * 10^{-7}$

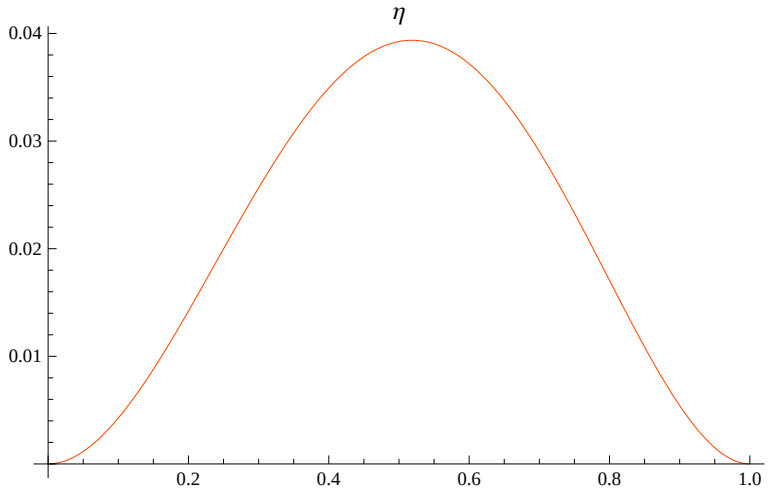

Figure 6.20: $a = 880.493$ and $\eta(1) = 8.78533 * 10^{-7}$

6.2 Nonlinear behaviour

Above we have studied the linear model for resonance; now we are investigating the nonlinear model. We have the same wall-relation as above in (6.1.21) but this time we have to solve this in conjunction with the nonlinear boundary layer equations.

6.2.1 Computational methods for the nonlinear model

So to summarize we have the following equations

$$p - p_0 = e_1\eta_{xxxx} + e_2\eta_{xx} + e_3\eta \tag{6.2.1}$$

$$u_x + v_y = 0 \qquad \text{continuity} \tag{6.2.2}$$

$$uu_x + vu_y = -p_x + u_{yy} \qquad \text{momentum} \tag{6.2.3}$$

with the boundary conditions $u = v = 0$ at $y = 0$ and $u \to y + \eta$ as $y \to \infty$. Here (6.2.1) can be solved in exactly the same way that (6.1.21) could be solved. However we cannot apply the same analytical procedure to the nonlinear boundary layer equations as in the linear case, so we need to solve them numerically. We make use of a second order centred finite differencing method in y and a first order backwards differencing method in x. So we can write (6.2.3) as

$$\bar{u}_j(\frac{u_j - \bar{u}_j}{\delta x}) + \bar{v}_j(\frac{u_{j+1} - u_{j-1}}{2\delta y}) = -(\frac{p - \bar{p}}{\delta x}) + (\frac{u_{j+1} - 2u_j + u_{j-1}}{(\delta y)^2}), \tag{6.2.4}$$

and grouping terms of u_j together we obtain

$$\left(-\frac{\bar{v}_j}{2\delta y} - \frac{1}{(\delta y)^2}\right)u_{j-1} + \left(\frac{\bar{u}_j}{\delta x} + \frac{2}{(\delta y)^2}\right)u_j + \left(\frac{\bar{v}_j}{2\delta y} - \frac{1}{(\delta y)^2}\right)u_{j+1} = \frac{\bar{u}_j^2}{\delta x} - \frac{p - \bar{p}}{\delta x}, \tag{6.2.5}$$

where we can define

$$a_j = -\frac{\bar{v}_j}{2\delta y} - \frac{1}{(\delta y)^2}, \tag{6.2.6}$$

$$b_j = \frac{\bar{u}_j}{\delta x} + \frac{2}{(\delta y)^2}, \tag{6.2.7}$$

$$c_j = \frac{\bar{v}_j}{2\delta y} - \frac{1}{(\delta y)^2}, \tag{6.2.8}$$

$$d_j = \frac{\bar{u}_j^2}{\delta x} - \frac{p - \bar{p}}{\delta x}, \tag{6.2.9}$$

where $\bar{p}$, $\bar{u}$ and $\bar{v}$ are the values of p, u and v at the previous step in x. This set-up allows us to write the equations in matrix form $\mathbf{M}.\underline{u} = \underline{d}$, which we can solve for u with the integration over y using the Thomas algorithm explained above. In this case it is a little simpler to solve as we only have a tridiagonal matrix. Again we have to remove the off-diagonal entries. We start be removing the diagonal containing entries a_j by multiplying row $j-1$ by $\frac{a_j}{b_{j-1}}$ and subtracting the result from row i as follows:

$$\dot{a}_j = a_j - b_{j-1}\frac{a_j}{b_{j-1}} \equiv 0, \tag{6.2.10}$$

$$\dot{b}_j = b_j - c_{j-1}\frac{a_j}{b_{j-1}}, \tag{6.2.11}$$

$$\dot{c}_j = c_j, \tag{6.2.12}$$

$$\dot{d}_j = d_j - d_{j-1}\frac{a_j}{b_{j-1}}. \tag{6.2.13}$$

Repeat this for $j = 2$ to $j = n$, entries in the first row remain unchanged. Next we remove the diagonal now containing entries $\dot{c}_j$ by multiplying row $j+1$ by $\frac{\dot{c}_j}{\dot{b}_{j+1}}$ and subtracting the result from row i as follows

$$\ddot{a}_j \equiv 0, \tag{6.2.14}$$

$$\ddot{b}_j = \dot{b}_j, \tag{6.2.15}$$

$$\ddot{c}_j = \dot{c}_j - \dot{b}_j\frac{\dot{c}_j}{\dot{b}_{j+1}} \equiv 0, \tag{6.2.16}$$

$$\ddot{d}_j = \dot{d}_j - \dot{d}_{j-1}\frac{\dot{c}_j}{\dot{b}_{j+1}}. \tag{6.2.17}$$

Repeat this for $j = n-1$ to $j = 1$, entries in the last row remain unchanged. We also have boundary conditions on u, which can be implemented as follows:

$$a1 = c1 = d_1 = 0 \text{ and } b_1 = 1 \tag{6.2.18}$$

which corresponds to $u = 0$ at $y = 0$ and

$$a_n = c_n = 0 \text{ and } b_n = 1 \text{ and } d_n = J + \eta \tag{6.2.19}$$

which corresponds to $u = y + \eta$ as $y \to \infty$. Having obtained a solution for u we need to solve for v. This calculation is straightforward from the continuity equation, as we have

$$v_j = v_{j-1} - \frac{\delta y}{2\delta x}(u_j - \bar{u}_j + u_{j-1} - \bar{u}_{j-1}) \text{ and } v_1 = 0. \tag{6.2.20}$$

In order to solve for the pressure we have to impose boundary conditions on (6.2.5) as $y \to \infty$. Hence

$$\bar{u}_J \left(\frac{u_J - \bar{u}_J}{\delta x} \right) + v_J = - \left(\frac{p - \bar{p}}{\delta x} \right). \tag{6.2.21}$$

Solving this for the pressure gives

$$p = \bar{p} - \bar{u}_J(u_J - \bar{u}_J) - v_j \delta x. \tag{6.2.22}$$

So far we have solved for the y-integration at a specified position x_i. We will repeat this process for each step in x along the range we are considering.

6.2.2 Results for the nonlinear model

Above we have set up the system of equations that need to be solved and we have explained the methods we are using to solve it. The procedure to calculate the flow over a blip is again to guess the pressure distribution over the blip, then to use this guessed pressure to calculate η from (6.2.1) as explained above. The resulting η is then used to solve the nonlinear boundary layer equations, which will give us a correction for the pressure. These steps need to be repeated until a convergence criterion is fulfilled, namely that the pressure difference, δp, from one iteration to the next is less than some small parameter ϵ, where $\epsilon = 10^{-3}$ and $\Delta x = \Delta y = 0.01$. In figures 6.21-6.32 below are

results for the pressure p, the blip shape η and the wall shear τ for several values of the flexibility parameters e_i, with $p_0 = 1$.

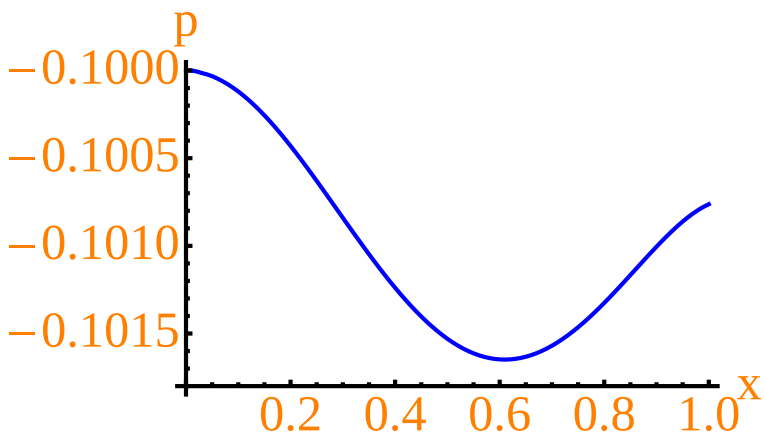

Figure 6.21: pressure plot for $e_1 = -1$, $e_2 = 1$ and $e_3 = -1$

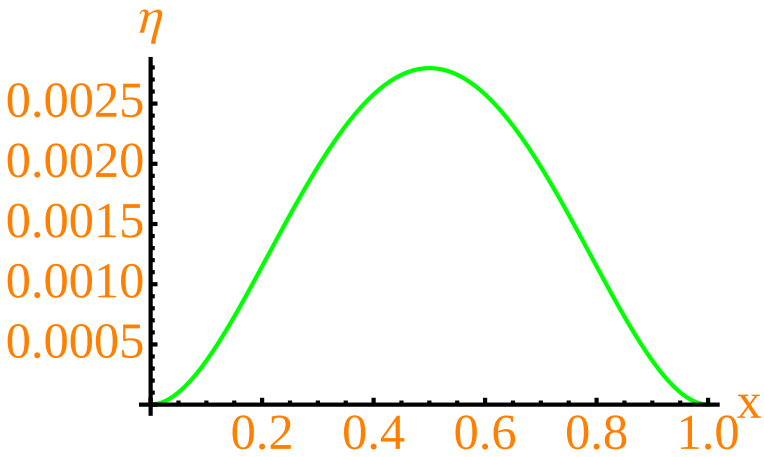

Figure 6.22: η plot for $e_1 = -1$, $e_2 = 1$ and $e_3 = -1$

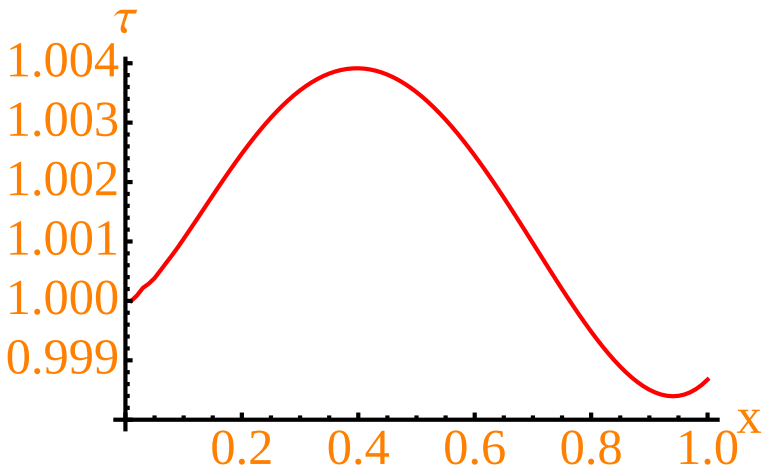

Figure 6.23: τ plot for $e_1 = -1$, $e_2 = 1$ and $e_3 = -1$

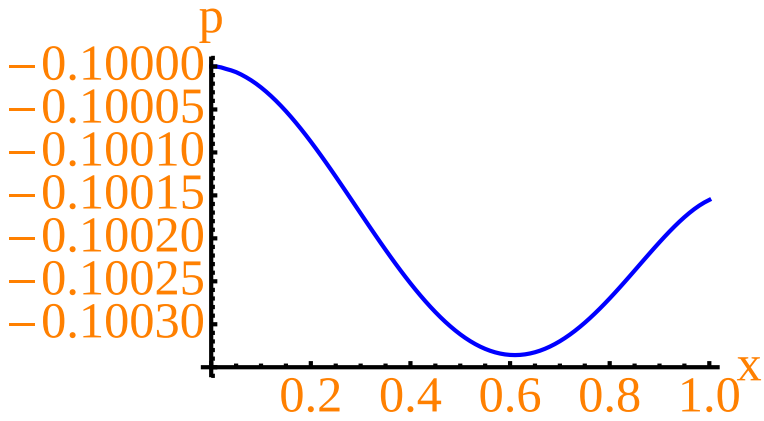

Figure 6.24: pressure plot for $e_1 = -5$, $e_2 = 1$ and $e_3 = -1$

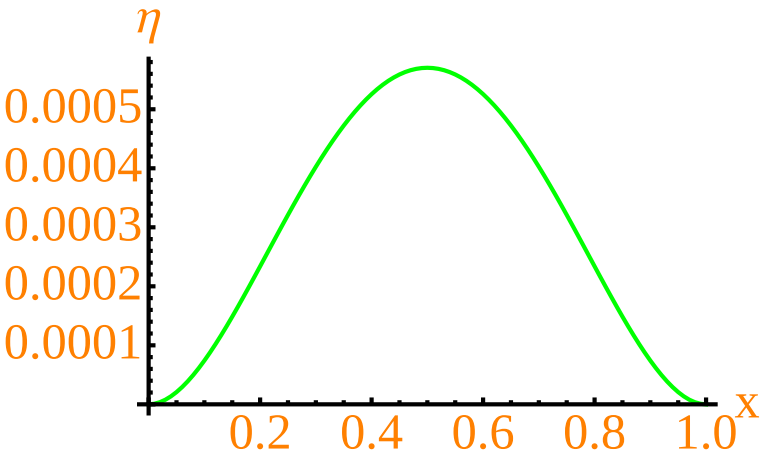

Figure 6.25: η plot for $e_1 = -5$, $e_2 = 1$ and $e_3 = -1$

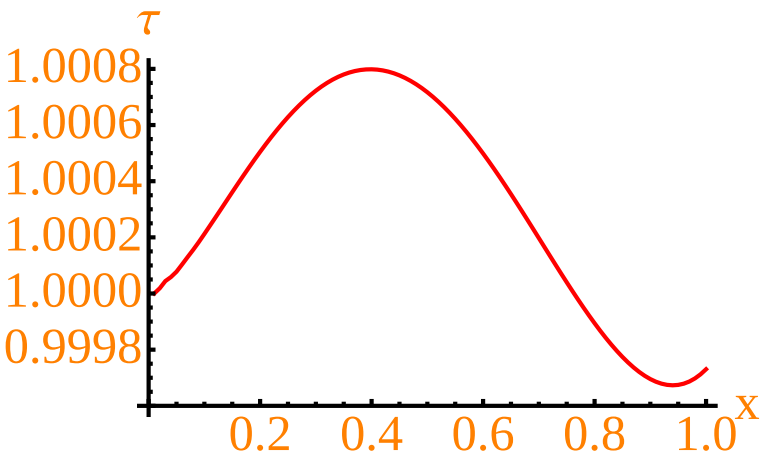

Figure 6.26: τ plot for $e_1 = -5$, $e_2 = 1$ and $e_3 = -1$

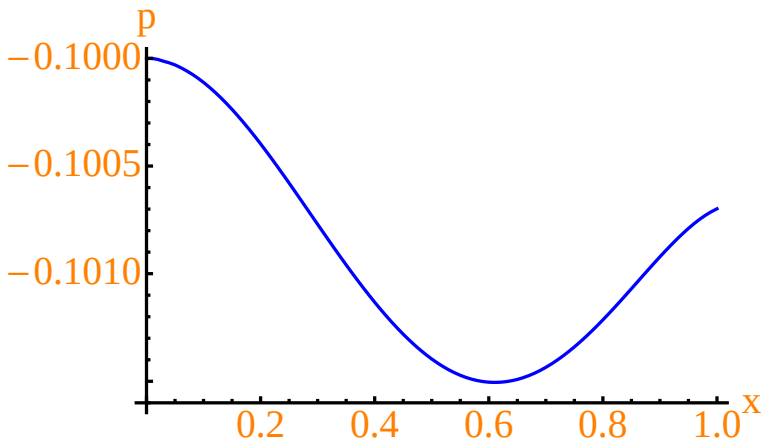

Figure 6.27: pressure plot for $e_1 = -1$, $e_2 = 5$ and $e_3 = -1$

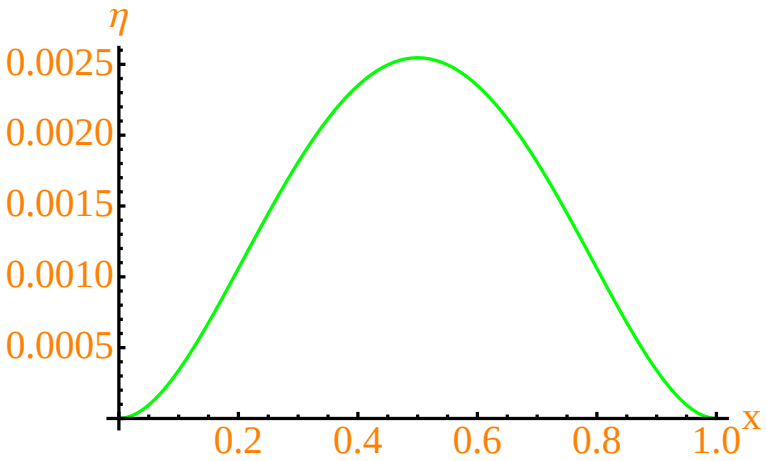

Figure 6.28: η plot for $e_1 = -1$, $e_2 = 5$ and $e_3 = -1$

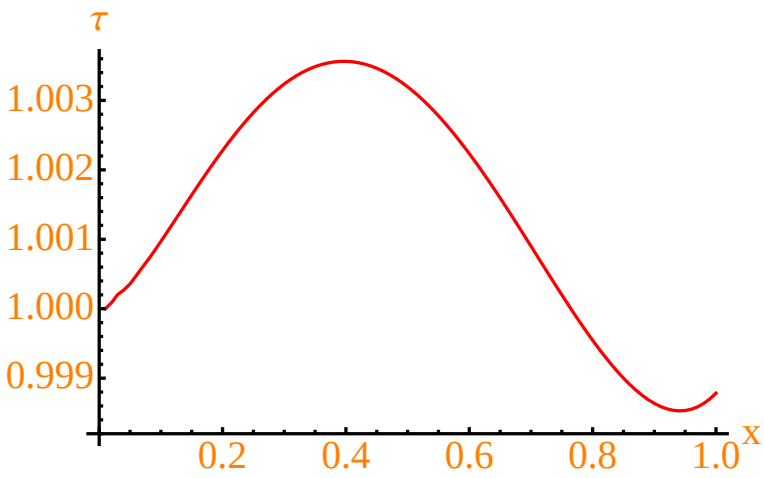

Figure 6.29: τ plot for $e_1 = -1$, $e_2 = 5$ and $e_3 = -1$

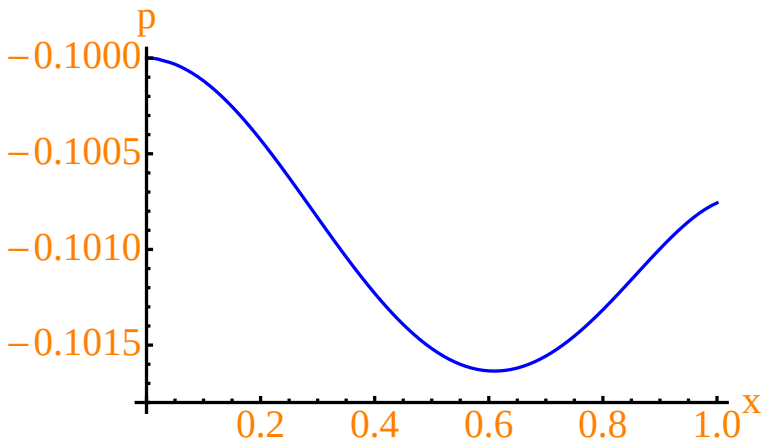

Figure 6.30: pressure plot for $e_1 = -1$, $e_2 = 1$ and $e_3 = -5$

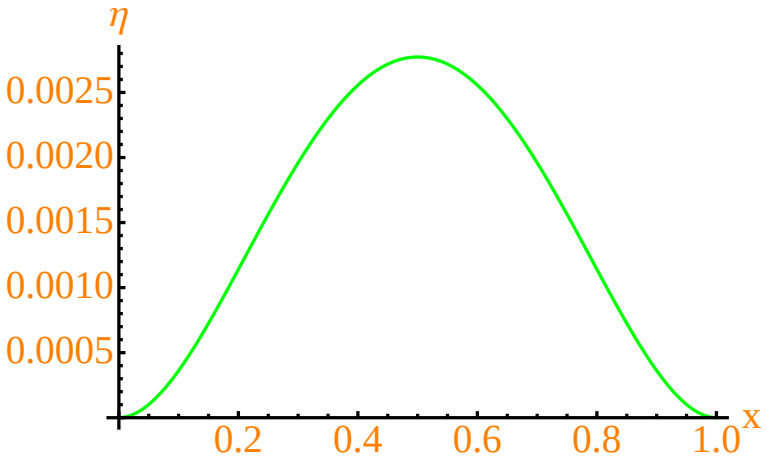

Figure 6.31: η plot for $e_1 = -1$, $e_2 = 1$ and $e_3 = -5$

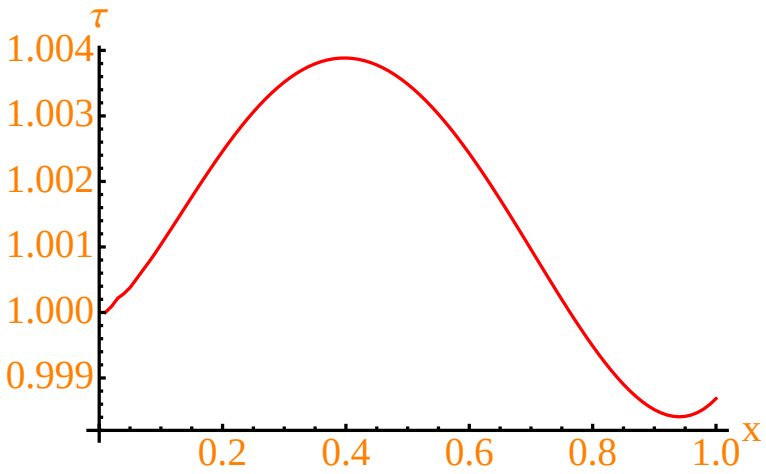

Figure 6.32: τ plot for $e_1 = -1$, $e_2 = 1$ and $e_3 = -5$

The results at this stage have τ_{wall} remaining near unity, in line with η, p being small, and so there is close corespondance with the linearised results of earlier in this chapter. In the above results we have kept $p_0 = 1$ constant. Results presented in figures 6.33-6.38 show the effect of doubling p_0.

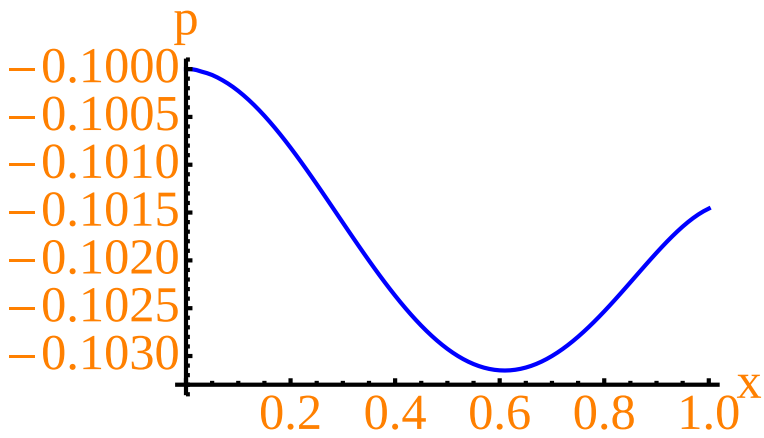

Figure 6.33: pressure plot for $e_1 = -1$, $e_2 = 1$ and $e_3 = -1$ and $p_0 = 2$

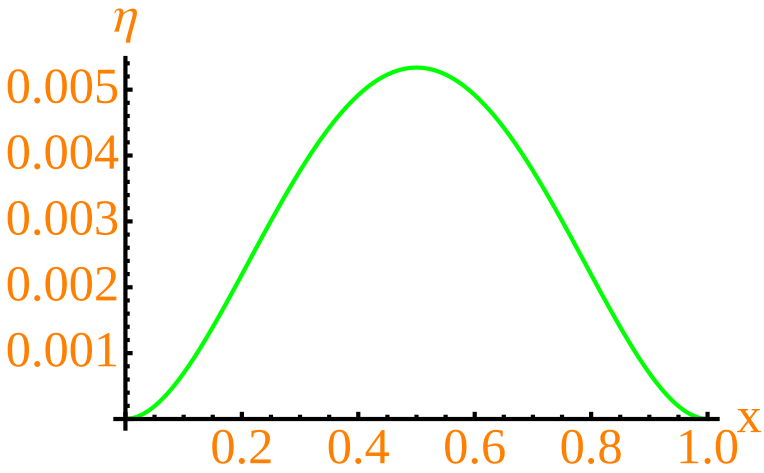

Figure 6.34: η plot for $e_1 = -1$, $e_2 = 1$ and $e_3 = -1$ and $p_0 = 2$

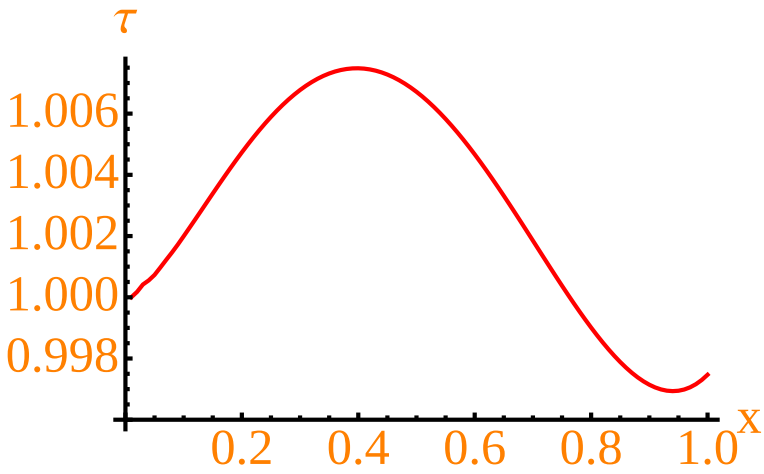

Figure 6.35: τ plot for $e_1 = -1$, $e_2 = 1$ and $e_3 = -1$ and $p_0 = 2$

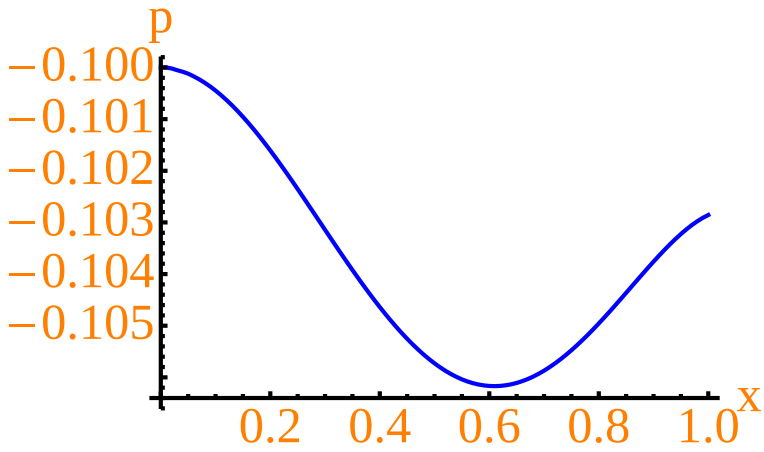

Figure 6.36: pressure plot for $e_1 = -1$, $e_2 = 1$ and $e_3 = -1$ and $p_0 = 4$

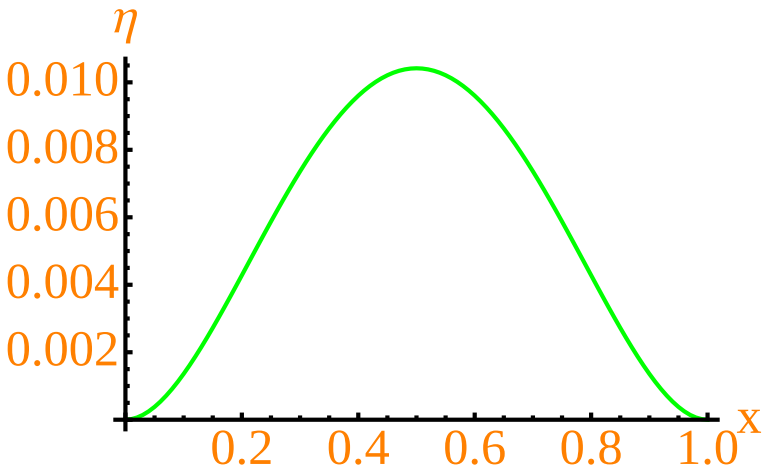

Figure 6.37: η plot for $e_1 = -1$, $e_2 = 1$ and $e_3 = -1$ and $p_0 = 4$

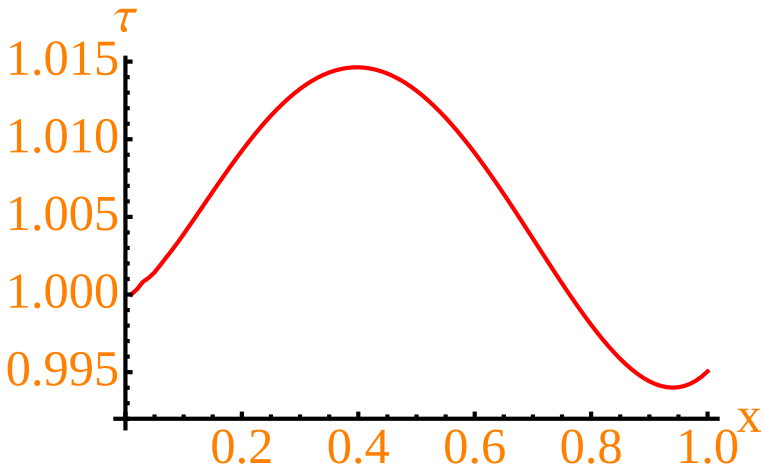

Figure 6.38: τ plot for $e_1 = -1$, $e_2 = 1$ and $e_3 = -1$ and $p_0 = 4$

As we can see doubling p_0 doubles the blip height. The dip in the pressure and the increase in the wall shear also double.

6.2.3 Resonance in the nonlinear model

We now introduce a parameter "b", which in effect is the same as the parameter "a" above, as it measures the ratio of the flow strength to the flexibility strength and we use it to scale parameters

e_i as follows

$$\hat{e}_i = \frac{1}{b} e_i \tag{6.2.23}$$

The following results show the maximum blip height in green, the maximum pressure over the blip in blue, the maximum wall-shear in red and the minimum wall-shear in orange, see figures 6.39-6.42 below.

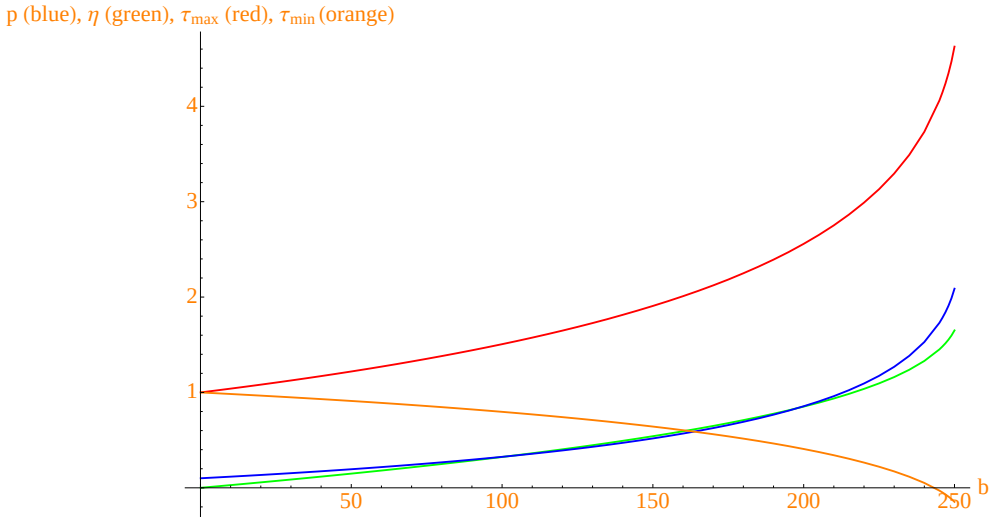

Figure 6.39: resonance plot for $e_1 = -1$, $e_2 = 1$ and $e_3 = -1$

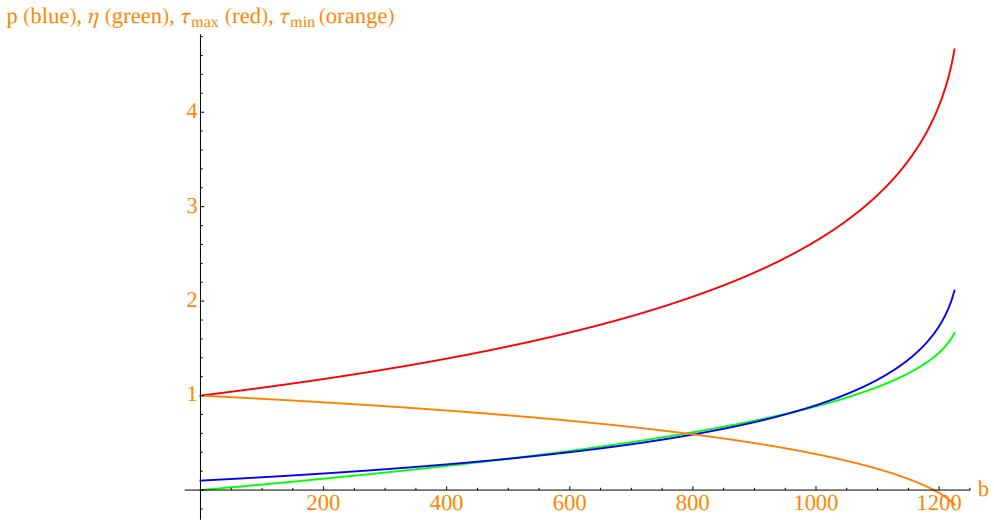

Figure 6.40: resonance plot for $e_1 = -5$, $e_2 = 1$ and $e_3 = -1$

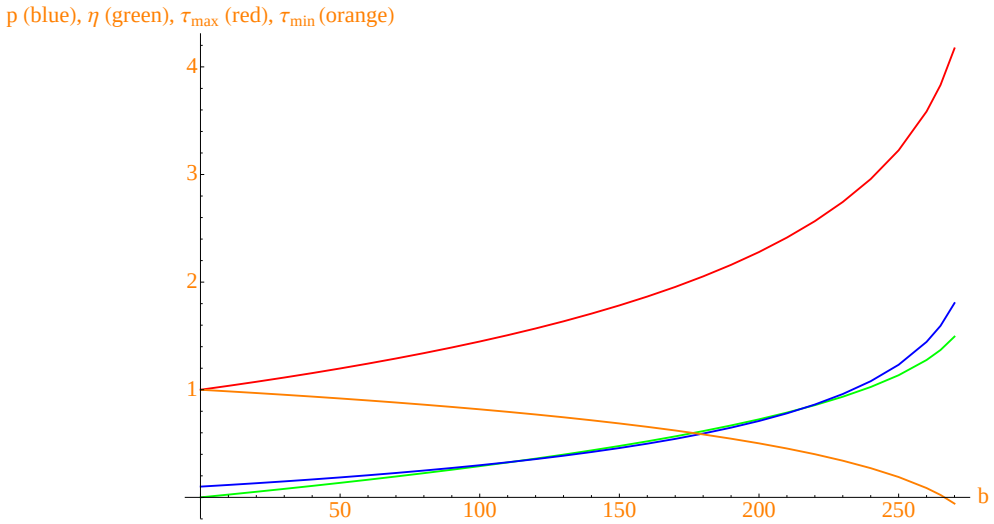

Figure 6.41: resonance plot for $e_1 = -1$, $e_2 = 5$ and $e_3 = -1$

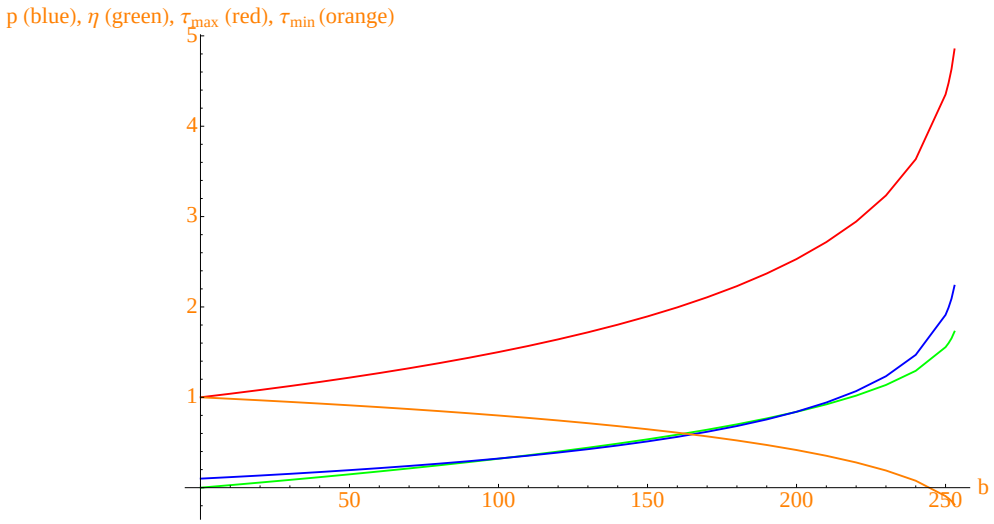

Figure 6.42: resonance plot for $e_1 = -1$, $e_2 = 1$ and $e_3 = -5$

Resonance is again encountered. The first aspect that can be noted is that a smaller value for "b" than "a" seems to be necessary to achieve resonance, which means that non-linear effects are important. Other than this we can make the same observations as before, that as we increase e_i we need a larger value of "b" to achieve resonance and again with e_1 being the most influential and e_3 being the least.

In the above results we can see that the minimum wall shear becomes negative near resonance. Where the wall shear goes negative is conventionally taken to indicate flow reversal.

6.3 Comparison between linear and nonlinear model

As mentioned above resonance values for "a" in the linear case and "b" in the nonlinear case differ. Here we compare directly the pressure and blip shape for three values of the parameters "a" and "b". We keep parameters e_1, e_2 and e_3 constant at $(-1, 1, -1)$. Figures 6.43-6.45 below show the blip shape for the linear model (dark green, dashed), the blip shape for the nonlinear model (light green, solid), the pressure for the linear model (purple, dashed) and the pressure for the nonlinear model (blue, solid):

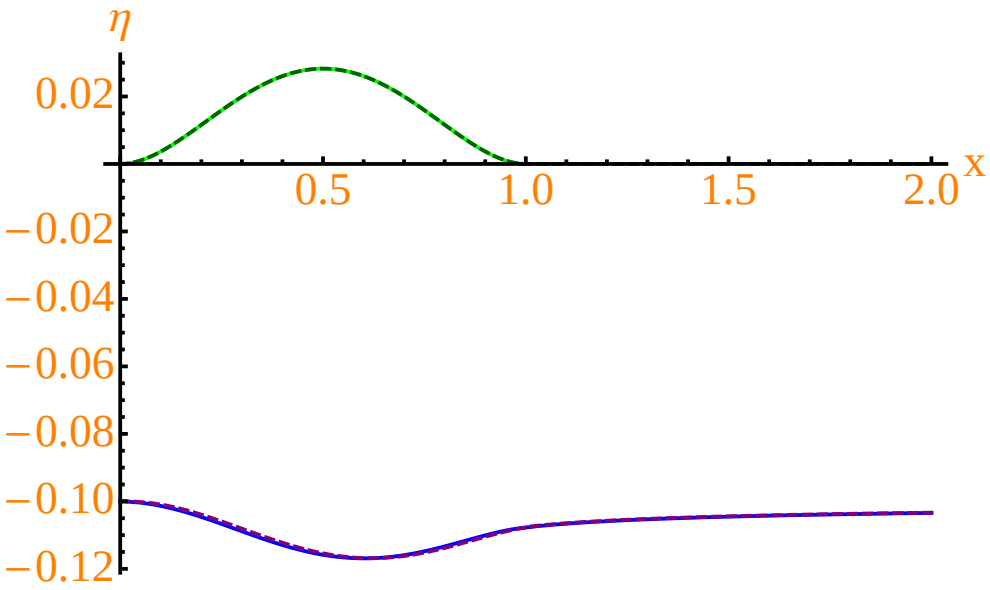

Figure 6.43: comparison between linear (dashed) and nonlinear (solid) for $b = a = 10$

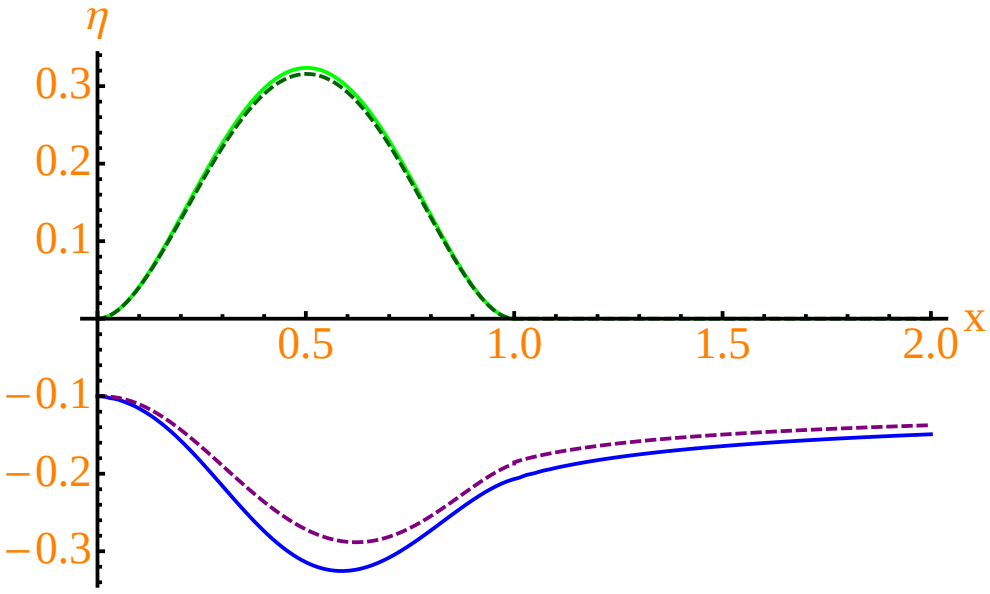

Figure 6.44: comparison between linear (dashed) and nonlinear (solid) for $b = a = 100$

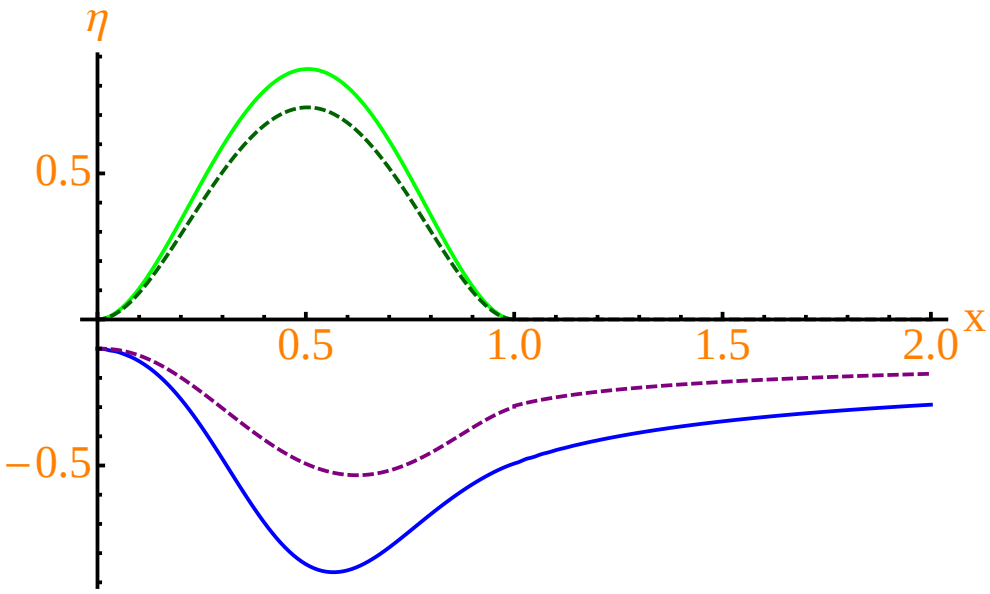

Figure 6.45: comparison between linear (dashed) and nonlinear (solid) for $b = a = 200$

We can see that at small "a" and "b" the models agree very well but as we increase "a" and "b" the linear model underestimates the blip height and the corresponding response of the pressure. So for the next section, which is examining the effect of several blips on resonance, we will use the nonlinear model.

6.4 Several blips

It may also be of interest to examine the effect several blips in a row may have on resonance. We will use the nonlinear model here, and the arrangement of the blips is shown in fig 6.46 below.

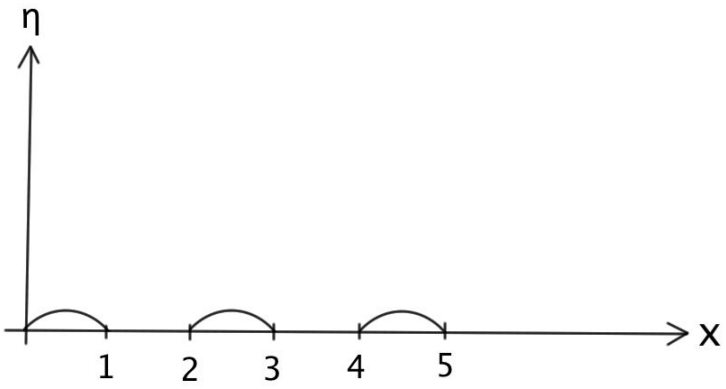

Figure 6.46: blip arrangement

We use the same methods as described in subsection 6.2.1 above for the nonlinear model and the overall procedure is that we guess the pressure over the whole range, use this guess to calculate the first blip shape η_1, use this result to calculate the resulting boundary layer over the whole range and obtain a correction for the pressure. These steps need to be iterated until the results have converged. Only then do we move on to the next blip and repeat the same procedure; we do this for each blip in turn. It should be noted that bearing in mind the governing equations we have assumed that there is no upstream influence. This is in the sense that the first blip shape is not influenced by the second blip, neither is the second by the third, and so on, provided that there is no substantial flow separation.

6.4.1 Results for several blips

Figures 6.47-6.52 show results for the pressure, blip-shape and wall shear for two and four blips. Here $p_0 = 1$ unless otherwise stated.

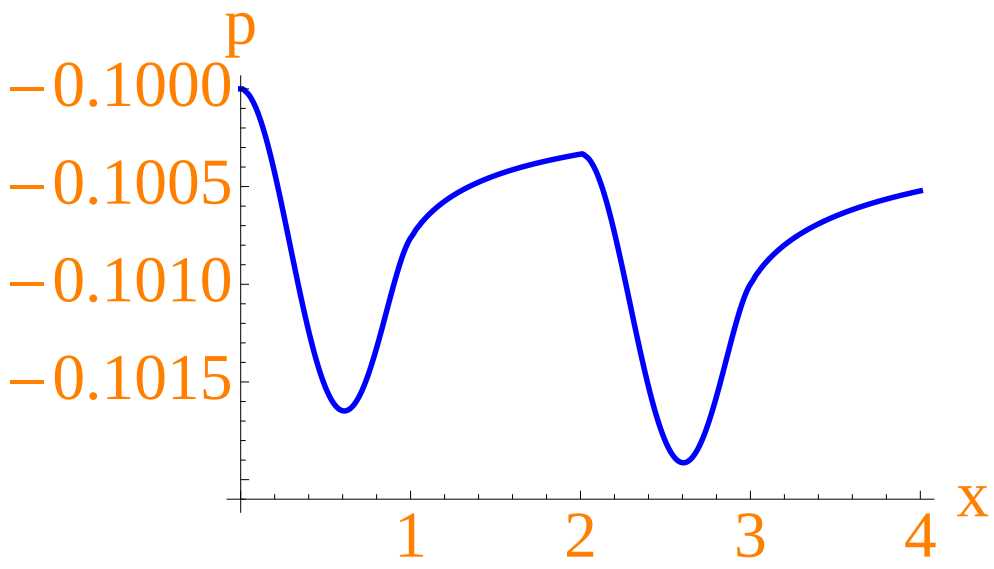

Figure 6.47: 2 blips plot for $e_1 = -1$, $e_2 = 1$ and $e_3 = -1$

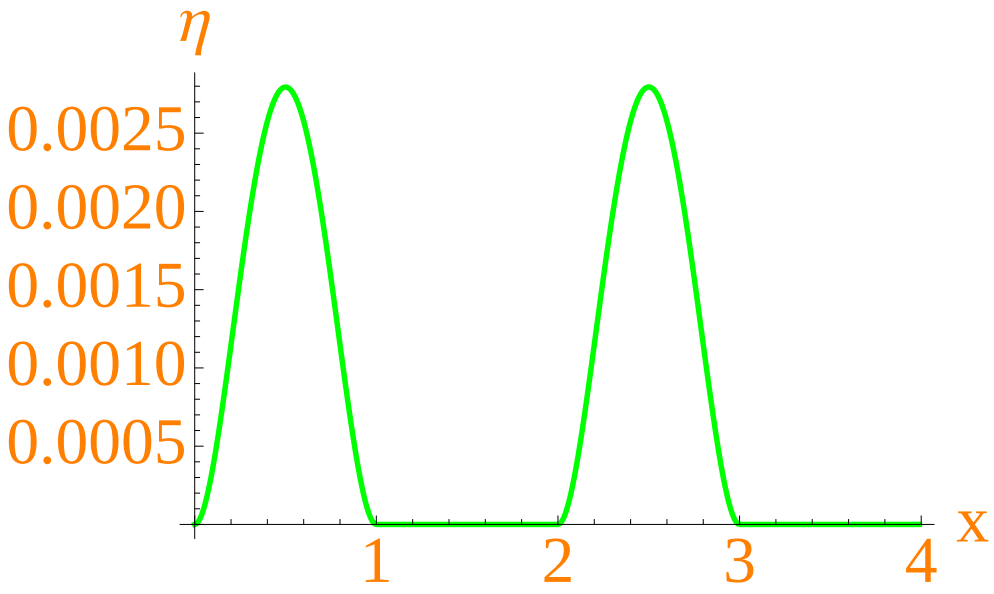

Figure 6.48: 2 blips plot for $e_1 = -1$, $e_2 = 1$ and $e_3 = -1$

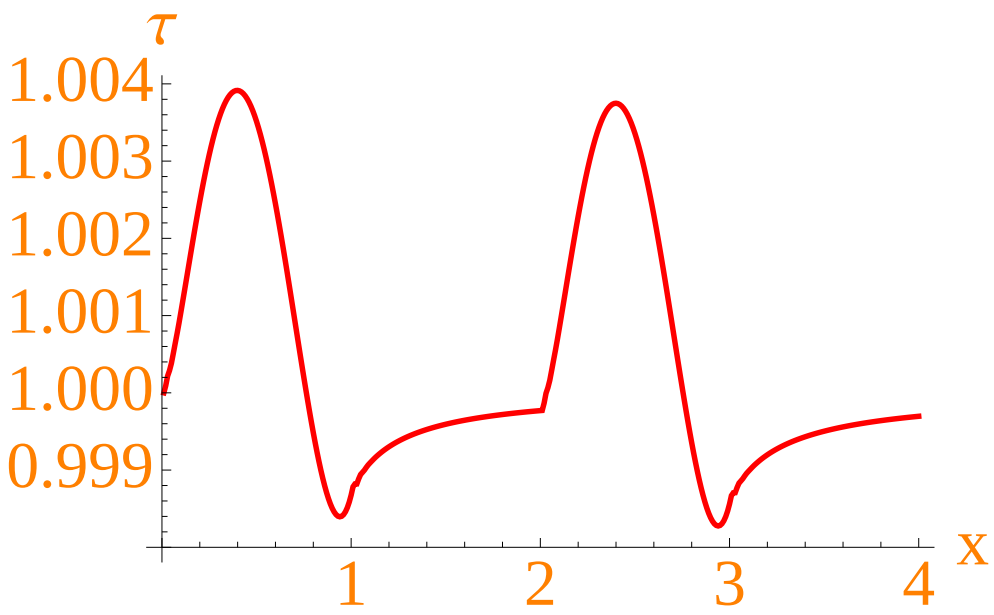

Figure 6.49: 2 blips plot for $e_1 = -1$, $e_2 = 1$ and $e_3 = -1$

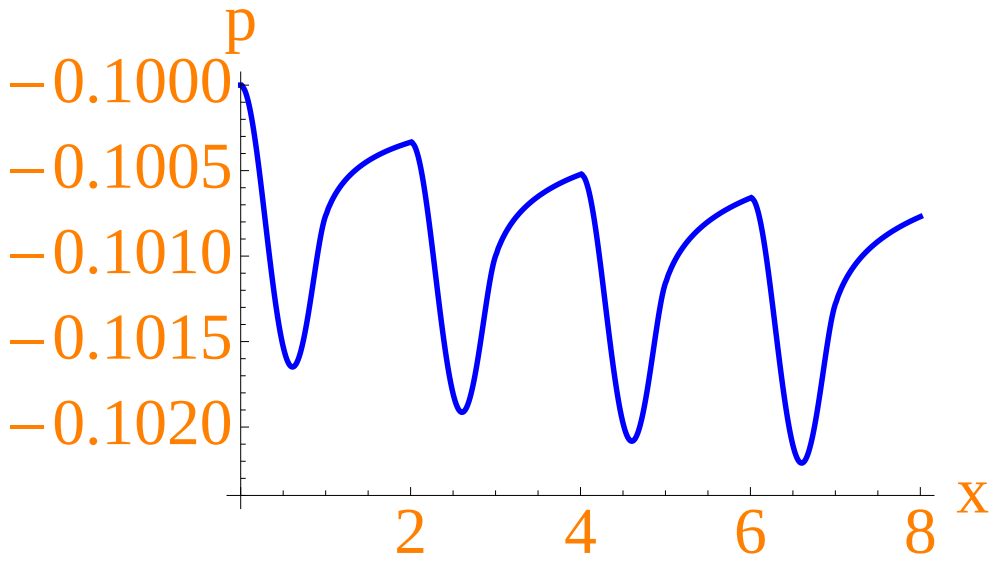

Figure 6.50: 4 blips plot for $e_1 = -1$, $e_2 = 1$ and $e_3 = -1$

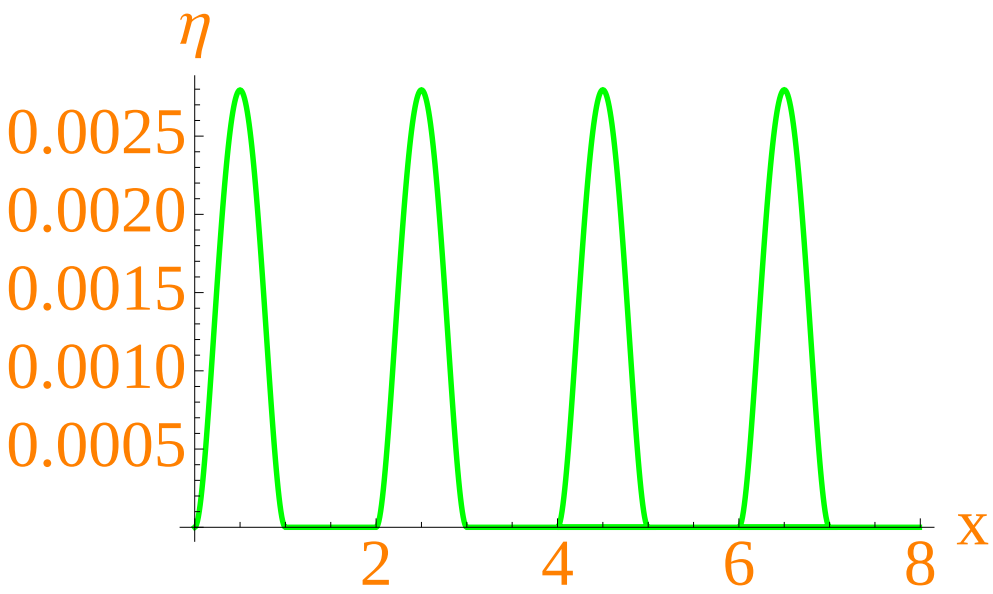

Figure 6.51: 4 blips plot for $e_1 = -1$, $e_2 = 1$ and $e_3 = -1$

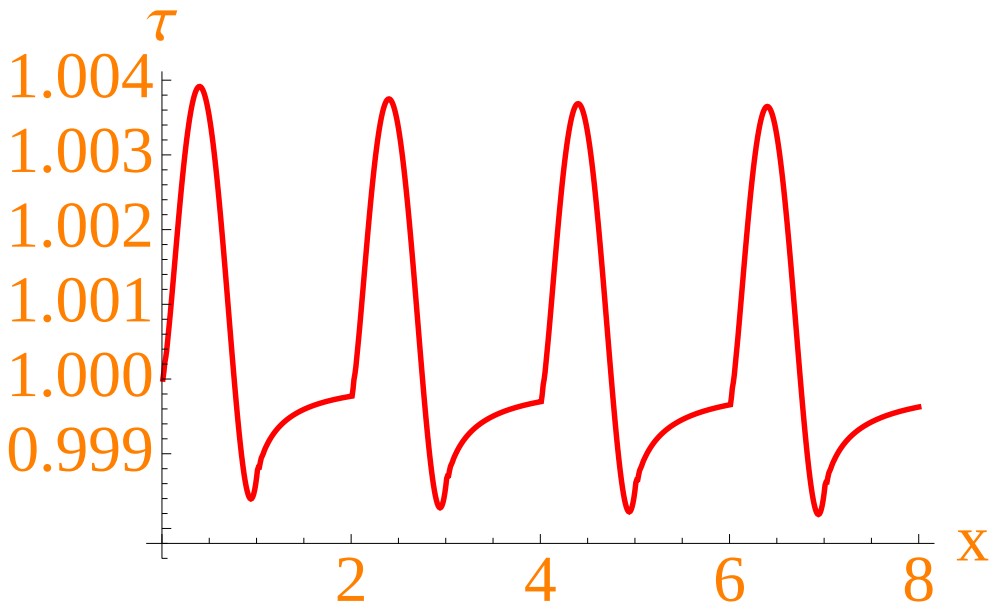

Figure 6.52: 4 blips plot for $e_1 = -1$, $e_2 = 1$ and $e_3 = -1$

We can see that as we increase the number of blips the effects accumulate most notably in the

pressure, but there is also a slight decrease in the wall-shear curves after each blip. The blip shapes themselves alter little at this level.

6.4.2 Resonance for several blips

Now, we investigate the effect an increase in blips has on resonance. Figures 6.53-6.54 below show resonance plots for two and four blips, with maximum pressure (blue), maximum blip height (green), maximum wall shear (red) and minimum wall shear (orange).

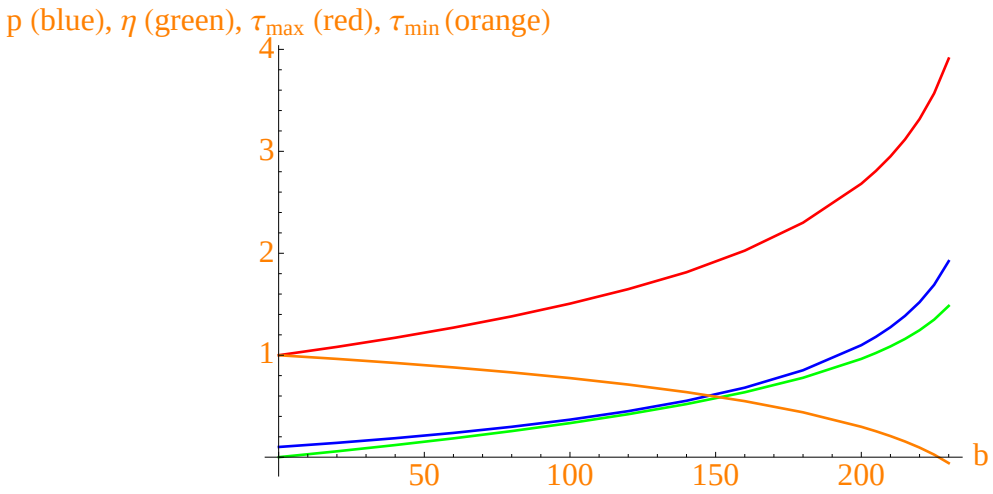

Figure 6.53: 2 blips resonance plot for $e_1 = -1$, $e_2 = 1$ and $e_3 = -1$

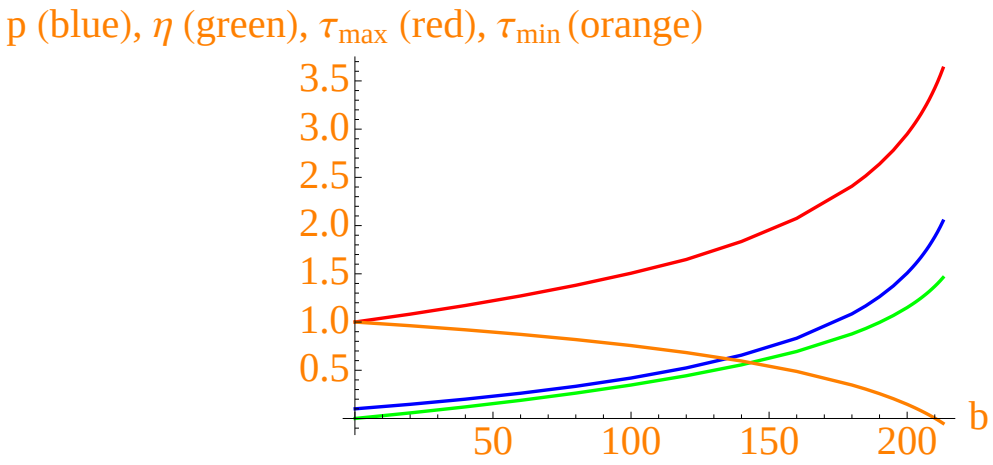

Figure 6.54: 4 blips resonance plot for $e_1 = -1$, $e_2 = 1$ and $e_3 = -1$

An interesting quantity to note here is the minimum wall shear, since a zero wall-shear indicates a possibility for separation. From the figures 6.34, 6.49 and 6.50 above we can see that the b-value at which the wall-shear becomes negative decreases as the blip number increases.

Chapter 7

For a three-dimensional flexible short blip

All the theoretical work in the thesis up to this stage has been on two-dimensional flow and interactions with a flexible wall. The focus moves on now to the modelling of fully three-dimensional properties. These properties are, or should be, more realistic in practical terms for all the contexts of interest, of course. The ideas and techniques developed in the previous chapters for two dimensions apply equally well here although there are extra aspects involved in three dimensions as we shall see. The three-dimensional theory for given wall-bump shapes was instigated by [54] and continued by [62–65].

In this chapter we work towards the full three-dimensional problem for flexible shapes (blips) in several steps. The non-dimensional length scales here are such that the typical z-scale (in the third spatial direction, i.e. spanwise) is of the same order as the streamwise x-scale, while the wall-layer thickness in terms of the normal coordinate y is as in the two-dimensional setting of earlier chapters. See [38, 54]. Here each calculation is treated separately and the slices at each z_i are independent, i.e. there is no interaction across z. This approach is described in detail in section 7.2.

Our previous two-dimensional calculations could be interpreted as an infinite "strip" of flexible material rather than a blip in three dimensions as shown in figure 7.1 below. So as a first approximation we take the two-dimensional problem and repeat the calculation for various values of x_0 and x_1 as if "slicing" straight through a three-dimensional blip. These x_0 and x_1 values would represent the edges of the slices through a circle projected onto the xz-plane, say, as shown in figure 7.2.

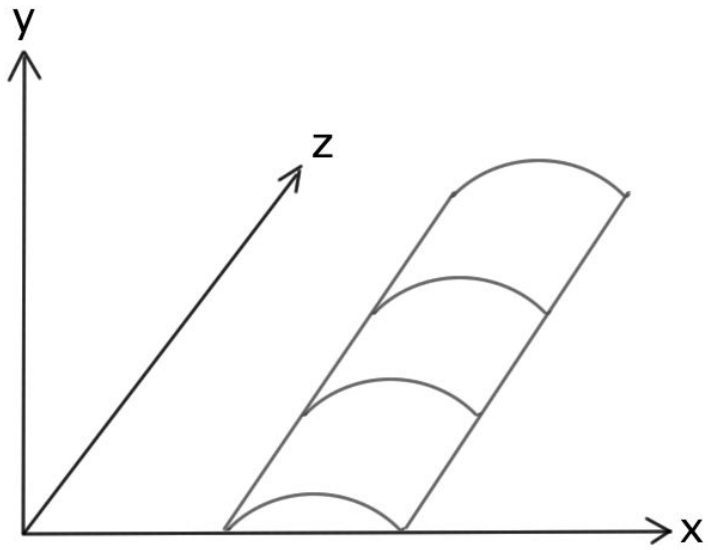

Figure 7.1: Schematic of two-dimensional "blip" as three-dimensional "strip"

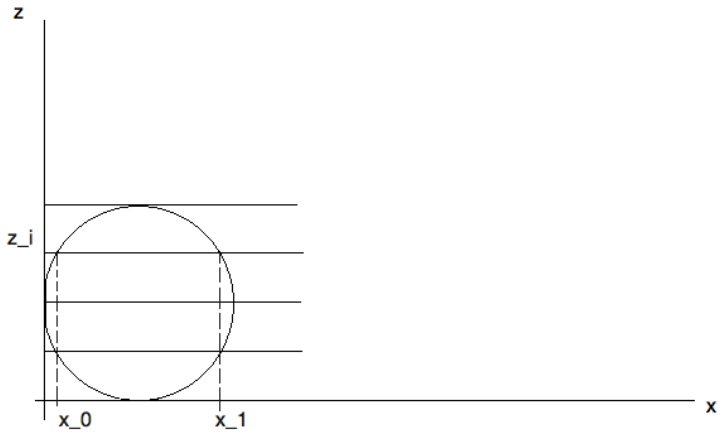

Figure 7.2: Schematic of set up for calculations

For the next approximation, in section 7.3, we calculate a quasi three-dimensional problem using the skewed shears method. The calculation proceeds similarly to the above but now we make use of the Laplace transform method, as described in section 7.1, to solve the equations as mentioned in previous chapters. This approach takes the interaction of the pressure across z into account.

Finally, in section 7.4, we work on the genuine three-dimensional problem. We take two different approaches, the first being to work with η_{2D}, which requires more complicated boundary conditions. The second approach is to work with $\int_0^x \eta_{2D} dx \equiv \eta_{3D}$ directly. This approach has the advantage that it uses the same simple boundary conditions as the two-dimensional problem but now an extra term appears in the equation, which requires some care. Concluding comments are provided in section 7.5.

7.1 Laplace transform method

For linear cases we can solve the wall relations, equations (6.1.21-6.1.22) derived in chapter 6, with a Laplace transform. However, here we only keep the term $e_2\eta_{2D}$ on the right-hand side of (6.1.21),

which reduces to

$$e_2\eta''_{2D}(x) = p - p_0 \tag{7.1.1}$$

So the equation we actually need to solve inside the blip is

$$e_2\eta''_{2D}(x) = \frac{Ai'(0)}{\int_0^\infty Ai(q)dq\Gamma(\frac{1}{3})}\int_0^x \eta_{2D}(q)(x-q)^{-\frac{2}{3}}dq - p_0, \tag{7.1.2}$$

for $\eta_{2D}(x)$, with e_2, p_0, $Ai(0)$, $\Gamma(\frac{1}{3})$ again being prescribed constants. It makes sense here to divide through by e_2:

$$\eta''_{2D}(x) = \alpha\int_0^x \eta_{2D}(q)(x-q)^{-\frac{2}{3}}dq - \pi_0, \tag{7.1.3}$$

where $\alpha = \frac{Ai'(0)}{e_2\int_0^\infty Ai(q)dq\Gamma(\frac{1}{3})}$ and $\pi_0 = \frac{p_0}{e_2}$. It is noted that for the settings of interest currently α is negative. Moreover although the focus in this particular section returns to the earlier scenario of two-dimensional interactions essentially the same methodology and results go through for the three-dimensional interactions which are of most interest in the current chapter: this merely involves an origin shift in the streamwise coordinate x as will be seen in detail in subsequent sections.

We will be applying the Laplace transform, which is defined as follows,

$$F(s) = \int_0^\infty e^{-st}f(t)dt, \tag{7.1.4}$$

for a given function $f(t)$, and the inverse transform is

$$f(t) = \frac{1}{2\pi i}lim_{T\to\infty}\int_{\gamma-iT}^{\gamma+iT} e^{st}F(s)ds, \tag{7.1.5}$$

where s is a complex variable of integration, i.e. $s = \sigma + iw$. We also use the rule for differentiation and the convolution theorem. The Laplace transform for the first derivative $f'(t)$ is $sF(s) - f(0)$ and the Laplace transform for the second derivative is $s^2F(s) - sf(0) - f'(0)$. The convolution

theorem states that the convolution function

$$(f * g)(t) = \int_0^t f(\tau)g(t-\tau)d\tau. \tag{7.1.6}$$

has $F(s)G(s)$ as its transform.

Now, applying the Laplace transform to (7.1.3) gives

$$s^2\eta^*_{2D}(s) - s\eta_{2D}(0) - \eta'_{2D}(0) = \alpha\eta^*_{2D}(s)\int_0^\infty q^{-\frac{2}{3}}e^{-sq}dq - \int_0^\infty \pi_0 e^{-sq}dq. \tag{7.1.7}$$

To evaluate the two integrals appearing in the above expression we make the substitution $Q = sq$ and $dQ = sdq$. The first integral becomes

$$s^{-\frac{1}{3}}\int_0^\infty Q^{-\frac{2}{3}}e^{-Q}dQ = s^{-\frac{1}{3}}\Gamma(\frac{1}{3}) \tag{7.1.8}$$

and the second integral becomes $\frac{\pi_0}{s}$. Substituting the above results back into (7.1.7) gives the transform equation

$$s^2\eta^*_{2D}(s) - s\eta_{2D}(0) - \eta'_{2D}(0) = \alpha\eta^*_{2D}(s)s^{-\frac{1}{3}}\Gamma(\frac{1}{3}) - s^{-1}\pi_0 \tag{7.1.9}$$

and solving for $\eta^*_{2D}(s)$ we obtain

$$\eta^*_{2D}(s) = \frac{s\eta_{2D}(0) + \eta'_{2D}(0) - s^{-1}\pi_0}{s^2 + \tilde{\alpha}s^{-\frac{1}{3}}} \tag{7.1.10}$$

where $\tilde{\alpha} = -\Gamma(\frac{1}{3})\alpha$ which is a positive real quantity. We now apply the inverse Laplace transform to (7.1.10) to obtain an expression for $\eta_{2D}(x)$,

$$2\pi i\eta_{2D}(x) = \int_{\gamma-i\infty}^{\gamma+i\infty} \frac{s\eta_{2D}(0) + \eta'_{2D}(0) - s^{-1}\pi_0}{s^2 + \tilde{\alpha}s^{-\frac{1}{3}}}e^{sx}ds. \tag{7.1.11}$$

Here we need to be careful with the integration due to the $s^{-\frac{1}{3}}$ term in the integrand. We can

however make use of a keyhole contour as shown below in figure 7.3 in order to apply Cauchy's Residue theorem.

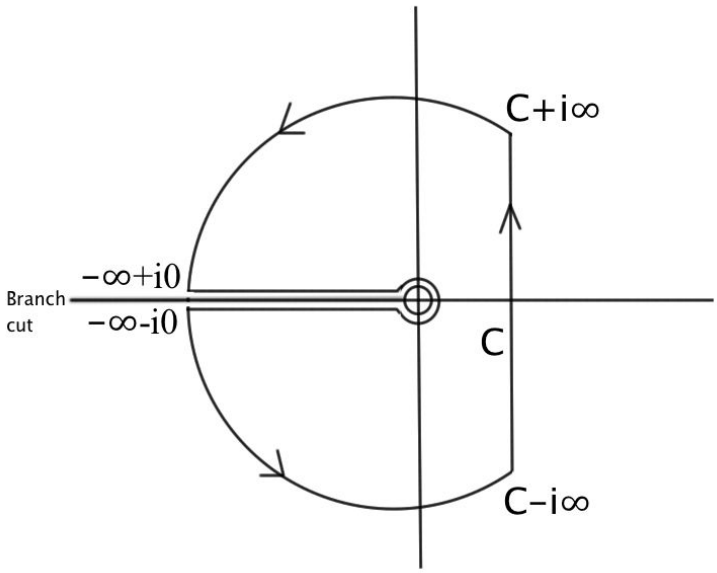

Figure 7.3: Schematic of the keyhole contour

The branch cut is to deal with the $s^{-\frac{1}{3}}$ term which can be written as $s^{-\frac{1}{3}} = r^{-\frac{1}{3}}e^{-\frac{i\theta}{3}}$, where we define θ such that $-\pi < \theta < \pi$. In the limit as the radius of the circular parts of the contour in figure 7.3 tends to infinity essentially the integral contains contributions from the paths along the real negative axis and the poles, according to Cauchy's Residue theorem. In order to locate the poles we need to solve $s^2 + \tilde{\alpha}s^{-\frac{1}{3}} = 0$, which yields just two poles at $s = \tilde{\alpha}^{\frac{3}{7}}e^{\frac{3\pi i}{7}}$ and $s = \tilde{\alpha}^{\frac{3}{7}}e^{-\frac{3\pi i}{7}}$ on account of the definition of θ above. So (7.1.11) becomes

$$2\pi i\eta_{2D}(x) = \int_0^\infty \frac{-r\eta_{2D}(0) + \eta'_{2D}(0) + r^{-1}\pi_0}{r^2 + \tilde{\alpha}r^{-\frac{1}{3}}e^{\frac{i\pi}{3}}}e^{-rx}dr - \int_0^\infty \frac{-r\eta_{2D}(0) + \eta'_{2D}(0) + r^{-1}\pi_0}{r^2 + \tilde{\alpha}r^{-\frac{1}{3}}e^{-\frac{i\pi}{3}}}e^{-rx}dr + 2\pi i\Sigma(Res) \tag{7.1.12}$$

The residues can be calculated analytically but the integrals need to be determined numerically, this requires some caution. First we note that the denominators are complex conjugates. This

allows us to combine the integrals and obtain a denominator that is real. We have:

$$I = \int_0^\infty \frac{-r\eta_{2D}(0) + \eta'_{2D}(0) + r^{-1}\pi_0}{r^2 + \tilde{\alpha}r^{-\frac{1}{3}}e^{\frac{i\pi}{3}}} e^{-rx} dr - \int_0^\infty \frac{-r\eta_{2D}(0) + \eta'_{2D}(0) + r^{-1}\pi_0}{r^2 + \tilde{\alpha}r^{-\frac{1}{3}}e^{-\frac{i\pi}{3}}} e^{-rx} dr \quad (7.1.13)$$

$$I = \int_0^\infty \frac{(-r\eta_{2D}(0) + \eta'_{2D}(0) + r^{-1}\pi_0)(r^2 + \tilde{\alpha}r^{-\frac{1}{3}}e^{-\frac{i\pi}{3}} - r^2 - \tilde{\alpha}r^{-\frac{1}{3}}e^{\frac{i\pi}{3}})}{(r^2 + \tilde{\alpha}r^{-\frac{1}{3}}e^{\frac{i\pi}{3}})(r^2 + \tilde{\alpha}r^{-\frac{1}{3}}e^{-\frac{i\pi}{3}})} e^{-rx} dr \text{ or} \quad (7.1.14)$$

$$I = \tilde{\alpha}\int_0^\infty \frac{(-r\eta_{2D}(0) + \eta'_{2D}(0) + r^{-1}\pi_0)(e^{-\frac{i\pi}{3}} - e^{\frac{i\pi}{3}})}{r^4 + \tilde{\alpha}^2 r^{-\frac{2}{3}} + r^2\tilde{\alpha}r^{-\frac{1}{3}}(e^{-\frac{i\pi}{3}} + e^{\frac{i\pi}{3}})} r^{-\frac{1}{3}} e^{-rx} dr \quad (7.1.15)$$

and since $e^{-\frac{i\pi}{3}} - e^{\frac{i\pi}{3}} = i\sqrt{3}$ and $e^{-\frac{i\pi}{3}} + e^{\frac{i\pi}{3}} = 1$ we have

$$I = i\sqrt{3}\tilde{\alpha}\int_0^\infty \frac{(-r\eta_{2D}(0) + \eta'_{2D}(0) + r^{-1}\pi_0)}{r^{\frac{13}{3}} + \tilde{\alpha}^2 r^{-\frac{1}{3}} + r^2\tilde{\alpha}} e^{-rx} dr. \quad (7.1.16)$$

To simplify this integral we make the substitution $r = s^3$ and $dr = 3s^2 ds$ as follows:

$$I = i\sqrt{3}\tilde{\alpha}\int_0^\infty \frac{(-s^3\eta_{2D}(0) + \eta'_{2D}(0) + s^{-3}\pi_0)}{s^{13} + \tilde{\alpha}^2 s^{-1} + s^6\tilde{\alpha}} e^{-s^3 x} 3s^2 ds \quad (7.1.17)$$

and simplifying gives

$$I = i3\sqrt{3}\tilde{\alpha}\int_0^\infty \frac{(-s^6\eta_{2D}(0) + s^3\eta'_{2D}(0) + \pi_0)}{s^{14} + s^7\tilde{\alpha} + \tilde{\alpha}^2} e^{-s^3 x} ds. \quad (7.1.18)$$

Now (7.1.12) becomes:

$$2\pi i\eta_{2D}(x) = i3\sqrt{3}\tilde{\alpha}\int_0^\infty \frac{(-s^6\eta_{2D}(0) + s^3\eta'_{2D}(0) + \pi_0)}{s^{14} + s^7\tilde{\alpha} + \tilde{\alpha}^2} e^{-s^3 x} ds + 2\pi i\Sigma(Res). \quad (7.1.19)$$

We can solve this for η_{2D}

$$\eta_{2D}(x) = \frac{3\sqrt{3}\tilde{\alpha}}{2\pi}\int_0^\infty \frac{(-s^6\eta_{2D}(0) + s^3\eta'_{2D}(0) + \pi_0)}{s^{14} + s^7\tilde{\alpha} + \tilde{\alpha}^2} e^{-s^3 x} ds + \Sigma(Res). \quad (7.1.20)$$

The integral and residues are purely real so we can easily implement this in Mathematica as follows. For the residues we make use of the fact that our singularities are simple poles, i.e. we calculate them

as $Res(c) = \frac{h(c)}{g'(c)}$ where c is the coordinate of the pole and $h(s) = (s\eta_{2D}(0) + \eta'_{2D}(0) - s^{-1}\pi_0)e^{sx}$ and $g(s) = s^2 + \tilde{\alpha}s^{-\frac{1}{3}}$. For the integral we divide the region of integration into small intervals and apply Simpson's rule on each interval. We also have to use a finite cut off, for this and the interval width we have done convergence tests. The next sections give results for the different model approaches. $\eta_{2D}(0)$ and $\eta'_{2D}(0)$ need to be determined by the boundary conditions, namely $\eta_{2D}(x) = 0$ at $x = x_0$ and $x = x_1$. We use this method in the following two sections, where we work with η_{2D}.s In section 7.4 we work with η_{3D} directly, although it would also be possible to use η_{3D} with more complex boundary conditions.

7.2 Two-dimensional calculations for a three-dimensional effect

As a first approximation to the three-dimensional model, we use the two-dimensional equations and treat the circle with slices that run parallel to the x-direction at intervals δz along the z-direction as depicted in figure 7.2. This allows us to use the same code as for the two-dimensional case described in section 6.1. However we focus on the simplified wall relation (7.1.1) and we only consider the linear model, which can alternatively be solved with the Laplace transform method described above. The nonlinear stage may be addressed with a fully numerical approach.

The computational procedure for the numerical method is as follows. An initial pressure distribution is guessed, then the blip shape η is calculated from (7.1.1) and (6.1.21) using a Thomas algorithm. With this newly guessed blip shape we calculate a correction for the revised pressure. The last two steps are then iterated until the convergence criterion, which is that the pressure difference from one iteration to next must be less than some small parameter ϵ, is fulfilled. In this section we work with $\epsilon = 10^{-6}$. We repeat the above steps for each "slice" through the blip as explained above. Results for this approach are shown in figure 7.4 below

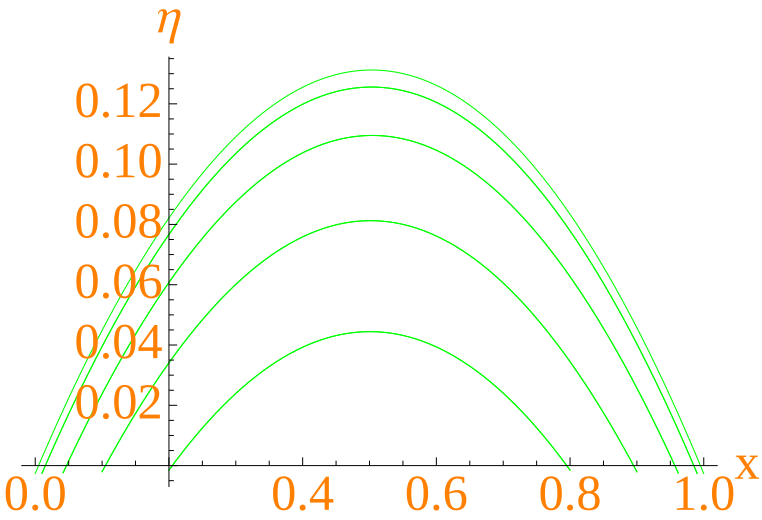

Figure 7.4: Converged results for η with $e_2 = 1$ and $p_0 = 1$ from repeated two-dimensional calculations

Alternatively, we can solve this set up using the Laplace transform described above. The computational procedure in this case is to simply solve (7.1.12) for each "slice" through the blip as shown in figure 7.5 below:

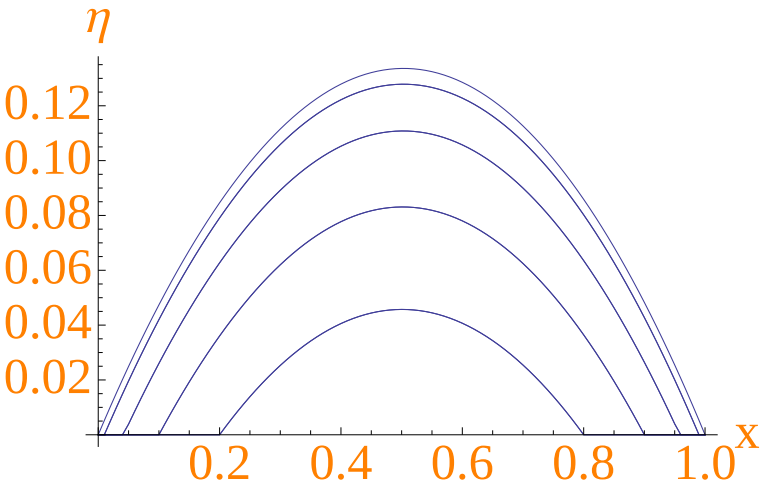

Figure 7.5: Results for η with $e_2 = 1$ and $p_0 = 1$ from repeated calculations utilising the Laplace transform method

For comparison of the two methods see figure 7.6 below

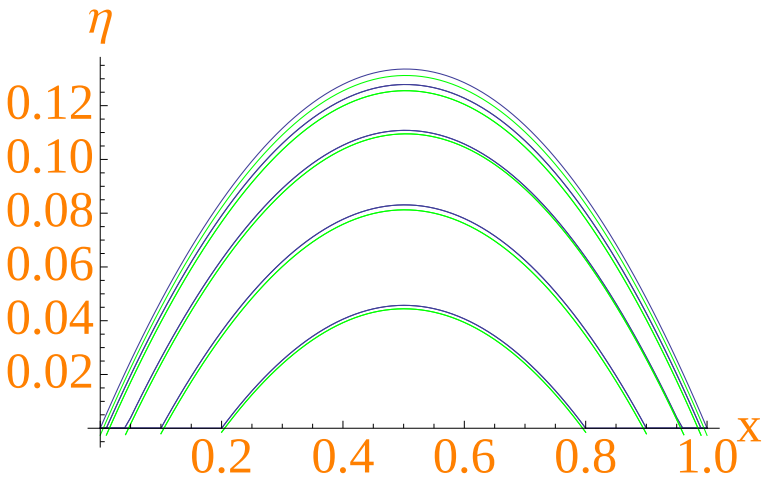

Figure 7.6: Comparison for η with $e_2 = 1$ and $p_0 = 1$ of Laplace method (blue) and numerical method (green)

We can see from figure 7.6 above that both methods give the same shape for the blip but the height is slightly different. The purely numerical method slightly underestimates the blip height compared to the Laplace method.

7.2.1 Refined grid

This is due to grid effects. In the above calculation we have used a very coarse grid with $\delta x = 0.1$. We have rerun the numerical calculations for a refined grid with $\delta x = 0.01$ and with $\delta x = 0.001$. The finer grid $\delta x = 0.001$ shows very good agreement between the two methods. See figure ... below where the Laplace method is shown in blue and the numerical method is shown in green. The results are almost identical

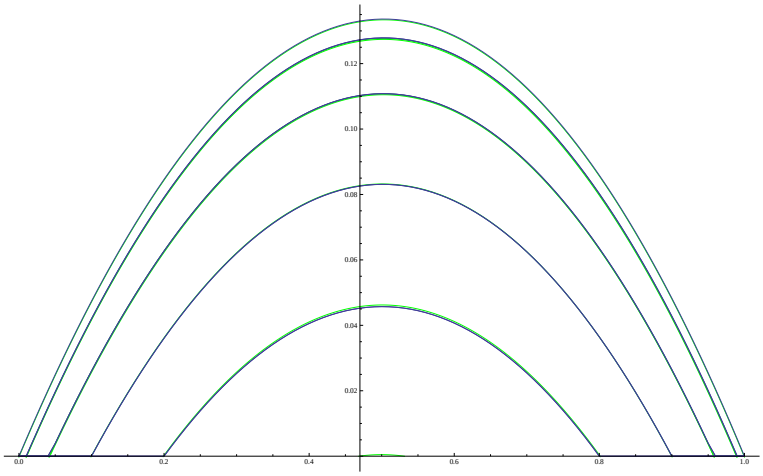

Figure 7.7: Refined grid comparison of numerical and Laplace methods

Also checking the boundary conditions at the edges shows that the error is $O(\delta y * 10^{-1})$ at most; this occurs where $x_0 = 0$ and $x_1 = 1$ with errors being -0.000261791and -0.000267583 respectively.

7.3 Quasi three-dimensional problem

As the next step, the idea for the quasi three-dimensional problem is to use the two-dimensional wall equation that emerges from the skewed-shear method [65] to calculate the wall shape, η, in the region we are considering and then to use this wall shape to calculate a three-dimensional pressure. So, in the quasi three-dimensional problem the three-dimensional effects in a sense only come into play in the pressure calculation.

In three dimensions we have the following equations [30] for linearized flow,

$$u_x + v_y + w_z = 0, \tag{7.3.1}$$

$$yu_x + v = -p_{3Dx} + u_{yy}, \tag{7.3.2}$$

$$yw_x = -p_{3Dz} + w_{yy}, \tag{7.3.3}$$

with boundary conditions $u = v = w = 0$ at $y = 0$ and $u \to \eta_{3D}(x, z)$ and $w \to 0$ as $y \to \infty$. Applying the method of skewed shears, i.e. applying the coordinate transform $Q = u_x + w_z$, and adding $\frac{d}{dx}$ (7.3.20) and $\frac{d}{dz}$ (7.3.3) gives

$$yQ_x + v_x = -p_{3Dxx} - p_{3Dzz} + Q_{yy} = -S + Q_{yy} \tag{7.3.4}$$

where $S = \nabla^2 p_{3D}$.

Also taking the derivative of equation (7.3.1) with respect to x gives

$$Q_x + (v_x)_y = 0. \tag{7.3.5}$$

Now we have the boundary conditions reading $Q = v_x = 0$ at $y = 0$ and $Q \to \eta_{3Dx}$ as $y \to \infty$. And it should be noted that $\eta_{2D} = \eta'_{3D}$.

The computational method is as follows. We solve for η_{2D} by the Laplace transform method then use (6.1.21) to solve for p_{2D}, which allows us to calculate $S = p'_{2D}$. And from S we can obtain the three dimensional pressure since $\nabla^2 p_{3D} = S$ as above.

To calculate η_{3D} we use the Laplace method as explained above in section 7.1, however we now have boundary conditions $\eta_{3D}(x) = \int \eta_{2D}(x)dx = 0$ at $x = x_0$ and $x = x_1$ since here η_{2D} is not the physical shape of the blip but η_{3D} is and it is the physical blip shape that needs to be zero at either end. This alters the shape slightly as is shown in the results in figures 7.7 - 7.9 below:

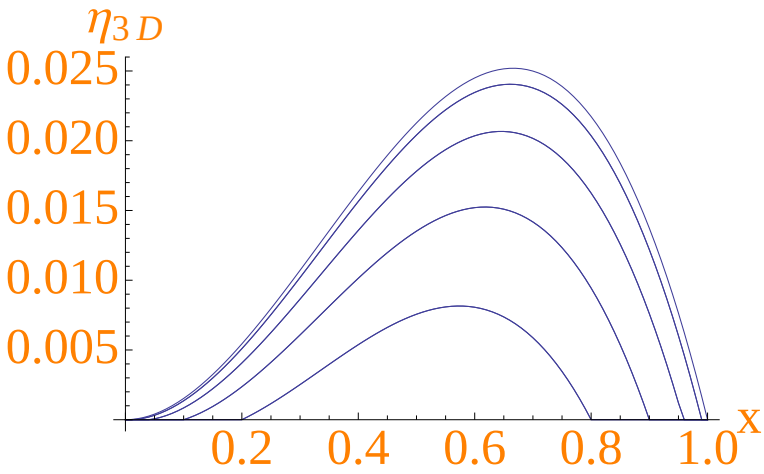

Figure 7.8: Results for η from quasi 3D calculations, using stepsize $\delta z = 0.1$

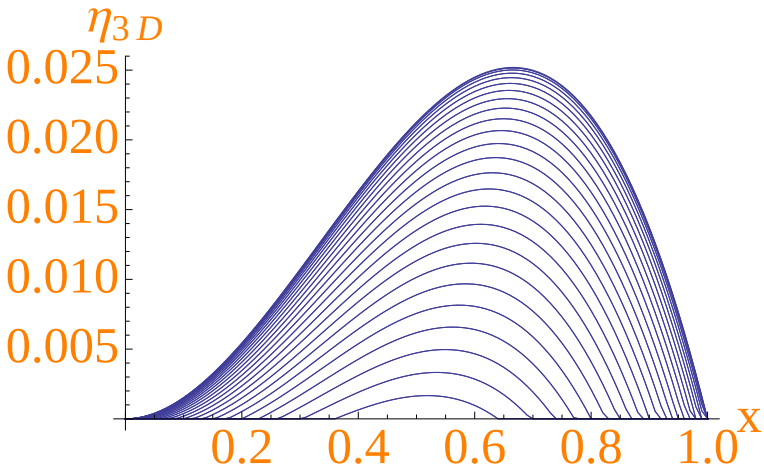

Figure 7.9: Results for η from quasi 3D calculations, using stepsize $\delta z = 0.05$

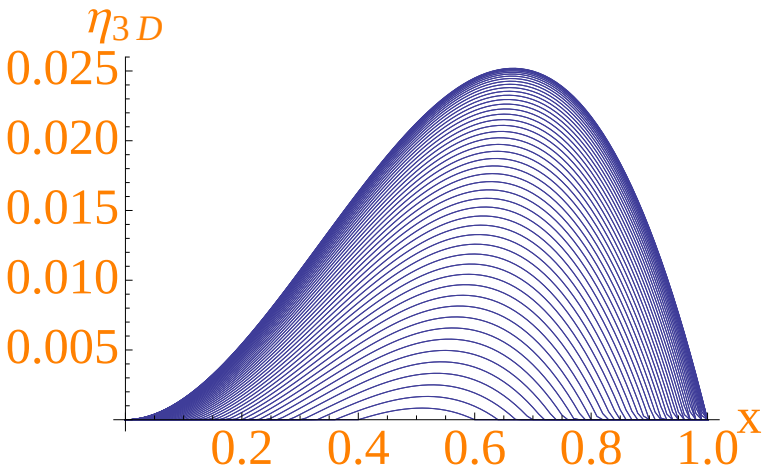

Figure 7.10: Results for η from quasi 3D calculations, using stepsize $\delta z = 0.01$

As expected the stepsize δz along the z-direction does not change the shape of the blip, since the z-dependence only comes into the pressure calculations at this stage. Below we show the results for the pressure for each case in figures 7.10 - 7.12:

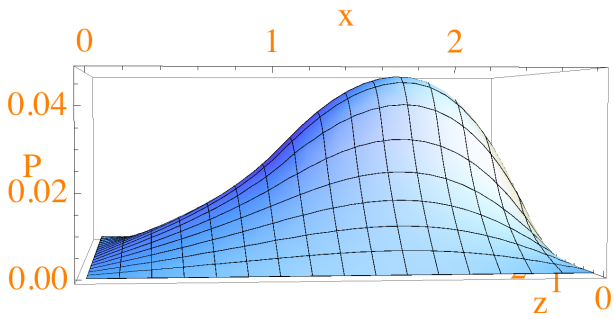

Figure 7.11: Results for η from quasi 3D calculations, using stepsize $\delta z = 0.1$

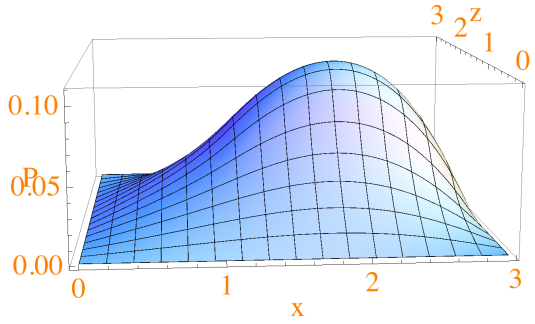

Figure 7.12: Results for η from quasi 3D calculations, using stepsize $\delta z = 0.05$

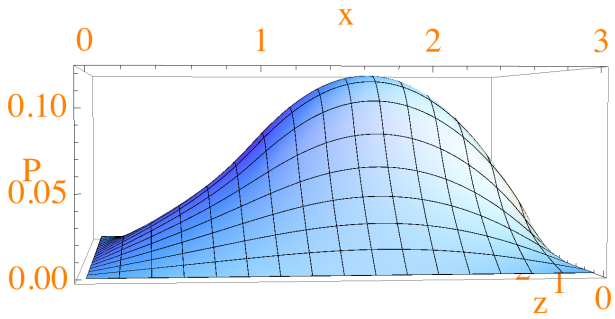

Figure 7.13: Results for η from quasi 3D calculations, using stepsize $\delta z = 0.01$

Here we can see that we need to chose the stepsize δz small enough to achieve converged results. We can see from figures 7.8 and 7.9 above that for a stepsize δz between 0.05 and 0.01 the pressure results are reasonable well converged.

We have done some calculations to determine the effect of p_0 on the blip, from chapter 6 we expect the blip height to be doubled as p_0 is doubled. Since the blip shape is not affected by the stepsize δz, we keep this fairly large, i.e. $\delta z = 0.1$, to keep calculation times low. For the results shown in figure 7.10 below we have doubled p_0 from 1 (the value used in all previous calculations in this chapter) to 2 and then again to 4 as shown in figure 7.11:

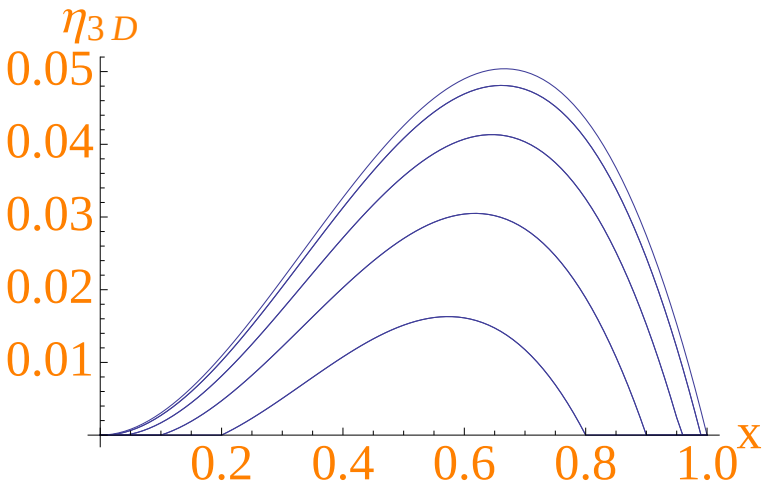

Figure 7.14: Results for η with $p_0 = 2$

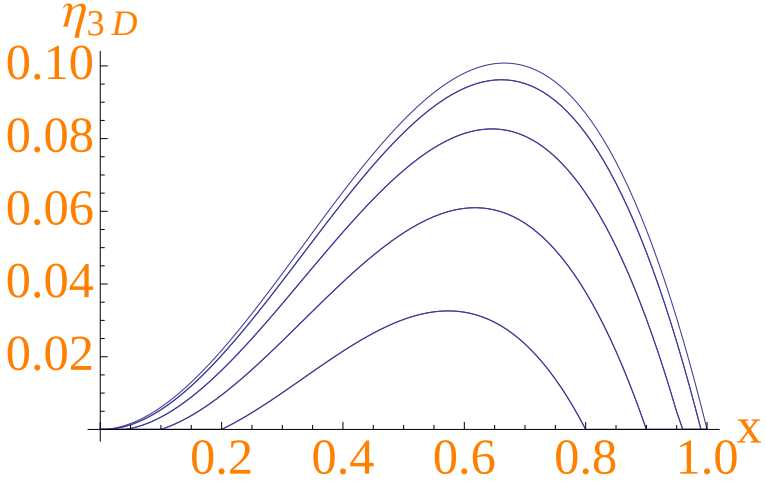

Figure 7.15: Results for η with $p_0 = 4$

We can see from figures 7.7, where $p_0 = 1$, 7.10, where $p_0 = 2$, and 7.11, where $p_0 = 4$, that doubling p_0 indeed doubles the blip height. Due to time constraints we have omitted here to calculate the pressure over the blips as the calculations require a refined grid, which makes the calculations time intensive.

7.4 Fully three-dimensional blip interactions

Finally, we derive the beginnings for fully three-dimensional blip interaction. The model here is intended to be more realistic. Here again we have to deal with two sets of equations: these are the equations describing the fluid response and the wall relation. Since we make use of the skewed shears method we can define the following quantities in terms of their two-dimensional counterparts: $Q \equiv u_{2D}$, $V_x \equiv v_{2D}$, $S \equiv p_{2Dx}$ and $\eta_{3Dx} = \eta_{2D}$. From the derivation of the skewed shears method it follows that $\nabla^2 P_{3D} = S$, see (7.15a). For the wall relation again we only keep the term containing e_2 but now we want to express the wall relation in terms of η_{3D} and S, where before we had $e_2\eta''_{2D} = p_{2D} - p_0$. Now we have the model

$$e_2\eta^{IV}_{3D} = S \tag{7.4.1}$$

or

$$e_2\eta''_{3D} = \int_{x_0}^{x}\int_{x_0}^{x} S dx dx - \pi_1. \tag{7.4.2}$$

This means we also have the conditions $\eta''_{3D}(x_0) = -\frac{\pi_1}{e_2} = -\hat{\pi}_1$, which is the known cavity pressure, and $\eta'''_{3D}(x_0) = 0$ in our model. Moreover closure requires the boundary conditions $\eta_{3D}(x_0) = \eta_{3D}(x_1) = 0$.

As above in (7.1.21-7.1.22) we have the following set of equations for the skewed shears method:

$$yQ_x + V_x = -S + Q_{yy}, \tag{7.4.3}$$

$$Q_x + (V_x)_y = 0 \tag{7.4.4}$$

with the boundary conditions:

$$Q = V_x = 0 \quad \text{at } y = 0, \tag{7.4.5}$$

$$Q \to \eta''_{3D} \qquad \text{as } y \to \infty. \tag{7.4.6}$$

We want to derive another relation between S and η_{3D}. Taking the derivative of (7.4.3) with respect to y and use (7.4.4) to eliminate $(V_x)_y$, we obtain

$$y(Q_y)_x = (Q_y)_{yy}. \tag{7.4.7}$$

Now, it is convenient to define $\tilde{T} = Q_y$ and apply a Fourier transform, which gives

$$y\tilde{T}_x = \tilde{T}_{yy} \tag{7.4.8}$$

and

$$yik\tilde{T}^* = \tilde{T}^*_{yy}, \tag{7.4.9}$$

respectively. Changing variable to $\zeta = (ik)^{\frac{1}{3}} y$ turns (7.4.9) into Airy's equation:

$$\zeta\tilde{T}^* - \tilde{T}^*_{\zeta\zeta} = 0, \tag{7.4.10}$$

the solution to which is known

$$\tilde{T}^*(\zeta) = B(k)Ai(\zeta) \tag{7.4.11}$$

where we have discarded the $Bi(z)$ term since our solution needs to be bounded at infinity. Applying the boundary condition at $y = 0$ gives

$$S^* = (ik)^{\frac{1}{3}} B(k)Ai'(0). \tag{7.4.12}$$

To eliminate $B(k)$ we apply the boundary condition as $y \to \infty$, i.e. we obtain

$$B(k) = \frac{(ik)^{\frac{1}{3}}}{\kappa}(\eta''_{3D})^* \tag{7.4.13}$$

and substituting this into (7.4.12) gives

$$S^* = \frac{(ik)^{\frac{2}{3}}}{\kappa}Ai'(0)(ik)^2\eta^*_{3D} \tag{7.4.14}$$

or

$$S^* = \frac{Ai'(0)}{\kappa}G^*(k)F^*(k) \tag{7.4.15}$$

where $\kappa = \int_0^\infty Ai(\zeta)d\zeta$ and we choose $G^*(k) = (ik)^{-\frac{1}{3}}$ and $F^*(k) = (ik)^3\eta^*_{3D}$. So applying the convolution theorem gives

$$S(x) = \frac{Ai'(0)}{\Gamma(\frac{1}{3})\kappa}\int_{x_0}^{x}(x-q)^{-\frac{2}{3}}\eta'''_{3D}(q)dq, \tag{7.4.16}$$

where $x > x_1$ the upper boundary needs to be x_1 since $\eta_{3D} \equiv 0$ outside of the region $[x_0, x_1]$. So inside the bilp we have

$$e_2\eta^{IV}_{3D}(x) = \frac{Ai'(0)}{\Gamma(\frac{1}{3})\kappa}\int_{x_0}^{x}(x-q)^{-\frac{2}{3}}\eta'''_{3D}(q)dq. \tag{7.4.17}$$

As we have described in detail in section 7.1 for the two-dimensional case this equation can also be solved via a Laplace transform but first we integrate in detail twice to accommodate (7.4.2) as it contains more information.

For convenience we divide through by e_2 and define $\alpha = \frac{Ai'(0)}{e_2\Gamma(\frac{1}{3})\kappa}$, so that we have

$$\eta^{IV}_{3D}(x) = \alpha\int_{x_0}^{x}(x-q)^{-\frac{2}{3}}\eta'''_{3D}(q)dq. \tag{7.4.18}$$

Now integrate once with respect to x from x_0 to x as follows:

$$\int_{x_0}^{x} \eta_{3D}^{IV}(\hat{x})d\hat{x} = \alpha \int_{x_0}^{x} \left\{ \int_{x_0}^{\hat{x}} (\hat{x}-q)^{-\frac{2}{3}} \eta_{3D}'''(q)dq \right\} d\hat{x}. \tag{7.4.19}$$

Next, changing the order of integration on the right hand side, we obtain

$$\eta_{3D}'''(x) - \eta_{3D}'''(x_0) = \alpha \int_{x_0}^{x} \left\{ \int_{q}^{x} (\hat{x}-q)^{-\frac{2}{3}} \eta_{3D}'''(q)d\hat{x} \right\} dq. \tag{7.4.20}$$

However $\eta_{3D}'''(x_0)$ is zero from (7.4.2). Also the factor $\eta_{3D}'''(q)$ on the right hand side does not depend on $\hat{x}$, so we can take it out of the integral, the remaining factor $(\hat{x}-q)^{-\frac{2}{3}}$ can be integrated analytically. So we have

$$\eta_{3D}'''(x) = 3\alpha \int_{x_0}^{x} (x-q)^{\frac{1}{3}} \eta_{3D}'''(q)dq. \tag{7.4.21}$$

Integrating again with respect to x from x_0 to x, we obtain

$$\int_{x_0}^{x} d\hat{x} \left\{ \eta_{3D}'''(\hat{x}) \right\} = 3\alpha \int_{x_0}^{x} \left\{ \int_{x_0}^{x} (\hat{x}-q)^{\frac{1}{3}} \eta_{3D}'''(q)dq \right\} d\hat{x}. \tag{7.4.22}$$

As above, integrating the left hand side and changing the order of integration on the right hand side gives

$$\eta_{3D}''(x) - \eta_{3D}''(x_0) = 3\alpha \int_{x_0}^{x} \left\{ \int_{q}^{x} (\hat{x}-q)^{\frac{1}{3}} \eta_{3D}'''(q)d\hat{x} \right\} dq. \tag{7.4.23}$$

Here again the factor $\eta_{3D}'''(q)$ does not depend on $\hat{x}$ and can be taken out of the integral and the remaining factor $(\hat{x}-q)^{\frac{1}{3}}$ can be integrated analytically. And we have

$$\eta_{3D}''(x) - \eta_{3D}''(x_0) = \frac{9\alpha}{4} \int_{x_0}^{x} \left\{ \eta_{3D}'''(q)(x-q)^{\frac{4}{3}} \right\} dq. \tag{7.4.24}$$

On the left hand side we now have $\eta_{3D}''(x)$ but on the right hand side we still have $\eta_{3D}'''(q)$. Therefore

integrate the right hand side by parts twice, to obtain

$$\int_{x_0}^{x}\left\{\eta_{3D}'''(q)(x-q)^{\frac{4}{3}}\right\}dq=-\eta_{3D}''(x_0)(x-x_0)^{\frac{4}{3}}-\frac{4}{3}\eta_{3D}'(x_0)(x-x_0)^{\frac{1}{3}}+\frac{4}{9}\int_{x_0}^{x}\left\{\eta_{3D}'(q)(x-q)^{-\frac{2}{3}}\right\}dq. \tag{7.4.25}$$

From substituting back into (7.4.24), and since $\eta_{3D}''(x_0)=-\hat{\pi}_1$, this gives

$$\eta_{3D}''(x)=\alpha\int_{x_0}^{x}\left\{\eta_{3D}'(q)(x-q)^{-\frac{2}{3}}\right\}dq-\hat{\pi}_1+E(x) \tag{7.4.26}$$

where

$$E(x)=\frac{9\alpha}{4}\hat{\pi}_1(x-x_0)^{\frac{4}{3}}-3\alpha\eta_{3D}'(x_0)(x-x_0)^{\frac{1}{3}}. \tag{7.4.27}$$

Next we need to find the Laplace transform of (7.4.26) with (7.4.27). We have gone through the details of the Laplace transform in section 7.1, so here we will just give the results since the working is very similar. Thus, with $\tilde{\alpha}=\Gamma(\frac{1}{3})\alpha$, we have

$$\eta_{3D}^{*}(s)=\frac{(s-\tilde{\alpha}s^{-\frac{1}{3}})\eta_{3D}(x_0)+\eta_{3D}'(x_0)-\hat{\pi}_1s^{-1}+E^{*}(s)}{s^2-\tilde{\alpha}s^{\frac{2}{3}}}. \tag{7.4.28}$$

from x_0 (an origin shift in x as anticipated earlier), i.e. to find $E^{*}(s)$ we note that the above equations apply from x_0 i.e. the Laplace integral becomes $\int_{x_0}^{\infty}e^{-s(x-x_0)}f(x)dx$. So

$$E^{*}(s)=\tilde{\alpha}\hat{\pi}_1s^{-\frac{7}{3}}-\tilde{\alpha}\eta_{3D}'(x_0)s^{-\frac{4}{3}}. \tag{7.4.29}$$

And we have

$$\eta_{3D}^{*}(s)=\frac{(s-\tilde{\alpha}s^{-\frac{1}{3}})\eta_{3D}(x_0)}{s^2-\tilde{\alpha}s^{\frac{2}{3}}}+\frac{(1-\tilde{\alpha}s^{-\frac{4}{3}})\eta_{3D}'(x_0)}{s^2-\tilde{\alpha}s^{\frac{2}{3}}}+\frac{(-s^{-1}+\tilde{\alpha}s^{-\frac{7}{3}})\hat{\pi}_1}{s^2-\tilde{\alpha}s^{\frac{2}{3}}}. \tag{7.4.30}$$

This simplifies to:

$$\eta^*_{3D}(s) = \frac{\eta_{3D}(x_0)}{s} + \frac{\eta'_{3D}(x_0)}{s^2} - \frac{\hat{\pi}_1}{s^3} \tag{7.4.31}$$

Inverting this gives:

$$\eta_{3D}(x) = \eta_{3D}(x_0) + \eta'_{3D}(x_0)(x - x_0) - \frac{1}{2}\hat{\pi}_1(x - x_0)^2 \tag{7.4.32}$$

We have the boundary conditions $\eta_{3D}(x_0) = \eta_{3D}(x_1) = 0$, from which we can determine $\eta'_{3D}(x_0) = \frac{1}{2}\hat{\pi}_1(x_1 - x_0)$. And our equation for $\eta_{3D}(x)$ becomes:

$$\eta_{3D}(x) = -\frac{1}{2}\hat{\pi}_1(x - x_0)^2 + \frac{1}{2}\hat{\pi}_1(x_1 - x_0)(x - x_0) \tag{7.4.33}$$

The solution is neat and simple according to the above and the resulting shape is realistic. The assumptions leading to (7.4.26) need checking but it is interesting to observe that the finding here of a predicted parabolic shape at each z location is very similar to those derived in the previous section.

We note there is an alternative interpretation based on re-examining (7.4.15). We have defined $F^* = (ik)^3\eta^*_{3D}$, which leads to η'''_{3D}, which is questionable as it may be discontinuous at the boundary. We could have instead defined $F^* = (ik)\eta^*_{3D}$ and divided through by (ik) which would lead to $\frac{S^*}{(ik)^2}$ on the left hand side. This alternative set up would lead to $\int\int S dx dx = \alpha \int (x-q)^{-\frac{2}{3}}\eta'_{3D}(q)dq$, which can be combined with (7.4.2). This would lead to the 2D results from earlier, so this supports the previous results that the full 3D and the 2D give the same blip shapes. However, this remains to be explored further.

Chapter 8

Conclusions and further work

8.1 Direct points

The overall concern of this thesis is with fluid flow past a body with a flexible surface which interacts with the flow. We have outlined the governing equations, non-dimensionalisation and scalings in chapter 2. Over most of the thesis we consider steady-flow phenomena apart from chapter 4 where we also investigate time-dependent effects.

In chapter 3 we have shown that instabilities arise even for simple piecewise-linear velocity profiles due to a flexible wall, particularly towards shorter wavenumbers.

In chapter 4 we take into account that real-world applications often require the inclusion of viscous effects; so here we have used the triple-deck structure to examine the occurrence of instability due to a flexible wall. We have studied time-dependent, time-independent and full dispersion relations arising from the coupling of the flexible-wall relation with the triple-deck structure of the flow. Here we have found that smaller values of the flexibility parameters produce a shift of the spatial growth rate relative to the solid-wall solution of pure Tollmien-Schlichting instabilities. In the time-independent case this shift occurs mostly for smaller values of the frequency. However, in the full dispersion relation we can see this shift occurring over a wide range of frequencies, with reducing

e_2 producing the largest shift towards increasing the instabilities.

The blip scales investigated with the triple-deck method are small compared to the boundary-layer scale. For completeness we have also studied blips on a larger scale, where the flexible wall spans from the front stagnation point to the separation point of a bluff body, see chapter 5. USe was then made of a prescribed pressure to calculate the blip shape, which for most cases we have tested produces a maximum height near the pressure minimum. This may indicate the possibility of moving the position of the breakaway separation point.

Another interesting phenomenon that we have investigated, in chapter 6, is that of resonance for short blips. Here we have introduced a parameter measuring the ratio of flow strength to flexibility strength. We have studied both a linear and a nonlinear model here. Both models show that as we increase this ratio parameter we eventually see resonance behaviour although in the comparison we show that the linear model seems to underestimate the blip height and pressure change for larger values of the ratio parameter. As in the triple-deck case smaller flexibility parameters produce more instability at a smaller ratio parameter. This leads to the extension from one blip to several blips. The work shows that, on inclusion of several blips, the effects on pressure change and wall shear become cumulative. This means that several blips could produce flow separation for parameter values for which a single blip does not.

Finally, in chapter 7, we have extended our model to three dimensions. Here we had to make some further simplifications to the wall-relation, namely to only include the term containing e_2 which is associated with the tension of the material. First approximations include applying the two-dimensional method with suitable boundary conditions for a three-dimensional model.

In the introduction we have stated that our aim is/was to find a method which utilizes flexible surfaces to create a tune-able trip in order to aid transition to turbulence and hence reduce overall drag. In effect this is what we have shown these flexible blips do, as they switch on\off depending on the speed. They also accommodate different directions more readily than conventional trips.

Further work we suggest could include more study of on the three-dimensional model. In this thesis we have significantly simplified the wall-relation and only considered small blips. It would be interesting to see how the results change with inclusion of more terms in the wall relation and also what behaviour occurs for large blips as discussed in chapter 5. The study of resonance presented in chapter 6 relies heavily on numerical calculations; further work might involve a more analytical treatment.

The idea behind using flexible blips as tune-able trips and trips in general is to make the boundary layer undergo transition from laminar to turbulent motion in order for it to stay attached for longer and hence reduce overall drag. Initially we considered the analysis of the laminar-turbulent crossover but decided to drop this approach in favour of the other work presented in this thesis. However, including flexible blips in the analysis of the laminar-turbulent crossover could yield very interesting results.

8.2 Wider view

Aimed at the wider audience, this section summarizes small-blip effects in the first sub-section below (noting that the effects of large blips are mostly reported already in chapter 5) and then describes in a second sub-section special final or remaining matters that arose from continual discussions with interested parties. There may be a little overlap with discussions presented earlier in the present chapter for example but the goal here is quite distinct.

8.2.1 Summary on small-blip effects

A summary report is given here for the intended benefit of readers who are possibly more concerned with somewhat broader implications or with applications than with the theoretical, technical or applied-mathematical details.

This mathematical modelling work holds for one or more surface-mounted small blips buried well inside a boundary layer of air motion. By small blip we mean a hump of streamwise length scale

not far different from the local boundary layer thickness (say 1 - 2 mms in practice), maybe slightly longer or shorter. By buried we mean of height scale which is much less than the boundary layer thickness. The blip is thus shallow. It is also flexible: its shape is determined by the local pressure variation which in turn is determined by the shape, so that there is interaction.

The motion is taken to be laminar at first everywhere in the local setting as well as two-dimensional and steady although unsteady factors may be expected to have the same scales as here prior to transition. The two-dimensionality say in Cartesian coordinates x, y corresponds to having a strip or strips of blips that are long in the third direction z. In the two-dimensional view there is either a single flexible blip or a succession of flexible blips at a distance apart which is comparable with the blip length.

The boundary layer coming on to the blip is supposed as laminar and steady or at least it has no significant variation over short length scales in the streamwise direction. The oncoming pressure is not extreme. The Reynolds number based on a typical overall length scale of say 10 cms is large but the Mach number small. The main flow direction of the boundary layer is perpendicular to the z direction, resulting in a two-dimensional motion riding over the blip or blips.

The governing dynamics in this scenario is the interactive boundary layer response applying in a thin sublayer containing the blip but with the local pressure variation being unknown and related to blip shape (η or eta) via flexural rigidity, tension and spring stiffness. There are many parameters present but the major point is the following. The interplay of the air flow, the local pressure and the flexible wall shape is nonlinear in the sense that local velocity profiles are provoked which are substantially different from the oncoming undisturbed profiles. These can in fact produce: (a) inflection in some of the velocity profiles (usually where the flow enters the lee of the blip), (b) separation of the flow, (c) resonance in the pressure-shape interaction, as the blip height gets increased by means of alterations in the parameter values. Any of (a) - (c) can lead on to quite violent /rapid instability and hence transition to turbulence in the air flow. The range of parameters producing (a) is large, greater than that for (b) which in turn is greater than that for (c).

Results are in the figures earlier in the thesis, mainly in chapters 5-7, supporting the order (a) - (c). Details and some background concerning the results are provided in the text. The implication is that transition can occur over a wide parameter range for small blips. Transition is enhanced by increasing incident flow pressure or by increasing flow shear for instance. It is also enhanced by increasing the number of successive blips. Whether there is an overlap with the behaviour of realistic materials remains to be seen in full.

8.2.2 Final /remaining points

A perhaps wider and alternative view is also provided by our referring next to meetings held during 2008-2012 with Drs Rob Lewis, Graham Johnson and Philip Bond and on occasion Dr Scott Drawer as part of the doctoral project. There were many such meetings. Here certain of the principal points that arose from the meetings are presented in more or less their original form as Points1, 2, etc below along with corresponding comments or Responses made now rather with the benefit of hindsight and of the research in this thesis. Other principal points were incorporated into the thesis research as it proceeded.

Point 1. Sum up the possibilities for the future.
Response 1. They include: more complete three-dimensional modelling; converting the reduced-equation systems of the present thesis to code /openfoam for example; more insight into effects of materials on separation; flow control by means of blips; parameter guidance on selection of materials.

Point 2. Can some of the complex matters involved in the current fluid-body interactions be explained clearly and simply from both the mathematical and the physical perspectives?
Response 2. We hope that has been at least partly achieved in the thesis.

Point 3. For the blips of chapter N2, is there a pressure recovery downstream?
Response 3. The answer is yes, from analysing the linearised case.

Point 4. The values of the coefficients $e_1 - e_5$ vary from material to material.

Response 4. We obtained our estimates of them from BAE Systems.

Point 5. Thickness^3 appears in the definition of rigidity.

Response 5. This indicates sensitivity of the coefficients to details of the material used.

Point 6. For large blips: we should vary $e_1 - e_5$ in this case; note one could link them via their original definitions; so better investigate their original definitions.

Response 6. This has not entirely been done as yet, but we remark that a factor 2 change in one e coefficient may imply a factor 8 change in another e.

Point 7. For small blips one may be able to tune the ballooning effect (i.e. resonance) to the actual flow speed.

Response 7. That would be equivalent to our b effect and is an interesting possibility.

Point 8. Name the practical conclusions.

Response 8. These would include the following: adjustable trips are emerging, in a sense; they go on /off depending on speed; and they can hide; different directions of oncoming flow can be accommodated; multiple blips; uses of trips in other domains; decreases in speed can be accommodated; one can vary major parameters; they are found to yield large differences; this tends to suggest trying new materials.

Point 9. Explain the relationship between the condensed case (where $A = 0$ in effect) and the triple-deck case (where scaled displacement A is linked to pressure P).

Response 9. This was written out in Smith, Brighton, Jackson and Hunt (1981) [58]. The relationship is really via the skin-friction factor λ and the length scale. In the condensed case in particular we have in scaled form, after a Prandtl transposition, $u \sim \lambda * (y + f)$ where f is the blip (or roughness) shape. Normalising out lambda then involves setting $u = \lambda^{\frac{2}{3}} * U$, $y = \lambda^{\frac{1}{3}} * Y$; here we assume the blip length scale x is fixed, as is the blip shape f. That leaves us with the nonlinear sublayer equations still but $U \sim Y + \lambda(\frac{1}{3}) * f$. So the effect of the blip (f) increases as λ increases.

The effect is maximal quite near the position of pressure minimum, which is probably where we want it to be focussed in some applications.

Point 10. Give a straightforward derivation of the triple-deck scales.

Response 10. Assuming nondimensionalisation such that we have an oncoming boundary layer of traditional thickness $O(Re^{-\frac{1}{2}})$, the following order-of-magnitude argument establishes the triple deck scales. Suppose something at the wall [such as a slender hump or corner] has streamwise length scale L say, with $L << 1$. Then a viscous layer of thickness $y \sim Re^{-\frac{1}{2}} * L^{\frac{1}{3}}$ is induced, in order to balance the inertial operator $\frac{u}{L}$ with the viscous operator $\frac{Re^{-1}}{y^2}$ and bearing in mind that u is of order $Re^{\frac{1}{2}} * y$ near the wall. So the viscous layer has $u \sim L^{\frac{1}{3}}$ and hence its $p \sim L^{\frac{2}{3}}$. ((A))
Meanwhile the vertical displacement of the whole boundary layer $\sim Re^{-\frac{1}{2}} * L^{\frac{1}{3}}$ and this affects the potential flow outside, producing p proportional to displacement slope, i.e. $p \sim Re^{-\frac{1}{2}} * L^{-\frac{2}{3}}$. ((B))
Balancing off ((A)), ((B)) gives the triple deck length scale, $L \sim Re^{-\frac{3}{8}}$. ((C))
All other scales such as those of velocity and pressure p then follow easily in the three implied decks.

Point 11. Estimate in #1 below when /how blips would actually come into play, say on a bluff body (note in passing, the increasing skin friction and the thinning boundary layer near the pressure minimum are important), and also estimate in #2 below the probability of transition (note in passing, the occurrence of flow reversal would indicate generally that transition has just taken place).

Response 11:- #1. The blip planform should be circular. The blip length (diameter) should be close to the expected incident boundary-layer thickness where transition to turbulence is required, say 2mms or perhaps 1-4 mms depending on Reynolds number. The arrays of blips can also be situated almost anywhere leading up to the transition region; precision is not necessary. The scalings involved mean that the effects of the blips really kick in quite near the pressure minimum, as the skin friction passes through its maximum, prior to large-scale separation. The effects in (from) an array are additive; so having many blips is beneficial, other things being equal. #2. For a given length of blip (or an array of them), the probability of transition due to the blip increases with distance

from the front stagnation point, beginning close to zero but reaching 90% or even 90%-100% at separation. Specifically between stagnation and the onset of separation the probability depends on scaled-skin-friction-to-the-one-third-power. So the estimate for the probability of transition at station x is

$$\text{Probability} = \lambda^{\frac{1}{3}} * 90\%$$

where λ is the ratio of the skin friction at x to the maximum skin friction just prior to separation.

Point 12. List the achievements, tools and understanding from the research.
Response 12. Achievements concern advances on interaction of blip oscillations and instability waves; prediction of flow separation on 2D blips or long blip-strips in 3D; effects of blip size and spacing on such separations; linear and nonlinear resonance; flow-field calculations showing inflection and separation; 3D modelling. Tools used are theory and calculation methods for 2D and 3D cases, including flow-wall interactions. Understanding is centred on more quantitative appreciation of how several important routes to transition soon arise when blips are present.

Point 13. Related points include: predict what arrangement of small blips is most likely to yield transition, given a rectangle of prescribed length.
Response 13. Tentative predictions can be made in terms of spacing and size of blips based on present findings.

Point 14. It could be helpful to provide a curve showing probability of transition versus distance say.
Response 14. This depends on the particular situation. One approach in certain free-stream environments is to tackle inflectional instability which is expected especially on the rearward side of the typical blip (see Smith and Bodonyi 1983).

Point 15. A 3D Navier-Stokes direct-computational code would in principle give us the surrounding pressure and parameter values. We could be supplied with the codes results for p-wall, τ-wall in

particular. Can we embed our theory inside that?

Response 15. That is a major question and challenge for the future.

Point 16. Can a separation point be achieved with minimum pressure loss, i.e. with minimum energy loss in some sense?

Response 16. Here separation may be taken as signalling transition. We have again a major question.

Point 17. Does a flexible blip perform better than a step-down trip in the sense of provoking transition?

Response 17. Our view tends towards yes but more research is necessary on the subject.

Point 18. Theory might lead on to turbulent vortex generators or turbulence enhancers.

Response 18. Intuition from the current investigations suggests the above devices should have length scales not very different from the present short-range blips, if an array of such devices is being considered.

Bibliography

[1] A. R. Paterson, *A first Course in Fluid Dynamics*, Cambridge University Press (1983)

[2] G. K. Batchelor, *An Introduction to Fluid Dynamics*, Cambridge University Press (1967, 1973, 2000)

[3] A. Neish and F. T. Smith, *On turbulent separation in the flow past a bluff body*, J. Fluid Mech. (1992), vol. 241, pp. 443-467

[4] H. K. Cheng and F. T. Smith, *The influence of airfoil thickness and Reynolds number on separation*, Journal of Applied Mathematics and Physics (1982), vol. 33

[5] M. Gad-el-Hak, *Flow Control: Passive, Active, and Reactive Flow Management*, Cambridge University Press (2000)

[6] N. C. Ovenden and F. T. Smith, *Vortices and flow reversal due to suction slots*, Phil. Trans. R. Soc., A (2005) 363, pp. 1199-1208

[7] F. T. Smith, L. Li and G. X. Wu, *Air cushioning with a lubrication/inviscid balance*, J. Fluid Mech. (2003), vol. 482, pp. 291-318

[8] A. S. Ellis, F. T. Smith and A. White, *Surface roughness effects on droplet impact*, Q J Mechanics Appl Math (2011)

[9] P. Bond, *Pressure and Drag on Surfaces*

[10] F. T. Smith and S. N. Timoshin, *Planar flows past thin multi-blade configurations*, J. Fluid Mech. (1996), vol. 324, pp. 355-377

[11] R. G. A. Bowles and F. T. Smith, *Lifting multi-blade flows with interactions*, J. Fluid Mech. (2000), vol. 415, pp. 203-226

[12] R. G. A. Bowles and F. T. Smith, *Interactive flow past multiple blades and wakes*, Q. Jl Mech. appl. Math. (2000) 53(2), pp. 207-251

[13] F. T. Smith, *On the High Reynolds Number Theory of Laminar Flows*, IMA Journal of Applied Mathematics (1982) 28, pp. 207-281

[14] D. T. Papageorgiou and F. T. Smith, *Linear instability of the wake behind a flat plate placed parallel to a uniform stream*, J. Fluid Mech. (1989), Vol. 208, pp. 67-89

[15] F. T. Smith, R. G. A. Bowles, L. Li, *Nonlinear effects in absolute and convective instabilities of a near-wake*, Eur. J. Mech. B - Fluids (2000) 19, pp. 173-211

[16] N. D. Sandham, *Transitional separation bubbles and unsteady aspects of aerofoil stall*, The Aeronautical Journal (2008), vol. 12 No. 1133, pp. 395-404

[17] L. E. Jones, R. D. Sandberg and N. D. Sandham, *Direct numerical simulations of forced and unforced separation bubbles on an airfoil at incidence*, J. Fluid Mech. (2008), vol. 602, pp. 175-207

[18] M. O. Kramer, *Boundary layer stabilization by distributed damping*, J. Amer. Soc. Naval Engrs. (1960), vol. 72, pp. 25-33

[19] T. B. Benjamin, *Effects of a flexible boundary on hydrodynamic stability*, J. Fluid Mech. (1960), vol. 9, pt. 4

[20] P. W. Carpenter and A. D. Garrad, *The hydrodynamic stability of flow over Kramer-type compliant surfaces. Part I Tollmien-Schlichting instabilities*, J. Fluid Mech. (1985), vol. 165, pp. 465-510

[21] P. W. Carpenter and A. D. Garrad, *The hydrodynamic stability of flow over Kramer-type compliant surfaces. Part II Flow-induced surface instabilities*, J. Fluid Mech. (1986), vol. 170, pp. 199-233

[22] C. Davis and P. W. Carpenter, *Instabilities in a plane channel flow between compliant walls*, J. Fluid Mech. (1997), vol. 352, pp. 205-243

[23] J. S. B. Gajjar and P. Sibanda, *The hydrodynamic stability of channel flow with compliant boundaries*, Theoret. Comput. Fluid Dynamics (1996), vol. 8, pp. 105-129

[24] P. W. Carpenter and P. K. Sen, *Effects of Boundary-Layer Growth on the Linear Regime of Transition over Compliant Walls*, Laminar-Turbulent Transition (1990), IUTAM Symp. Toulouse France, p. 123

[25] T. Theodorsen, *General Theory of Aerodynamic Instability and the Mechanism of Flutter*, National Advisory Committee for Aeronautics, Report No. 496

[26] T. Theodorsen and I. E. Garrick, *Flutter Calculations in Three Degrees of Freedom*, National Advisory Committee for Aeronautics, Report No. 741

[27] A. D. Fitt and M. P. Pope, *The unsteady motion of two-dimensional flags with bending stiffness*, J. Eng. Math. (2001), vol. 40, pp. 227-248

[28] O. E. Jensen, M. K. Horsburgh, D. Halpern and D.P. Gaver III, *The steady propagation od a bubble in a flexible-walled channel: Asymptotic and computational models*, Physics of Fluids (2002), vol. 14, pp. 443-457

[29] M. Argentina and L. Mahadevan, *Fluid-flow-induced flutter of a flag*, PNAS (2005), vol. 102, pp. 1829-1834

[30] A. Alben and M. J. Shelley, *Flapping States of a flag in an Inviscid Fluid: Bistability and the Transition to Chaos*, PRL (2008), vol. 100

[31] H. Schlichting and K. Gersten, *Boundary-Layer Theory*, Springer (2004)

[32] E. Reshotko , *Transient growth: A factor in bypass transition*, Phys. Fluids (2001) 13, 1067

[33] M. V. Morkovin, *On the many faces of transition*, In: Viscous Drag Reduction (1969), ed. CS Wells, pp. 131. New York: Plenum

[34] M. E. Goldstein and L. S. Hultgren, *Boundary-layer receptivity to long-wave free-stream disturbances*, Ann. Rev. Fluid Mech. (1989) 21, pp. 137-166

[35] W. S. Saric, H. L. Reed and E. J. Kerschen, *Boundary-Layer Receptivity to Freestream Disturbances*, Annu. Rev. Fluid Mech. (2002) 34, pp. 291-319

[36] P. W. Duck, A. I. Ruban and C. N. Zhikharev, *The generation of Tollmien-Schlichting waves by freestream turbulence*, J. Fluid Mech. (1996), vol. 312, pp. 341-371

[37] P. Hall and F. T. Smith, *A suggested mechanism for non-linear wall roughness effects on high Reynolds-number flow stability*, Studies in Applied Mathematics (1982), vol. 66, pp. 241-265

[38] J. E. F. Green, N. C. Ovenden and F. T. Smith, *Flow in a multi-branching vessel with compliant walls*, J. Eng. Math. (2009), vol. 64, pp. 353-365

[39] B. Scheichl and F. S. G. Paleotti, *Elasto-hydrodynamic lubrication of rough contacts: on a rigorous generalisation of the homogenisation approach*, ECCOMAS (2012)

[40] F. T. Smith, *Separating Flow: Small-scale, Large-scale, and Nonlinear Unsteady Effects*, Boundary-Layer Separation (1987), Springer, pp. 331-345

[41] F. T. Smith, *On physical mechanisms in two- and three-dimensional separations*, Phil. Trans. R. Soc. Lond. A (2000) 358, pp. 3091-3111

[42] F. T. Smith, *The separating flow through a severely constricted symmetric tube*, J. Fluid Mech. (1979), vol. 90, part 4, pp. 725-754

[43] V. V. Kozlov, *Interrelation of the Flow Separation and Stability*, Boundary-Layer Separation (1987), Springer, pp. 349-366

[44] A. V. Dovgal, V. V. Kozlov and O. A. Simonov, *Experiments on Hydrodynamic Instability of Boundary Layers with Separation*, Boundary-Layer Separation (1987), Springer, pp. 109-130

[45] R. L. Simpson, *A Review of Two-dimensional Turbulent Separated Flow Calculation Methods*, Boundary-Layer Separation (1987), Springer, pp. 179-196

[46] F. T. Smith, *On the non-parallel flow instability of the Blasius boundary layer*, Proc. R. Soc. Lond. A. 366 (1979), pp. 91-109

[47] F. T. Smith, *Two-dimensional disturbance travel, growth and spreading in boundary layers*, J. Fluid Mech. (1986), vol. 169, pp. 353-377

[48] D. A. R. Davis and F. T. Smith, *Influence of cross-flow on nonlinear Tollmien-Schlichting/vortex interaction*, Proc. R. Soc. Lond. A (1994) 446, pp. 319-340

[49] F. T. Smith, *Steady and unsteady boundary layer separation*, Ann. Rev. Fluid Mech (1986) , 18, pp. 197-220

[50] A. P. Rothmayer and F. T. Smith, *Incompressible Triple-Deck Theory*, In: Johnson, RW, (ed.), CRC Handbook of Fluid Dynamics (1998), New York, chps. 23-25

[51] V. V. Sychev et al, *Asymptotic theory of separated flows*,Cambridge University Press (1998), Cambridge, New York

[52] P.-Y. Lagree, *Mixed convection at small Richardson Number on Triple deck scales ("Convection thermique mixte faible nombre de Richardson dans le cadre de la triple couche")*, C. R. Acad. Sci. Paris (1994), t. 318, Srie II, pp. 1167- 1173

[53] P.-Y. Lagree, *Interactive Boundary Layer in a Hele Shaw cell*, Z. Angew. Math. Mech. (2007) 87, No. 7, pp. 486-498

[54] F. T. Smith, R. I. Sykes and P. W. M. Brighton, *A two-dimensional boundary layer encountering a three-dimensional hump*, J. Fluid Mech. (1977), vol. 83, part 1, pp. 163-176

[55] P. G. Drazin and W. H. Reid, *Hydrodynamic Stability*, Cambridge Univesity Press (1981)

[56] P. J. Schmid and D. S. Hennigson, *Stability and Transition in Shear Flows*, Springer (2001)

[57] I. J. Sobey, *Introduction to Interactive Boundary Layer Theory*, Oxford University Press (2000)

[58] F. T. Smith, P. W. M. Brighton, P. S. Jackson and J. C. R. Hunt, *On boundary-layer flow past two-dimensional obstacles*, J. Fluid Mech. (1981), vol. 113, pp. 123-152

[59] P. G. Larose and J. B. Grotberg, *Flutter and long-wave instabilities in compliant channels conveying developing flows*, J. Fluid Mech. (1997), vol. 331, pp. 37-58

[60] D. P. Gaver, D. Halpern, O. E. Jensen and J. B. Grotberg, *The steady motion of a semi-infinite bubble through a flexible-walled channel*, J. Fluid Mech. (1996), vol. 319, pp. 25-65

[61] L. Rosenhead, *Laminar Boundary Layers*, Dover Publications (1988)

[62] F. T. Smith, *Pipeflows distorted by non symmetric indentation or branching*, Mathematika (1976) 23, pp. 62-83

[63] R. I. Sykes, *On three-dimensional boundary layer flow over surface irregularities*, Proc Roy Soc A (1980), vo.l 373, pp. 311-329

[64] F. T. Smith and A. G. Walton, *Flow past a two- or three-dimensional steep-edged roughness*, Proc. R. Soc. A (1998), vol. 454, pp. 31-69

[65] F. T. Smith, *Properties and a finite-difference approach, for interactive three-dimensional boundary layers*, UTRC report (1983) UT 83-46, East Hartford, Connecticut, USA. See also Ann. Rev. Fluid Mech. (1986)